

# **Adsorption onto Heterogeneous Porous Materials: Equilibria and Kinetics**

## **PROEFSCHRIFT**

ter verkrijging van de graad van doctor aan de Technische Universiteit  
Eindhoven, op gezag van de Rector Magnificus, prof.dr. M. Rem, voor een  
commissie aangewezen door het College voor Promoties in het openbaar te  
verdedigen op dinsdag 5 juni 2001 om 16.00 uur

door

**Frans Bernard Aarden**

geboren te Standdaarbuiten

Dit proefschrift is goedgekeurd door de promotoren:

prof.dr.ir. P.J.A.M. Kerkhof

en

prof.dr.ir. K. Kopinga

Copromotor:

dr.ir. A.J.J. van der Zanden

CIP-DATA LIBRARY TECHNISCHE UNIVERSITEIT EINDHOVEN

Aarden, Frans B.

Adsorption onto heterogeneous porous materials : equilibria and kinetics / by Frans B. Aarden. - Eindhoven : Technische Universiteit Eindhoven, 2001.

Proefschrift. - ISBN 90-386-2822-6

NUGI 813

Trefwoorden: scheidingstechnologie ; adsorptie / poreuze materialen ; diffusie / actieve koolstof / MRI / fysisch-chemische simulatie ; dichtheidsfunctionalen

Subject headings: separation technology ; adsorption / porous materials ; diffusion / activated carbon / magnetic resonance imaging / physicochemical simulation ; density functional theory

**Voor mijn ouders**

# Summary

Adsorption technology is important for the separation and purification of products, which often is the value adding step in process industry. Together with the development of new materials, like zeolites and micro-porous membranes, this stresses the need to gain a better understanding in adsorption processes.

The basic objective of the study in this thesis is to contribute to the understanding and modelling of the equilibria and kinetics of adsorption processes. Special attention is given to the phase separation inside a porous material.

In chapter 1, a short introduction to adsorption processes is presented.

Chapter 2 discusses the properties of the materials that were used in this study. Those materials were three types of activated carbon and several adsorbates. The adsorbates were all organic compounds, namely, nitrobenzene, p-nitroaniline, quinoxaline, benzene and pyridine. Nitrogen adsorption experiments and mercury porosimetry experiments were carried out to characterise the activated carbons. The aqueous phase sorption isotherms of the organic adsorbates were measured at several temperatures. The sorption isotherms were modelled with a Radke-Prausnitz isotherm. This model fits the experimental data well over a large concentration range, compared to popular models such as the Langmuir, Freundlich and Jossens isotherms.

In chapter 3, the use of the Kierlik-Rosinberg density functional theory, for the calculation of multi-component sorption equilibria of simple Lennard-Jones molecules in a slit pore, is discussed. The model shows the existence of several pore filling mechanisms, dependent on molecular interactions, pore width and temperature. These mechanisms are: continuous pore filling, film layer formation and capillary phase separation.

The density functional theory also is used to calculate the pore size distribution of the activated carbons, used in this study, from the nitrogen sorption isotherms. It predicts pore sizes that are about twice as large than predicted by the Horvath-Kawazoe method, which is an often used method to characterise the pore size distribution of an activated carbon. The prediction of the pore size may have important consequences in understanding kinetics of adsorption since the pores are only a few molecular diameter in width and the molecular motion in the first molecular layer near the pore wall differs greatly from the kinetics of molecules, further away from the pore wall.

In Chapter 4, a new model is put forward for the calculation of the intra-particle kinetics for adsorption from the liquid phase. Contradictory to the usual models, which are based on surface diffusion, this one is based on the capillary flow of capillary phase separated adsorbate. The model is applied to experimental data from literature on the adsorption of nitrobenzene and benzonitrile from the liquid phase onto activated carbon. A good prediction is obtained for the

dependence of the effective diffusion coefficient on the amount adsorbed and temperature.

Chapter 5 presents data on the kinetics of adsorption from water phase for nitrobenzene, p-nitroaniline and quinoxaline for the three activated carbons. The experiments, that were carried out in order to obtain these data, were batch uptake experiments, in which the concentration in the aqueous solution was monitored during the adsorption process. A surface diffusion theory, based on the Maxwell-Stefan equations, was used to model the experimental data. Molecular diffusion in macro-pores and surface diffusion in micro-pores, were assumed to take place in parallel. The Maxwell-Stefan surface diffusion coefficient was shown to have a large dependence, of several orders of magnitude, on the amount adsorbed. One explanation for this is that at low concentrations, the adsorbate is strongly bound in small pores, near the pore walls, and has a small mobility. At high concentrations, the adsorbate is also located in larger pores and farther away from the pore walls, resulting in a higher mobility. Another explanation is that the transport by molecular diffusion in macro-pores and the transport in micro-pores, that may be viewed as capillary transport or surface diffusion, take place in series. The micro-pore transport is the faster mechanism and will become more dominant at higher carbon loading. This results in a larger surface diffusion coefficient.

In chapter 6, the fairly new application of magnetic resonance imaging (MRI) for the measurement of adsorption kinetics of nitrobenzene onto activated carbon is discussed. MRI makes it possible to measure directly the concentration profiles of the adsorbate in the activated carbon. Two experiments were carried out. The first one is the adsorption from the vapour phase. The second experiment is the adsorption from heavy water solution. The results of the latter experiment show reasonable agreement with the results obtained from the experimental method of chapter 5. A big advantage of the MRI experiments is that they are several orders of magnitude less time consuming than the experiments of chapter 5.

Also, a  $T_2$ -study of nitrobenzene on activated carbon was made with MRI. Nitrobenzene shows three  $T_2$  peaks. One of them can be attributed to nitrobenzene inside macro-pores. The other two peaks are caused by nitrobenzene in micro-pores. It is likely that one of those peaks originates from molecules in the first layer near the pore-wall and that the other one originates from molecules that are located farther away from the pore wall.

To obtain better information about the adsorption process with MRI, it is desired to measure the adsorption profiles with a higher resolution and to measure the  $T_2$  data with less noise. This should be possible by applying a stronger external magnetic field or by using a larger carbon sample.

# Samenvatting

Adsorptie is een belangrijke technologie in het scheiden en zuiveren van producten. Het is vaak de 'value-adding' step in de proces industrie. Ook gezien de recente ontwikkelingen van nieuwe materialen, zoals zeolieten en micro-poreuze membranen, bestaat de behoefte om een beter inzicht te krijgen in adsorptie processen.

De basisdoelstelling van de studie in dit proefschrift is een bijdrage te leveren aan het begrijpen en modelleren van de evenwichten en kinetiek van adsorptie processen. Speciale aandacht gaat uit naar fasenscheiding in poreuze materialen.

In hoofdstuk 1 wordt een korte introductie betreffende adsorptie-processen gegeven.

Hoofdstuk 2 bediscussieert de eigenschappen van de materialen die gebruikt werden in deze studie. Dit waren 3 typen actieve kool en enkele adsorbaten. De adsorbaten waren allen organisch, namelijk, nitrobenzeen, p-nitroaniline, quinoxaline, benzeen en pyridine. Stikstof adsorptie-experimenten en kwikporosimetrie-experimenten werden uitgevoerd om de actieve kool te karakteriseren. De waterfase sorptie-isothermen van de organische adsorbaten werden bij verschillende temperaturen gemeten. Ze werden gemodelleerd met een Radke-Prausnitz isotherm. Deze bleek de experimentele data over een groot gebied, vergeleken met populaire modellen als Langmuir, Freundlich en Jossens, goed te beschrijven.

In hoofdstuk 3 wordt de Kierlik-Rosinberg-'density functional theory' gebruikt voor de berekening van multi-component sorptie-evenwichten van eenvoudige Lennard-Jones moleculen in een slit-porie. Het model toont aan dat er verschillende mechanismen bestaan waarmee een porie gevuld kan worden. Dit is afhankelijk van moleculaire interacties, porie-grootte en de temperatuur. De verschillende mechanismen zijn: continue porie-vulling, filmlaag-vorming en capillaire fasenscheiding.

De 'density functional theory' werd ook gebruikt om de poriegrootte-verdeling van de verschillende koolsoorten te berekenen, uitgaande van de gemeten stikstof sorptie-isothermen. De berekende poriediameters zijn ongeveer twee keer zo groot als die berekend met de Horvath-Kawazoe methode. Horvath-Kawazoe is een veel gebruikte methode om poriegrootte-verdelingen van actieve kool te berekenen. Het bepalen van de poriegrootte-verdeling kan belangrijke consequenties hebben voor het begrip van de adsorptie-kinetiek, omdat de poriën slechts enkele molecuuldiameters groot zijn. De beweeglijkheid van moleculen direct tegen de poriewand wijkt namelijk aanzienlijk af van die van de moleculen die zich verder van de wand bevinden.

In hoofdstuk 4 wordt een nieuw model geïntroduceerd voor de berekening van de interne adsorptie-kinetiek voor adsorptie vanuit de waterfase. In tegenstelling tot de gebruikelijke modellen, die gebaseerd zijn op oppervlakte-diffusie, is dit model gebaseerd op de capillaire stroming van capillair fasengescheiden adsorbaat. Het model wordt toegepast op experimentele data uit de literatuur

van de adsorptie van nitrobenzeen en benzonitril vanuit de waterfase aan actieve kool. Het model geeft een goede voorspelling van de temperatuur- en beladingsafhankelijkheid van de effectieve diffusiecoëfficiënt.

Hoofdstuk 5 presenteert data betreffende de kinetiek van adsorptie vanuit de waterfase voor de adsorbaten nitrobenzeen, p-nitroaniline en quinoxaline voor de drie verschillende koolsoorten. De data werden verkregen via batch uptake experimenten, waarbij de concentratie in de waterfase werd gevolgd tijdens het adsorptie proces. Een oppervlaktediffusie-theorie, gebaseerd op de Maxwell-Stefan oppervlaktediffusie-coëfficiënt, werd gebruikt om de experimentele data te modelleren. Moleculaire diffusie in de macro-poriën en diffusie in de micro-poriën werden parallel verondersteld. De dusdanig gevonden Maxwell-Stefan oppervlaktediffusie-coëfficiënt varieerde enkele ordegroottes met variërende geadsorbeerde hoeveelheid. Een verklaring hiervoor is dat bij lage concentraties het adsorbaat sterk gebonden is in de kleine poriën dicht tegen de poriewand. Dus heeft het een lage mobiliteit. Bij hoge concentraties zit het adsorbaat ook in grotere poriën en verder verwijderd van de poriewand. Dit resulteert in een hogere mobiliteit van de moleculen. Een andere verklaring is dat het transport door moleculaire diffusie in macro-poriën en het transport in de micro-poriën in serie plaatsvinden. Het micro-porie transport, dat gezien kan worden als oppervlakte-diffusie of als capillair transport, is het snellere mechanisme en wordt dominant bij hogere hoeveelheid geadsorbeerde stof. Dit leidt tot een hogere oppervlakte-diffusiecoëfficiënt in het parallel-model.

In hoofdstuk 6 wordt de relatief nieuwe toepassing van MRI voor het meten van adsorptie-kinetiek besproken. MRI werd gebruikt om direct de concentratie-profielen van nitrobenzeen in actieve kool te meten gedurende een adsorptie-experiment. Er werden twee verschillende experimenten uitgevoerd. Het eerste was de adsorptie van nitrobenzeendamp aan actieve kool. Het tweede experiment was adsorptie vanuit een zwaar water oplossing. De resultaten van het tweede experiment komen redelijk overeen met de resultaten die verkregen werden uit de batch uptake experimenten zoals beschreven in hoofdstuk 5. Een groot voordeel van de MRI experimenten is dat ze enkele ordegroottes minder tijdrovend zijn dan de batch uptake experimenten.

Er werd ook een  $T_2$ -analyse gemaakt van nitrobenzeen in actieve kool. Nitrobenzeen geeft drie  $T_2$ -pieken. Eén van deze pieken kan worden toegeschreven aan nitrobenzeen dat zich in de macro-poriën bevindt. De andere twee pieken worden veroorzaakt door nitrobenzeen in de micro-poriën. Het is waarschijnlijk dat één van deze pieken afkomt van moleculen die zich direct tegen de poriewand bevinden. De andere piek wordt dan veroorzaakt door moleculen die zich niet direct aan de poriewand bevinden.

Om betere informatie over adsorptie-processen te verkrijgen met MRI experimenten, is het nodig om de adsorptie-profielen met een hogere resolutie en de  $T_2$  data met relatief minder ruis meten. Dit moet mogelijk zijn door het toepassen van een sterker extern magnetisch veld of door een groter monster te gebruiken.

# Contents

<b>1. Introduction</b>	<b>1</b>
1.1. Adsorption processes	1
1.2. Objective of the study	1
1.3. Outline of the thesis	1
References	2
<b>2. Material properties</b>	<b>4</b>
2.1. Introduction	4
2.2. Adsorbates	4
2.3. Adsorbents	5
2.3.1. Physical properties	5
2.3.2. Characterisation of adsorbents with nitrogen adsorption	5
2.3.3. Characterisation of adsorbents with mercury porosimetry	9
2.4. Sorption isotherms	9
2.4.1. Measurement method	9
2.4.2. Modelling of the isotherms	10
2.4.2.1 Radke-Prausnitz isotherm	10
2.4.2.2 The potential theory	10
2.4.3. Results and discussion	11
References	20
Symbols	20
<b>3. Adsorption equilibria with density functional theory</b>	<b>21</b>
3.1. Introduction	21
3.2. The Kierlik-Rosinberg DFT	22
3.2.1. The grand potential energy functional	22
3.2.2. Minimisation of the grand potential energy functional	24
3.2.3. Bulk	27
3.2.3.1. The bulk chemical potential	27
3.2.3.2. The bulk pressure	28
3.2.3.3. Bulk phase separation, gas-liquid and liquid-liquid phase equilibria	29
3.2.4. Adsorption of a Lennard-Jones fluid in a slit pore	30
3.3. Calculations and pore filling mechanisms	34
3.3.1. Introduction	34
3.3.2. Nitrogen adsorption in a slit pore	40
3.3.2.1. Introduction	40
3.3.2.2. Bulk properties	40
3.3.2.3. Adsorption in an infinite slit pore	41
3.3.2.4. The use of DFT data to calculate pore size distributions from sorption isotherms of the carbons used in this study	45
3.3.3. Multi-component adsorption in a carbon slit pore	50
3.3.3.1. Results	50
3.3.3.2. Discussion	56
References	60
Symbols	61

<b>4. Capillary transport in adsorption from liquid phase on activated carbon</b>	<b>64</b>
4.1. Introduction	64
4.2. Theory	68
4.2.1. Model I: Continuous capillary transport	68
4.2.2. Model II: Discontinuous capillary transport	70
4.3. Results and discussion	72
4.4. Conclusions	76
References	76
Symbols	78
<b>5. Uptake experiments</b>	<b>79</b>
5.1. Introduction	79
5.2. Equipment	79
5.3. Experiments in small concentration steps	80
5.4. Maxwell-Stefan diffusion model for transport in porous media	81
5.4.1. Theory	81
5.4.2. Solving the equations	84
5.5. Results and discussion	86
References	92
Symbols	92
<b>6. The application of <sup>1</sup>H-MRI to measurement of adsorption processes</b>	<b>94</b>
6.1. Introduction to Magnetic Resonance Imaging (MRI) techniques	94
6.2. Measurement of nitrobenzene adsorption profiles with the aid of <sup>1</sup> H-MRI	97
6.2.1. Introduction	97
6.2.2. Equipment	98
6.2.2.1. The adsorption process	98
6.2.2.2. The MRI equipment and parameters	99
6.2.3. Results	99
6.2.3.1. Calibration curve	99
6.2.3.2. Nitrobenzene profiles as a function of time	101
6.2.3.3. T <sub>2</sub> -data	101
6.2.4. Discussion and conclusions	105
6.2.4.1. Determination of the diffusion coefficient	105
6.2.4.2. T <sub>2</sub> -analysis	106
6.3. Measurement of nitrobenzene adsorption profiles on activated carbon saturated with D <sub>2</sub> O with the aid of <sup>1</sup> H-MRI	109
6.3.1. Introduction	109
6.3.2. The experiment	109
6.3.3. Results and discussion	109
6.3.3.1. Adsorption profiles from MRI measurements	109
6.3.3.2. Adsorption profiles from the batch uptake experiments	110
References	112
Symbols	113
<b>7. General conclusions</b>	<b>114</b>
<b>Appendix 1</b>	<b>116</b>
<b>Dankwoord</b>	<b>118</b>
<b>Curriculum Vitae</b>	<b>119</b>



# 1. Introduction

## 1.1. Adsorption processes

The value-adding step in the process industry is often found in the separation and purification of products. Adsorption technology has an important share in this step. Also, adsorption is important in the removal of undesired components from, for example wastewater and air streams. There are many materials, both from nature and from synthesis, that have sorption capacity. The most important commercial adsorbents are activated carbon, molecular-sieve zeolites, silica gel and activated alumina. The applications for these adsorbents depend on their particular sorptive properties [Crittenden and Thomas, 1998, p.28].

Applications of the use of activated carbon are, among other things: recovery of nitrogen from air, ethene from methane and hydrogen, removal of odours from gases, in gas masks and water purification, including removal of phenol, halogenated compounds, pesticides, caprolactam and chlorine.

Zeolites are distinct from other adsorbents in that, for each type, there is no distribution of pore size because the crystal lattice into which the adsorbate molecules can or cannot enter is precisely uniform. For this reason, zeolites are capable of separating effectively on the basis of molecular size. They are used, among others for the separation of oxygen and argon, separation of normal from branched paraffins, drying of gases and removing water from azeotropic mixtures.

Silica gel and activated alumina are used for the drying of gases, organic solvents and transformer oils.

## 1.2. Objective of the study

The basic objective of the study in this thesis is to contribute to the understanding and modelling of the equilibria and kinetics of adsorption processes. Special attention is given to phase separation phenomena inside a porous material.

Sorption kinetics and equilibria were widely studied the past century. This resulted in important developments as the Dubinin-Polanyi [Dubinin and Astakhov, 1971] potential theory. In addition, a breakthrough was the recognition of the importance of considering the chemical potential gradient, rather than the concentration gradient, as the driving force for transport in adsorption systems [Habgood 1958; Krishna, 1993]. This resulted in the widespread use of the Maxwell-Stefan equations in adsorption modelling.

The development of special micro-porous membranes and zeolites has contributed to a more extensive use of adsorption processes in separation technology. This also motivates the need for better understanding of adsorption principles.

With the increase of computational power, detailed calculations can be performed on molecular scale. The main methods are molecular dynamics,

Monte Carlo and density functional calculations. These methods have led to insights, in the adsorption mechanism, that could not be obtained from experimental methods [Vlugt, 2000; Lastoskie et al., 1993].

On the experimental level, Magnetic Resonance Imaging is a promising tool that has not been applied extensively in studying adsorption processes yet. It can be used to investigate sorption kinetics [Ruthven, 2000].

In this study, use was made of several of the developments in adsorption that were described above in order to gain understanding in adsorption processes.

### **1.3. Outline of the thesis**

The model material that is used in this study is activated carbon. Even though its porous structure is very complicated, it was chosen because it is the most used adsorbent, world-wide.

In chapter 2, the different kinds of activated carbon, used in the study, are characterised. Liquid-phase sorption isotherms of several aromatic adsorbates were measured.

In chapter 3, the Kierlik and Rosinberg [1991] density functional theory is used to gain understanding in adsorption equilibria of one or two components in an infinite slit pore. The influence of temperature and pore size was studied. In addition, the effects of the interactions between the adsorbed component and the pore-wall and the interactions between components mutually were investigated.

In chapter 4, a new model is put forward for calculation of the intra-particle kinetics for adsorption from the liquid phase. Contradictory to the usual models, which are based on surface diffusion, this one is based on the capillary flow of capillary phase separated adsorbate.

Chapter 5 treats the experimental kinetics of the adsorption from liquid phase for several activated carbons and aromatic adsorbates. Batch uptake experiments were carried out in small concentration steps to determine the kinetics as a function of the amount adsorbed. A surface diffusion theory, based on the Maxwell-Stefan equations, was used to model the experimental data.

In chapter 6, the fairly new application of magnetic resonance imaging for the measurement of adsorption kinetics is discussed. The kinetics of nitrobenzene adsorption onto activated carbon were measured from both gas and liquid phase. In the latter case, a comparison was made with the conventional experimental method of chapter 5.

### **References**

Crittenden, Barry and Thomas, W. John; 'Adsorption technology and design, Butterworth-Heinemann', Oxford, 1998.

Dubinin, M.M. and Astakhov, Y.A.; Adv. Chem. Ser., 102, pp. 69-85, 1971.

Habgood, H.W.; 'The kinetics of molecular sieve action. Sorption of nitrogen-methane mixtures by Linde molecular sieve 4A', Can. J. Chem., 36, pp. 1384-1397, 1958.

Kierlik, E. and Rosinberg, M.L.; 'Density-functional theory for inhomogeneous fluids: Adsorption of binary mixtures', *Physical review A*, 44, no. 8, pp. 5025-5037, 1991.

Krishna R.; 'Problems and pitfalls in the use of the Fick formulation for intra-particle diffusion', *Chem. Eng. Sci*, Vol. 48, No. 5, p.845, 1993.

Lastoskie, C., Gubbins, K.E., and Quirke, N.; 'Pore size heterogeneity and the carbon slit pore: a density functional theory model', *Langmuir* 9, pp. 2693-2702, 1993.

Ruthven, D.M., 'Past progress and future challenges in adsorption research', *Ind. Eng. Chem. Res*, 39, pp. 2127-2131, 2000.

Vlugt, Thijs J.H.; 'Adsorption and diffusion in zeolites: A computational study', PhD. Thesis, University of Amsterdam, 2000.

## 2. Material properties

### 2.1. Introduction

In this section, the properties of the adsorbates and adsorbents, that were used in this study, are presented. The adsorbents were characterised with nitrogen adsorption and mercury porosimetry experiments.

The adsorbates that were used are benzene derivatives, having different properties with respect to a.o. melting point and solubility in water.

Benzene derivatives are common pollutants in potable and wastewater. They can be effectively removed from water with the aid of activated carbon, which is one of the most important types of adsorbent. This is due to its low raw material costs, its large internal surface area and because it is non-hazardous.

Three types of activated carbon were used in this study. The aqueous phase sorption isotherms of the adsorbates, in combination with the different activated carbons, were measured at several temperatures.

### 2.2. Adsorbates

The adsorbates that were chosen for this study are quinoxaline (QNX), nitrobenzene (NBZ), p-nitroaniline (PNA), benzene (BZ) and pyridine (PYR). Their structural formulas are given below:

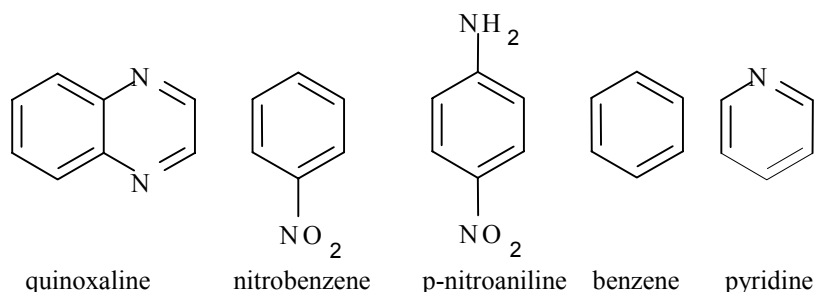


Fig. 2.2-1 Structural formulas of the used adsorbates

NBZ and PNA are often used in adsorption research, which makes it easy to obtain additional information on them. NBZ is a liquid at room temperature. PNA has a melting point of 149°C. QNX has a melting point at 32°C. This way it is possible to perform experiments with QNX in an aqueous environment above and below the melting point. In addition, NBZ and PNA are poorly soluble in water while QNX is very well soluble in water. All atoms of the three molecules are almost positioned in the flat benzene plane. For PNA and NBZ, it has been shown that they are reversibly adsorbed onto activated carbon [Tamon and Okazaki, 1996].

BZ is poorly soluble in water while PYR is completely miscible with water at room temperature. Because their structural formulas are very similar, this makes an interesting comparison.

Some more detailed information on the adsorbates is given in table 2.2-1.

**Table 2.2-1** Characteristics of adsorbates

Characteristics	Unit	QNX	PNA	NBZ	BZ	PYR
Molecular weight	kg.mole <sup>-1</sup>	0.1301	0.1381	0.1231	0.0781	0.0791
Melting point	°C	29-32	149	6	5.5	-42
Boiling point	°C		332	211	80.1	115
Density at 20°C	kg.m <sup>-3</sup>	1133	1424	1204	879	982
$C_s$ at 20 °C	kg.kg <sup>-1</sup> <sub>water</sub>	0.457	0.5*10 <sup>-3</sup>	1.9*10 <sup>-3</sup>	0.7*10 <sup>-3</sup>	∞
$D_{a,w}$ at 20 °C	10 <sup>-10</sup> m <sup>2</sup> s <sup>-1</sup>	-	9.26	9.25	-	-

$D_{a,w}$  is the bulk diffusivity of the adsorbate in water, from Kouyoumdjiev [1992, p. 63].

$C_s$  is the solubility of the adsorbate in water

## 2.3. Adsorbents

### 2.3.1. Physical properties

Three types of activated carbon were used in this study. All were in extruded form and had a cylindrical shape. The activated carbons RWB1 and AP4-60 were manufactured for removal of organic pollutants from industrial as well as municipal wastewater. The AC R1-extra was manufactured for gas separations.

Physical properties of both carbons are given in table 2.3.1-1.

**Table 2.3.1-1** Physical properties of the activated carbons

Parameter	Unit	RWB1	R1 extra	AP4-60
Length	10 <sup>-3</sup> m	≅3	≅3	≅10
Diameter	10 <sup>-3</sup> m	1	1	4
Manufacturer		Norit B.V.	Norit B.V.	Chemviron
Particle density <sup>1</sup>	kg.m <sup>-3</sup>	710	556	740
N <sub>2</sub> micropore capacity <sup>2</sup>	kg <sub>N2</sub> .kg <sup>-1</sup> <sub>c</sub>	0.44	0.69	0.50
Micropore volume <sup>2</sup>	m <sup>3</sup> .m <sup>-3</sup> <sub>c</sub>	0.39	0.47	0.46
Macropore volume <sup>3</sup>	m <sup>3</sup> .m <sup>-3</sup> <sub>c</sub>	0.20	0.26	0.20

<sup>1</sup> determined from mercury porosimetry experiments

<sup>2</sup> explanation follows in section 2.3.2.

<sup>3</sup> explanation follows in section 2.3.3.

### 2.3.2. Characterisation of adsorbents with nitrogen adsorption

The carbons were characterised by performing nitrogen sorption measurements with a Coulter Omnisorp 100. The experiments were performed at 77K, the boiling point of nitrogen at atmospheric pressure.

The sorption isotherms are shown in figure 2.3.2-1. Here  $T$  is the absolute temperature,  $R_g$  is the gas constant [J.mole<sup>-1</sup>.K<sup>-1</sup>] and  $P$  is the nitrogen vapour pressure [Pa].  $P_0$  is the saturated nitrogen vapour pressure, which is atmospheric at this temperature.

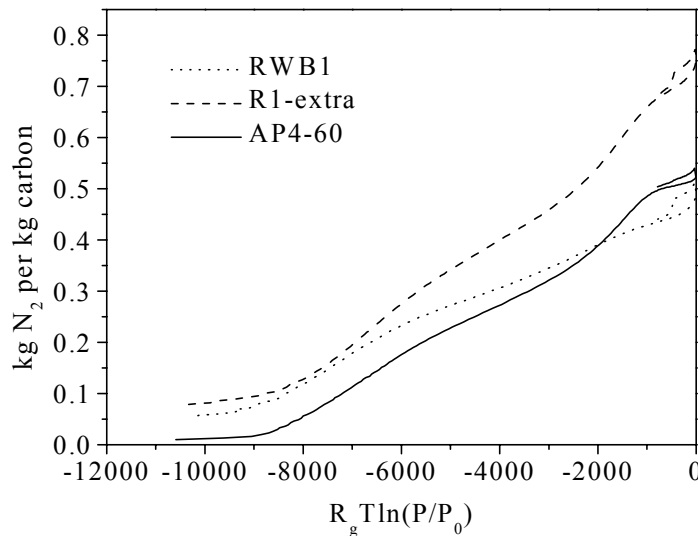


**Fig. 2.3.2-1** N<sub>2</sub> sorption isotherms at 77K for the activated carbons RWB1, R1 extra and AP4-60.

In view of the isotherms, it is observed that a significant amount of nitrogen was already adsorbed on the carbons RWB1 and R1-extra at very low pressures (0.01 Pa). The hysteresis loop of all three isotherms closes at  $P/P_0=0.45$ , which is common for nitrogen adsorption [Gregg and Sing, 1980, p.154]. Below this pressure, the pore filling mechanism is so-called micro-pore filling, for which no hysteresis occurs. Micro-pores have a diameter of less than 2 nm. The micro-pore capacity of each carbon for nitrogen was read from the adsorption isotherm at  $P/P_0=0.45$ . These are tabulated in table 2.3.1-1. Note the large difference between the micro-pore capacities of AC RWB1 and AC R1 extra. The micro-pore volume per volume of carbon particle was calculated by approximating the density of adsorbed nitrogen with its liquid bulk density at 77K ( $808 \text{ kg.m}^{-3}$ ). The results are shown in table 2.3.1-1. When the nitrogen pressure exceeds  $P/P_0=0.45$  meso-pores are filled by means of capillary condensation. In view of the figures, it is concluded that the meso-pore volume of the three carbons was quite small compared to the micro-pore volume.

The micro-pore size distribution of each activated carbon was calculated with the Horvath and Kawazoe method [Horvath and Kawazoe, 1983]. This approach was used to obtain the average potential energy for a slit shape pore from which a method was derived to determine the micro-pore size distribution from the information of experimental isotherm data.

The working equation [Do, 1998, p. 319] runs as follows:

$$R_g T \ln\left(\frac{P}{P_0}\right) = N_{AV} \frac{N_1 A_1 + N_2 A_2}{\sigma^4 (d - (\sigma_1 + \sigma_2))} \times \left[ \frac{\sigma^{10}}{9 \left(\frac{\sigma_1 + \sigma_2}{2}\right)^9} - \frac{\sigma^4}{3 \left(\frac{\sigma_1 + \sigma_2}{2}\right)^3} - \frac{\sigma^{10}}{9 \left(d - \frac{\sigma_1 + \sigma_2}{2}\right)^9} + \frac{\sigma^4}{3 \left(d - \frac{\sigma_1 + \sigma_2}{2}\right)^3} \right] \quad (2.3.2-1)$$

In equation 2.3.2-1,  $d$  is the diameter of the slit pore from pore wall centre to pore wall centre.  $N_{AV}$  is the Avogadro number. A pore with diameter  $d$  will be filled with nitrogen when in equilibrium with a bulk phase pressure that is larger than  $P/P_0$ .

The parameters  $N_1$ ,  $N_2$ ,  $A_1$  and  $A_2$  were obtained from Do [1998, p. 319]. The Lennard-Jones diameters of the adsorbent atom, carbon and of the adsorbate atom, nitrogen are respectively  $\sigma_1=0.34$  nm and  $\sigma_2=0.357$  nm. Thus, the effective pore width is  $d-\sigma_l$ .

For

$$\sigma \equiv \left(\frac{2}{5}\right)^{1/6} \frac{\sigma_1 + \sigma_2}{2} \quad (2.3.2-2)$$

it is calculated that  $\sigma=0.299$  nm. Substituting all parameters in the working equation, it follows that

$$\ln\left(\frac{P}{P_0}\right) = \frac{44.44}{2d - 0.697} \times \left[ \frac{2.664 \times 10^{-3}}{(2d - 0.3485)^3} - \frac{6.3456 \times 10^{-7}}{(2d - 0.3485)^9} - 0.05457 \right] \quad (2.3.2-3)$$

The micro-pore size distributions of the three activated carbons are shown in figure 2.3.2-2.

A more detailed analysis of the nitrogen isotherms is made in section 3.3.2 with the aid of density functional theory.

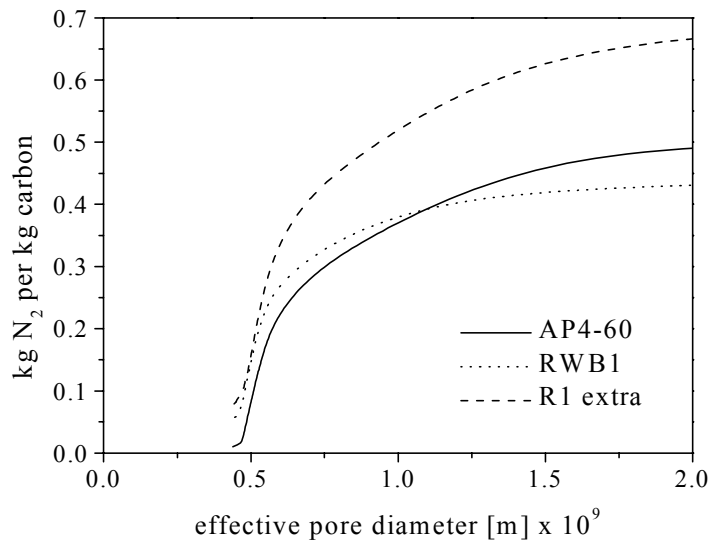


**Fig. 2.3.2-2** Cumulative amount of nitrogen adsorbed as a function of pore size for the activated carbons RWB1, R1 extra and AP4-60, calculated with the Horvath Kawazoe method from the N<sub>2</sub> sorption isotherms at 77K.

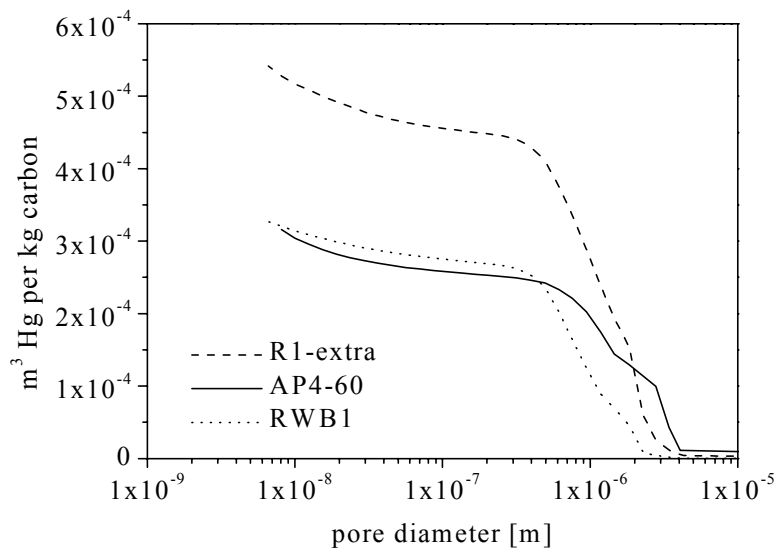


**Fig. 2.3.3-1** Cumulative pore size volumes for the activated carbons RWB1, R1 extra and AP4-60, calculated with the Washburn equation from mercury intrusion experiments.

### **2.3.3. Characterisation of adsorbents with mercury porosimetry**

The carbons were characterised by performing mercury porosimetry experiments with a Micromeritics Autopore IV 9500 apparatus. The experiments were performed using the carbon particles in extruded form. Cumulative pore size volumes were calculated from the intrusion experiments with the Washburn equation [Gregg and Sing, 1982, p. 175] for cylindrical pores.

The results are shown in figure 2.3.3-1.

It becomes clear from figure 2.3.3-1 that AC R1-extra has a high macro-pore volume compared to the other two carbons. The dimensions of most of the macro-pores vary roughly from 4 to 0.4 micrometer. The macro-pore volume is calculated as the volume of all pores larger than 50 nm, which is the definition of a macro-pore. The values for the different carbons are given in table 2.3.1-1. Also from the mercury intrusion experiments, it is concluded that the mesoporous (pores with a diameter between 2 and 50 nm) volume is relatively small.

## **2.4. Sorption isotherms**

### **2.4.1. Measurement method**

The sorption isotherms of the adsorbates, mentioned in section 2.2, were determined by the conventional method. The crushed adsorbent was put in an Erlenmeyer flask and 200 ml of adsorbate solution was added. The Erlenmeyer flask was sealed and placed in a Lab-Line Environ-Shaker at the desired temperature and agitated at 250 rpm for two or three weeks to make sure equilibrium had been reached.

After this time, the shaker was stopped, enabling the carbon particles to deposit. This was done because the solution had to be filtered. During filtering the temperature of the solution might change, which would influence the equilibrium. Also, carbon particles in the solution silt up the filter, making filtering a slower process. Thus the solution was decanted so that almost no carbon particles were left in it. Then the solution was pressed through a, for the adsorbates inert, membrane filter (Schleicher and Schüll, diameter 47mm, pore diameter 0,45  $\mu\text{m}$ ).

The filtered solution was analysed with a Beckman DU-64 single-beam spectrophotometer with a wavelength range of 200 to 900nm at for the adsorbate characteristic minima and maxima in the light spectrum. With the aid of a calibration curve, the concentration was determined. Because the minima in the spectrum of PNA coincide with the maxima in the spectrum of NBZ and the other way around, it was possible to determine the independent concentrations of the components when both were present in the same aqueous solution. This way it was possible to measure the multi-component sorption isotherm for this combination of components.

## 2.4.2. Modelling of the isotherms

### 2.4.2.1. Radke-Prausnitz isotherm

The Radke-Prausnitz model [Radke and Prausnitz, 1972], was used to fit the isotherm data. The Radke-Prausnitz equation runs as follows:

$$Q = \frac{K_{RP} C}{1 + (K_{RP} / F_{RP}) C^{1-N_{RP}}} \quad (2.4.2-1)$$

$Q$  is the carbon loading in kg adsorbate per kg adsorbent.  $C$  [kg.m<sup>-3</sup>] is the adsorbate concentration in the solvent.  $K_{RP}$ ,  $F_{RP}$  and  $N_{RP}$  are the model parameters, which are obtained by a non-linear statistical fit of the equation to the experimental data.

The Radke-Prausnitz equation has several important properties which make it suitable for use in many adsorption systems. At low concentrations it reduces to a linear isotherm. At high concentrations it becomes the Freundlich isotherm and for the special case of  $N_{RP} = 0$  it becomes the Langmuir isotherm. This Radke-Prausnitz model gives a good fit over a wide concentration range and was therefore preferred above isotherm models like Langmuir, Freundlich and Jossens.

### 2.4.2.2. The potential theory

The potential theory is especially useful for adsorption of non-polar components on micro-porous materials such as activated carbon. The theory interprets the sorption isotherm via a characteristic curve that is independent of temperature. This way it is possible to make predictions about the temperature dependence of the sorption isotherm.

Polanyi [Polanyi, 1932] proposed the concept of a pore wall surface force field that can be represented by equi-potential contours above the surface, and that the space between each set of equi-potential surfaces corresponds to a definite adsorbed volume per kg of adsorbent,  $W$ , with

$$W = nV_m \quad (2.4.2-2)$$

Here,  $n$  is the number of moles adsorbed per unit mass of sorbent and  $V_m$  the molar volume of adsorbate in the adsorbed phase.

As a consequence of the equi-potential contours, the cumulated volume of the adsorbed space is a function of the adsorption potential,  $\varepsilon$  [J.mole<sup>-1</sup>]. This is the difference between the chemical potentials of the adsorbate, in the state of a normal liquid, and the adsorbate, in the adsorbed state, at the same temperature. Then for low solute concentrations of the adsorbate

$$\varepsilon = R_g T \ln \frac{C}{C_s} \quad (2.4.2-3)$$

In which  $C_s$  [kg.m<sup>-3</sup>] is the adsorbate solubility.

The characteristic curve is found by plotting  $nV_m$  against  $R_g T \ln \frac{C}{C_s}$ .

According to the theory, sorption isotherms at different temperatures should result in one characteristic curve.

### 2.4.3. Results and discussion

The results of the measured single component isotherms are shown in figures 2.4.3-1 to 2.4.3-8. Also the Radke-Prausnitz fits are shown in the figures. The fitting data are given in table 2.4.3-1 For PNA and NBZ, which have a low solubility in water, the isotherms at different temperatures were also plotted according to the potential theory. The molar volumes were assumed to have negligible temperature dependence in the temperature range of 293K to 323K. Thus the adsorbed volume  $W$  is directly proportional to carbon loading  $Q$  in [ $\text{kg}_{\text{adsorbate}} \cdot \text{kg}^{-1} \text{c}$ ].

**Table 2.4.3-1** Radke-Prausnitz parameters for isotherm fits

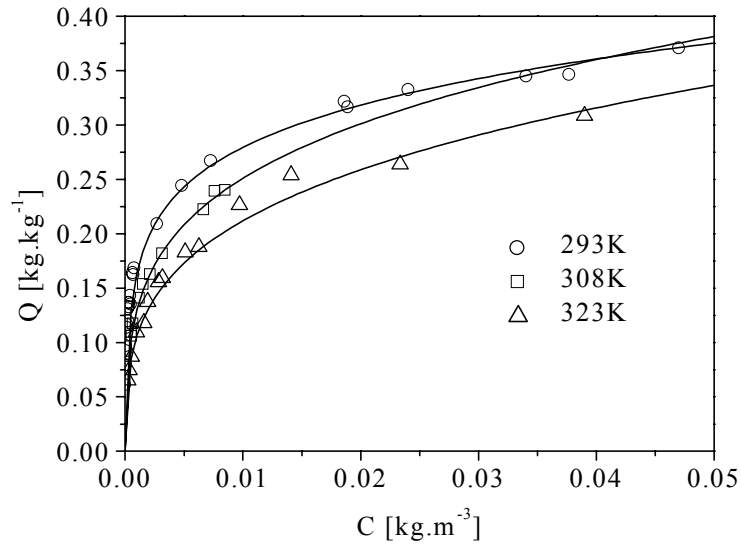
Adsorbate	AC	T	$K_{\text{RP}}$	$F_{\text{RP}}$	$N_{\text{RP}}$
NBZ (fit 1)	RWB1	293	1042	0.631	0.171
NBZ (fit 2)	RWB1	293	$6.40 \cdot 10^6$	0.508	0.142
NBZ	RWB1	308	1363	0.816	0.252
NBZ	RWB1	323	2093	0.788	0.283
NBZ	R1 extra	293	372	0.778	0.155
NBZ	R1 extra	323	677	0.792	0.244
NBZ	AP4-60	293	1349	0.843	0.301
PNA	RWB1	293	754	0.456	0.091
PNA	RWB1	323	4605	0.540	0.159
PNA	R1 extra	293	3289	0.817	0.169
PNA	R1 extra	323	391	0.611	0.143
QNX	RWB1	293	2318	0.372	0.111
QNX	RWB1	323	835	0.347	0.144
QNX	R1 extra	293	155764	0.510	0.144
QNX	R1 extra	323	4073	0.403	0.144
BZ	RWB1	293	7.47	0.451	0.016
PYR	RWB1	293	7.87	0.139	0.181

Figure 2.4.3-1c shows the nitrobenzene isotherm on AC RWB1 at 293K, which was measured over a wide concentration range. It is clear that the Radke-Prausnitz isotherm is not a good model for the whole concentration range. However, over a smaller concentration range, it models the isotherm data well for all adsorbate/adsorbent systems that were investigated.

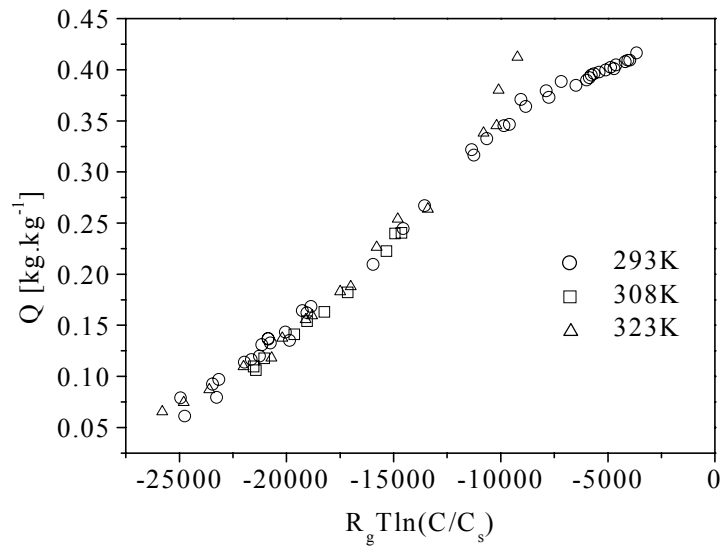
Nitrobenzene seems to obey well to the potential theory in case of both the activated carbons RWB1 and R1-extra (figs. 2.4.3-1b and 2.4.3-2b). However, for PNA, not one characteristic curve was found in the potential plot. The curve at 323K lies higher than that at 293K for both carbons. If the temperature dependence of the molar volume had been taken into account, the difference would be even bigger, because the molar volume increases with temperature.

Figure 2.4.3-8 shows that benzene is much better adsorbed than pyridine on the activated carbon RWB1, from an aqueous solution. This was to be expected since the benzene is less soluble in water than pyridine.

The multi-component isotherm of the system PNA/NBZ on AC RWB1 at 293K is shown in figure 2.4.3-9. Theories for adsorption equilibria in multi-component systems are not as advanced as those for single component systems. The slow progress in this area is due to a number of reasons [Do, 1998, p. 248], among which: the lack of experimental data for multi-component systems and a solid surface that is too complex to model adequately.



**Fig. 2.4.3-1a** Sorption isotherms of nitrobenzene on AC RWB1. The lines are the Radke-Prausnitz fits. Its parameters are given in table 2.4.3-1.



**Fig 2.4.3-1b** Potential plot of sorption isotherms of nitrobenzene on AC RWB1.

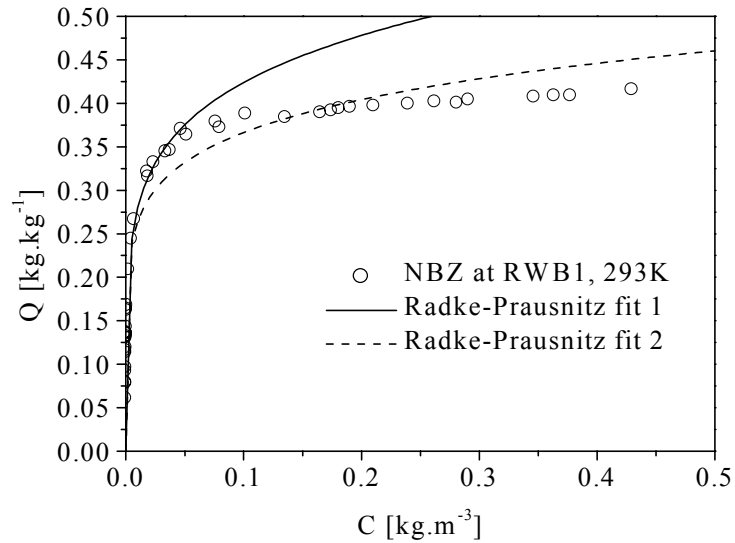


**Fig 2.4.3-1c** Sorption isotherms of nitrobenzene on AC RWB1 over wide concentration range. Fit 1 is Radke-Prausnitz fit of data points in fig. 2.3.4.1a. For fit 2 all data points were taken into account.

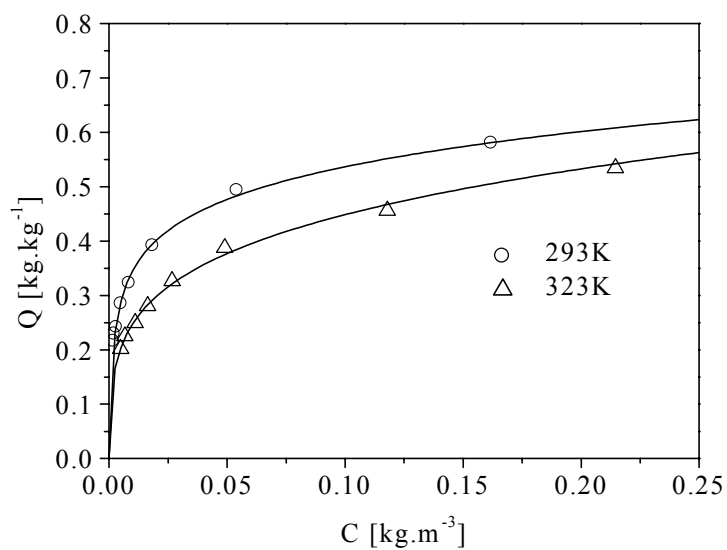


**Fig. 2.4.3-2a** Sorption isotherms of nitrobenzene on AC R1 extra. The lines are the Radke-Prausnitz fits. Its parameters are given in table 2.4.3-1.

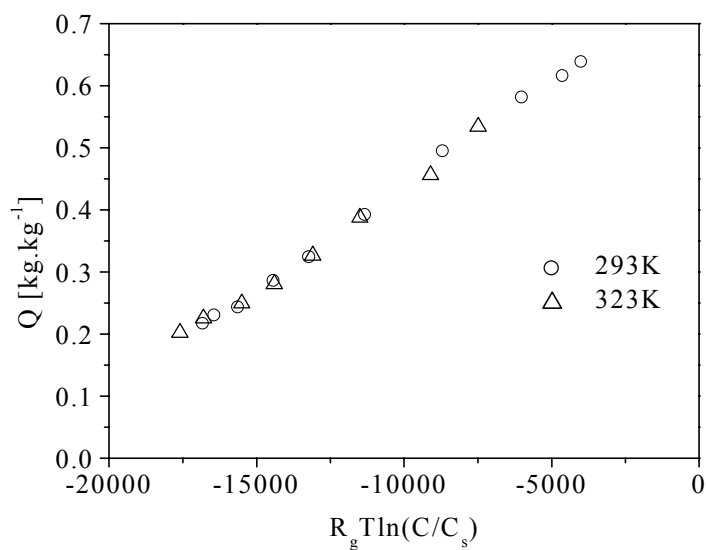


**Fig. 2.4.3-2b** Potential plot of sorption isotherms of nitrobenzene on AC R1 extra.

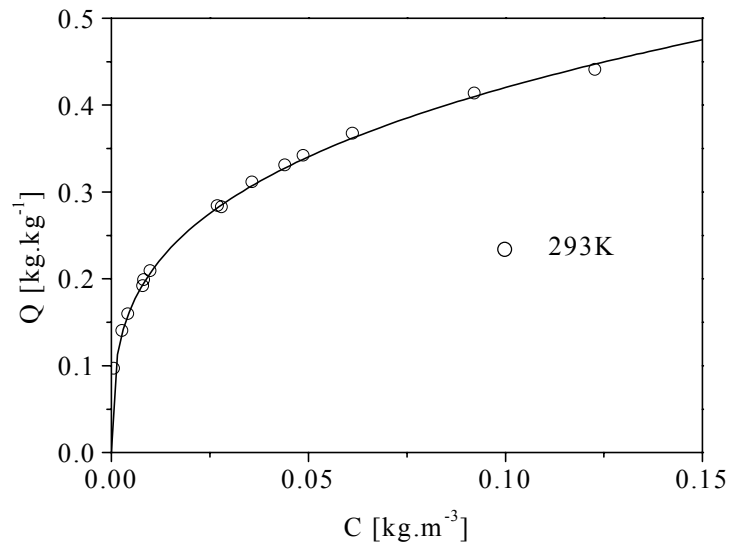


**Fig 2.4.3-3** Sorption isotherm of nitrobenzene on AC AP4-60 at 293K. The line is the Radke-Prausnitz fit. Its parameters are given in table 2.4.3-1.

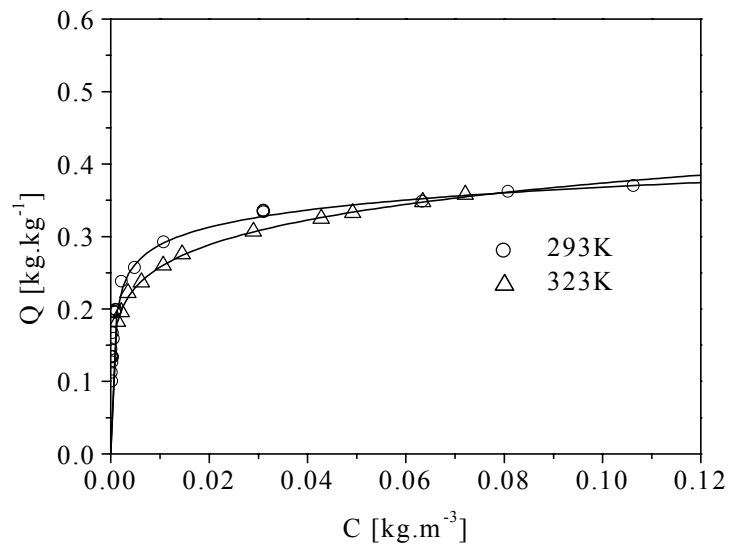


**Fig. 2.4.3-4a** Sorption isotherms of p-nitroaniline on AC RWB1. The lines are the Radke-Prausnitz fits. Its parameters are given in table 2.4.3-1.

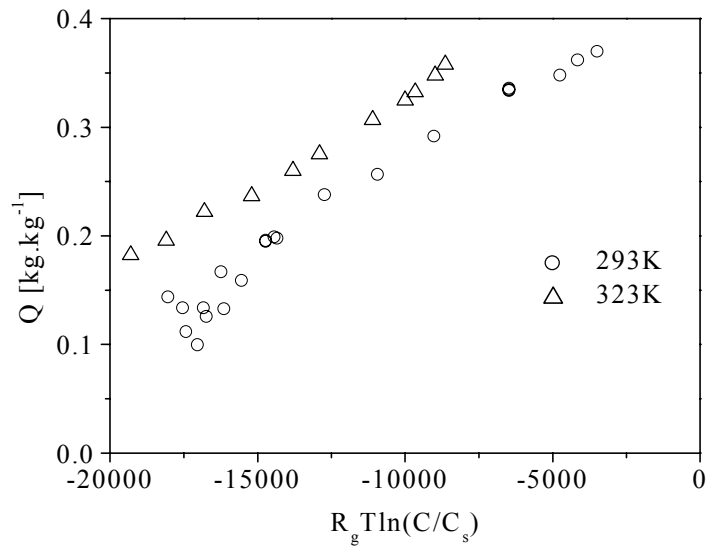


**Fig. 2.4.3-4b** Potential plot of sorption isotherms of p-nitroaniline on AC RWB1.

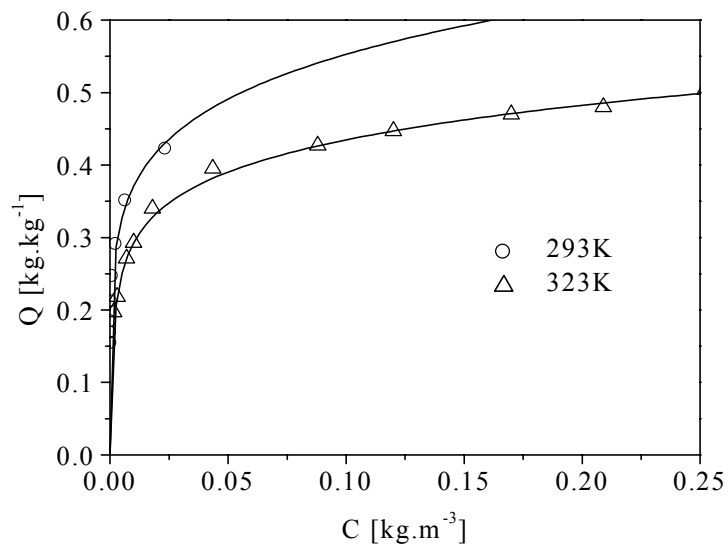


**Fig. 2.4.3-5a** Sorption isotherms of p-nitroaniline on AC R1-extra. The lines are the Radke-Prausnitz fits. Its parameters are given in table 2.4.3-1.

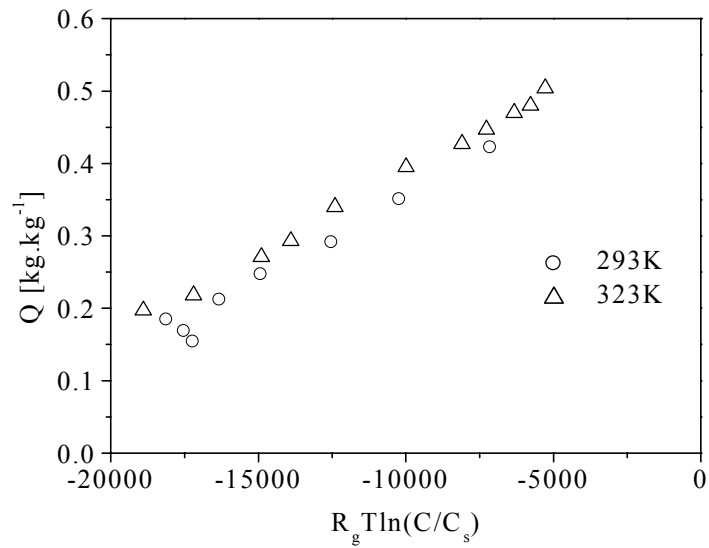


**Fig. 2.4.3-5b** Potential plot of sorption isotherms of p-nitroaniline on AC R1-extra.

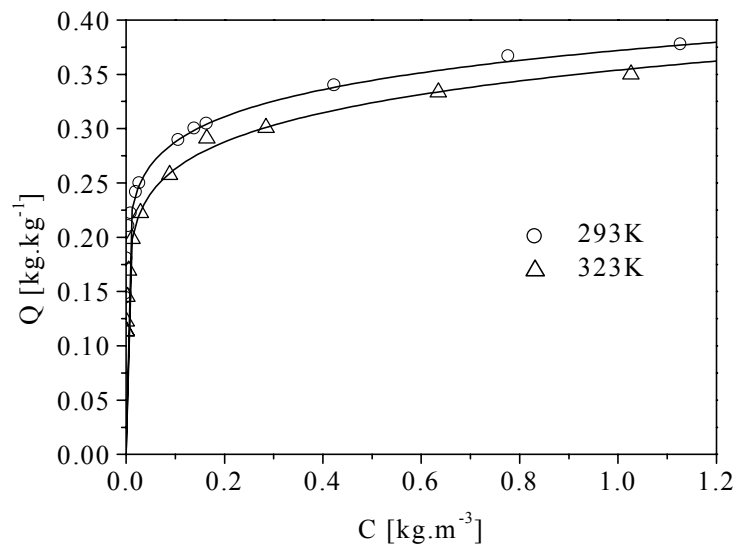
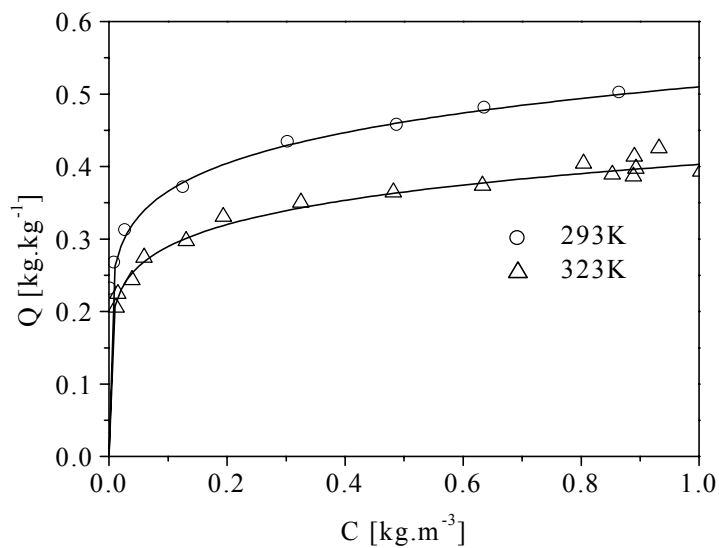


**Fig. 2.4.3-6** Sorption isotherms of quinoxaline on AC RWB1. The lines are the Radke-Prausnitz fits. Its parameters are given in table 2.4.3-1.



**ig. 2.4.3-7** Sorption isotherms of quinoxaline on AC R1-extra. The lines are the Radke-Prausnitz fits. Its parameters are given in table 2.4.3-1.

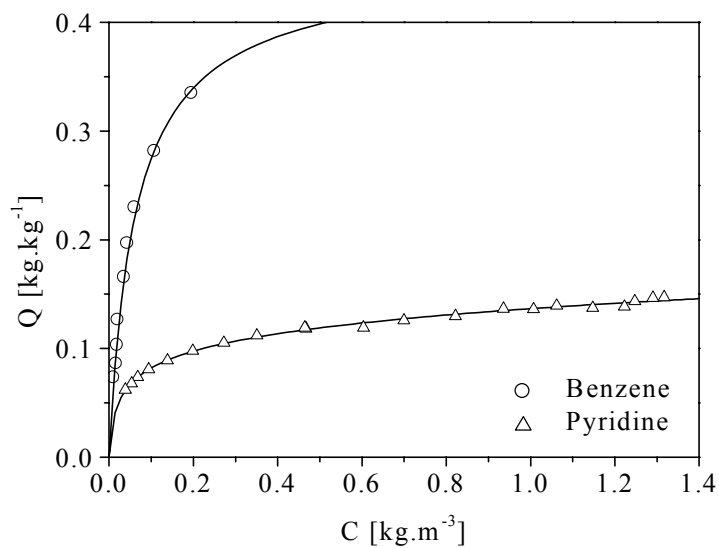


**Fig.2.4.3-8** Sorption isotherms of benzene and pyridine on AC RWB1 at 293K. The lines are the Radke-Prausnitz fits. Its parameters are given in table 2.4.3-1.

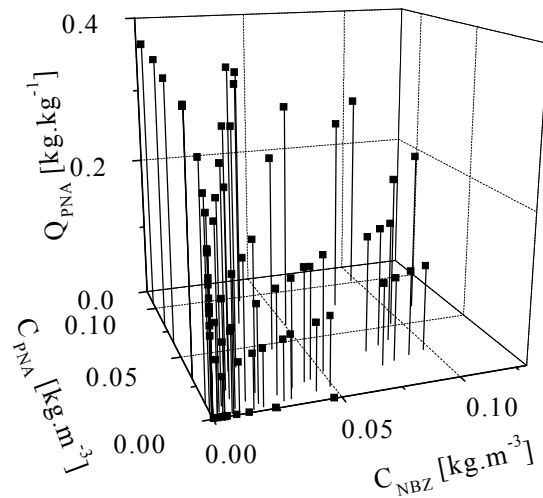


**Fig. 2.4.3-9a** Sorption isotherm of PNA on AC RWB1 at 293K as a function of NBZ and PNA solute concentration. (Data complemented with data from Kouyoumdiev [1992]).

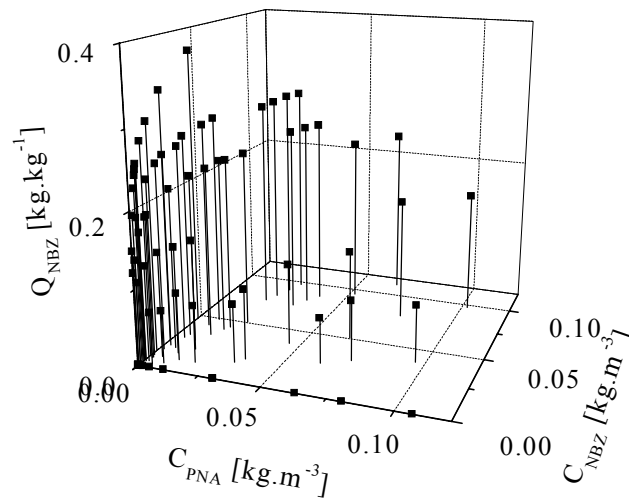


**Fig. 2.4.3-9b** Sorption isotherm of NBZ on AC RWB1 at 293K as a function of NBZ and PNA solute concentration. (Data complemented with data from Kouyoumdiev [1992]).

## References

Do, Duong. D.; 'Adsorption analysis: equilibria and kinetics', London, Imperial College Press, 1998.

Gregg, S.J. and Sing, K.S.W.; 'Adsorption, surface area and porosity', 2<sup>nd</sup> ed., London, Academic Press, 1982.

Horvath, G. and Kawazoe, K.; 'Method for the calculation of effective poresize distribution in molecular sieve carbon', J. Chem. Eng. Japan 16, pp. 16, 1983.

Kouyoumdjiev, M.S. 'Kinetics of adsorption from liquid phase on activated carbon', PhD. Thesis, Eindhoven University of Technology, 1992.pp. 1-235.

Polanyi, M.; 'Theories of the adsorption of gases. A general survey and some additional remarks', Trans. Faraday Soc., 28, p. 316, 1932.

Radke, C.J. and Prausnitzs, J.M.; 'Adsorption of organic compounds from dilute aqueous solution on activated carbon', Ind. Eng. Chem. Fund., 11, p. 445, 1972.

Tamon, Hajime and Okazaki, Morio; 'Desorption characteristics of aromatic compounds in aqueous solution on solid adsorbents', J. Colloid Interface Sci. 179, pp. 181-187, 1996.

## Symbols

### Greek symbols:

$\varepsilon$	J.mole <sup>-1</sup>	adsorption potential
$\sigma$	nm	Lennard-Jones diameter
$\sigma_1$	nm	Lennard-Jones diameter of adsorbent atom
$\sigma_2$	nm	Lennard-Jones diameter of adsorbate atom

### Latin symbols:

$A1, A2, N_1, N_2$		parameters Horvath Kawazoe model
$C$	kg.m <sup>-3</sup>	adsorbate concentration
$C_s$	kg.m <sup>-3</sup>	solubility
$D_{a,w}$	m <sup>2</sup> .s <sup>-1</sup>	bulk diffusivity of the adsorbate
$F_{RP}, K_{RP}, N_{RP}$		Radke-Prausnitz fit parameters
$n$	mole.kg <sup>-1</sup>	amount of adsorbate per kg carbon
$N_{AV}$	-	Avogadro number
$P$	Pa	vapour pressure
$P_0$	Pa	saturated vapour pressure
$Q$	kg <sub>adsorbate</sub> .kg <sub>c</sub> <sup>-1</sup>	amount of adsorbate per kg carbon
$R_g$	J.mole <sup>-1</sup> .K <sup>-1</sup>	gas constant
$T$	K	absolute temperature
$V_m$	m <sup>3</sup> .mole <sup>-1</sup>	molar volume
$W$	m <sup>3</sup> kg <sub>c</sub> <sup>-1</sup>	adsorbed volume

### 3. Adsorption equilibria with density functional theory

#### 3.1. Introduction

In order to understand transport phenomena in heterogeneous porous materials, it is necessary to gain insight in the equilibrium behaviour in a single pore. It has been known that fluids in narrow pores show a rich variety of phase transitions [Lastoskie et.al., 1993]. It has also been known for a long time that the confinement leads to a shift of the bulk coexistence curve. This is called capillary phase separation, when liquid-phase adsorption is considered, or capillary condensation, considering vapour-phase adsorption. The past two decades statistical mechanics calculations made clear that in the micro-pores, with a diameter of a few molecular sizes, pore filling mechanisms like film-layer formation and continuous pore filling play an important role. In addition, freezing and melting behaviour of confined fluids may deviate strongly from bulk behaviour [Sliwinska-Bartkowiak et.al., 1999].

The numerical models of adsorption may be separated into three general categories. Firstly the molecular dynamic (MD) simulations in which the forces between discrete molecules are calculated to follow their individual time-dependent movements. Secondly, Monte Carlo (MC) methods replace the lengthy process of time integration with trial-and-error minimisation of the free energy followed by ensemble averaging. Both the MD and MC simulations need the definition of discrete molecules that makes the simulations bound to a limited number of molecules in the calculations, because of computing time and memory limitations. In contrast to MD and MC simulations, density functional theory (DFT) uses a mean field approximation for the molecule-molecule forces so that the system is not limited to a certain number of molecules. DFT accurately reproduces the results of MD and MC simulations with greatly reduced computational effort.

Several versions of density functional theory have been reported in the literature. All DFT's use similar physical concepts. Generally, it is assumed that the inter-molecular interaction can be divided into a short-range repulsive part, which determines the structure of the fluid, and a long-range attractive part. The main difference between the different versions of DFT is the treatment of the short-range repulsive part, which is approached with a hard sphere fluid. For highly inhomogeneous confined fluids, the local density is smoothed (non-local density approximation). The weighting function for smoothing the local density is chosen to give a good description of the hard sphere direct pair correlation function for the uniform fluid over a wide range of densities.

Here the Kierlik-Rosinberg DFT [Kierlik and Rosinberg, 1991] is used to gain insight in adsorption equilibria because it is applicable to multi-component fluids, in contrast to the often-used Tarazona model [Tarazona, 1985]. It is numerically simple compared to other DFT's like the Meister-Kroll-Groot theory [Meister and Kroll, 1985; Groot, 1987] or the Curtin-Ashcroft theory

[Curtin and Ashcroft, 1989], because the weighting functions are density independent. Finally, this theory also seems to be one of the most adequate ones to describe adsorption of fluids at solid surfaces. [Kierlik & Rosinberg, 1991, Kozak & Sokolowski, 1991].

In the next section, the theory is treated for general pore geometry and simple Lennard-Jones molecules. Next, the theory is worked out further for slit-like pore geometry. In section 3.3 the calculations come up for discussion. In section 3.3.1 it is explained how physical insight in the pore filling mechanisms is used to find a numerical solution to the theory. The subsequent section discusses simulations of nitrogen adsorption onto activated carbon. A comparison is made with the experimental results of section 2.3.2. In section 3.3.3 the results of some multi-component adsorption calculations are discussed.

## 3.2. The Kierlik-Rosinberg DFT

### 3.2.1 The grand potential energy functional

The fluid density distribution in an area of uniform temperature,  $T$ , and chemical potential,  $\mu_i = \mu_{\infty,i}$ , is determined by minimising the grand potential energy functional [Kierlik and Rosinberg, 1990]

$$\Omega[\{\rho_i\}] = F[\{\rho_i\}] + \sum_{i=1}^n \int d\mathbf{r} [v_i(\mathbf{r}) - \mu_i] \rho_i(\mathbf{r}) \quad (3.2.1-1)$$

in which  $v_i(\mathbf{r})$  [J] is the external potential and  $\rho_i(\mathbf{r})$  [m<sup>-3</sup>] the number density of a component  $i$  at position  $\mathbf{r}$ .

The intrinsic Helmholtz free energy functional  $F[\{\rho_i\}]$  describes the contribution of the molecule-molecule interactions, which are modelled with a Lennard-Jones potential.

$$u_{LJ,i,j}(r) = 4\epsilon_{i,j} \left[ \left( \frac{\sigma_{i,j}}{r} \right)^{12} - \left( \frac{\sigma_{i,j}}{r} \right)^6 \right] \quad (3.2.1-2)$$

$\sigma_{i,j}$  [m] is the Lennard-Jones size parameter,  $\epsilon_{i,j}$  [J] is the energy parameter.

The attractive part of the Lennard-Jones potential is defined according to the Weeks-Chandler-Andersen approximation [Weeks et.al.,1971] with a correction for the potential at cut-off radius  $r_c$ , beyond which the intermolecular interactions are neglected. The repulsive part of the Lennard-Jones potential is approximated with the potential of an inhomogeneous hard sphere mixture. Thus,  $F$  is separated into an attractive term ( $F_a$ ) and a repulsive term ( $F_r$ )

$$F = F_r + F_a \quad (3.2.1-3)$$

$F_a$  is modelled in a mean field approximation as

$$F_a[\{\rho_i\}] = \frac{1}{2} \sum_{i=1}^n \sum_{j=1}^n \int \int d\mathbf{r} d\mathbf{r}' \rho_i(\mathbf{r}) \rho_j(\mathbf{r}') u_{i,j}(|\mathbf{r} - \mathbf{r}'|) \quad (3.2.1-4)$$

in which  $n$  is the number of components.  $u_{i,j}$  [J] is the fluid-fluid potential for molecules  $i$  and  $j$ . According to the Weeks-Chandler-Andersen approximation

$$u_{i,j}(r) = u_{LJ,i,j}(r_m) - u_{LJ,i,j}(r_c) = -\varepsilon_{i,j} - u_{LJ,i,j}(r_c) \quad \text{for } r \leq r_m \quad (3.2.1-5)$$

$$u_{i,j}(r) = u_{LJ,i,j}(r) - u_{LJ,i,j}(r_c) \quad \text{for } r_m < r \leq r_c \quad (3.2.1-6)$$

$$u_{i,j}(r) = 0 \quad \text{for } r > r_c \quad (3.2.1-7)$$

$$r_m = 2^{1/6} \sigma_{i,j} \quad (3.2.1-8)$$

is the radius at which the derivative of the Lennard-Jones potential equals zero. The repulsive forces between the molecules are approximated with a hard-sphere potential:

$$u_{hs}(r) = \infty \quad \text{for } r \leq d_{hs}$$

$$u_{hs}(r) = 0 \quad \text{for } r > d_{hs}$$

The hard sphere diameter  $d_{hs}$  is approximated with the Barker-Henderson equation [Barker & Henderson, 1967]

$$d_{hs,i} = \int_0^{\infty} \left[ 1 - \exp\left(\frac{-u_{i,i}^R(r)}{k_B T}\right) \right] dr \quad (3.2.1-9)$$

where

$$u_{i,i}^R(r) = u_{LJ,i,i}(r) - u_{LJ,i,i}(r_m) - u_{LJ,i,i}(r_c) \quad \text{for } r < r_m \quad (3.2.1-10)$$

$$u_{i,i}^R(r) = 0 \quad \text{for } r > r_m \quad (3.2.1-11)$$

According to Kierlik and Rosinberg the following approximation is used for the Helmholtz free energy functional of a hard sphere mixture [Kierlik & Rosinberg, 1990, 1992].  $F_r$  is split up into an ideal gas term  $F_{r,id}$  and an excess part  $F_{r,ex}$ .

$$F_r = F_{r,id} + F_{r,ex} \quad (3.2.1-12)$$

$$F_{r,id}[\{\rho_i\}] = k_B T \sum_{i=1}^n \int d\mathbf{r} \rho_i(\mathbf{r}) [\ln(\Lambda_i^3 \rho_i(\mathbf{r})) - 1] \quad (3.2.1-13)$$

in which  $\Lambda_i$  is the deBroglie wavelength [m], given by [Davis, 1996, p.101]

$$\Lambda_i = h_p (2\pi m_i k_B T)^{-1/2} \quad (3.2.1-14)$$

Here  $h_p$  is Planck's constant [Js] and  $m_i$  is the molecular mass of component  $i$  [kg].

The excess part of the free energy functional for a hard sphere mixture is given by

$$F_{r,ex}[\{\rho_i\}] = k_B T \int d\mathbf{r} \Phi_{PY}[n_0(\mathbf{r}), n_1(\mathbf{r}), n_2(\mathbf{r}), n_3(\mathbf{r})] \quad (3.2.1-15)$$

The free energy density,  $\Phi_{PY}$ , is taken from the Percus-Yevick compressibility equation of state for a uniform hard-sphere mixture.

$$\Phi_{PY} = -n_0 \ln(1 - n_3) + n_1 n_2 / (1 - n_3) + (1 / 24\pi) n_2^3 / (1 - n_3)^2 \quad (3.2.1-16)$$

The smoothed density  $n_\alpha$  is calculated from

$$n_\alpha(\mathbf{r}) = \sum_{i=1}^n n_{\alpha,i}(\mathbf{r}) = \sum_{i=1}^n \int \rho_i(\mathbf{r}') \omega_{\alpha,i}(|\mathbf{r} - \mathbf{r}'|) d\mathbf{r}' \quad (3.2.1-17)$$

where  $\omega_k(r)$  are four independent weight functions wherein  $R_{hs,i}$  is the hard sphere radius of component  $i$ :

$$\omega_{0,i}(r) = -\frac{1}{8\pi} \delta''(R_{hs,i} - r) + \frac{1}{2\pi r} \delta'(R_{hs,i} - r) \quad (3.2.1-18)$$

$$\omega_{1,i}(r) = -\frac{1}{8\pi} \delta'(R_{hs,i} - r) \quad (3.2.1-19)$$

$$\omega_{2,i}(r) = \delta(R_{hs,i} - r) \quad (3.2.1-20)$$

$$\omega_{3,i}(r) = \Theta(R_{hs,i} - r) \quad (3.2.1-21)$$

Here  $\Theta(r)$  is the Heaviside function,  $\delta(r)$  is the Dirac delta function and the primes denote successive derivatives of the delta function.

### 3.2.2. Minimisation of the grand potential energy functional

The equilibrium density profile was found by minimising the grand potential energy functional, which means solving

$$\frac{\delta\Omega[\{\rho_i\}]}{\delta\rho_j(\mathbf{r})} = 0 \quad (3.2.2-1)$$

simultaneously for all components  $j$  over the total volume area  $r$ .

All parameters were made dimensionless according to

length	[m]:	$r^* = r/\sigma_{1,1}$
volume	[m <sup>3</sup> ]	$\rho^* = \rho \cdot \sigma_{1,1}^{-3}$
energy	[J]:	$\mu^* = \mu/\varepsilon_{1,1}$
pressure	[Pa]:	$P^* = P \cdot \sigma_{1,1}^3/\varepsilon_{1,1}$
density	[m <sup>-3</sup> ]:	$\rho^* = \rho \cdot \sigma_{1,1}^3$
$\Lambda$	[m]:	$\Lambda^* = \Lambda/\sigma_{1,1}$
$k_B T$	[J]:	$T^* = k_B T/\varepsilon_{1,1}$

In the following (sections 3.2.2, 3.2.3 and 3.2.4), the asterisks are left out for the dimensionless parameters. All parameters, used in this section, are dimensionless.

According to the rules for functional derivation [Davis, 1996, p.429]

$$\int \frac{\delta\Omega[\{\rho_i\}]}{\delta\rho_j(\mathbf{r})} y(\mathbf{r}) d\mathbf{r} = \left( \frac{d\Omega[\{\rho_i; \rho_j(\mathbf{r}) + \varepsilon y(\mathbf{r})\}]}{d\varepsilon} \right)_{\varepsilon=0} \quad (3.2.2-2)$$

for an arbitrary function  $y(r)$ . Here the object  $\delta\Omega[\{\rho_i\}]/\delta\rho_j(r)$  depends on  $\rho_j$  and  $r$  but not on  $\varepsilon$  or  $y(r)$ .

The grand potential is split up in different parts that each are differentiated.

$$\frac{\delta\Omega[\{\rho_i\}]}{\delta\rho_j(\mathbf{r})} = \frac{\delta \left( F_{r,id} + F_{r,ex} + F_a + \sum_{i=1}^n \int v_i(\mathbf{r}) \rho_i(\mathbf{r}) d\mathbf{r} - \sum_{i=1}^n \int \mu_i \rho_i(\mathbf{r}) d\mathbf{r} \right)}{\delta\rho_j(\mathbf{r})} \quad (3.2.2-3)$$

Firstly, the differentiation of the part describing the influence of the external potential is considered, using equations (3.2.1-1) and (3.2.2-2)

$$\left[ \frac{d \left( \sum_{i=1, i \neq j}^n \int v_i(\mathbf{r}) \rho_i(\mathbf{r}) d\mathbf{r} + \int v_j(\mathbf{r}) [\rho_j(\mathbf{r}) + \varepsilon y(\mathbf{r})] d\mathbf{r} \right)}{d\varepsilon} \right]_{\varepsilon=0} = \int v_j(\mathbf{r}) y(\mathbf{r}) d\mathbf{r} \quad (3.2.2-4)$$

and thus

$$\frac{\delta \left( \sum_{i=1}^n \int v_i(\mathbf{r}) \rho_i(\mathbf{r}) d\mathbf{r} \right)}{\delta \rho_j(\mathbf{r})} = v_j(\mathbf{r}) \quad (3.2.2-5)$$

A similar solution is found for differentiation of the chemical potential term.

$$\frac{\delta \left( \sum_{i=1}^n \int \mu_i \rho_i(\mathbf{r}) d\mathbf{r} \right)}{\delta \rho_j(\mathbf{r})} = \mu_j(\mathbf{r}) \quad (3.2.2-6)$$

The ideal gas contribution is found from equation (3.2.1-13) as follows.

$$\left( \frac{dF_{r,id} [\{\rho_i; \rho_j + \varepsilon y\}]}{d\varepsilon} \right)_{\varepsilon=0} = \left( \frac{d \left( T \int d\mathbf{r} (\rho_j(\mathbf{r}) + \varepsilon y(\mathbf{r})) [\ln(\Lambda_j^3 (\rho_j(\mathbf{r}) + \varepsilon y(\mathbf{r}))) - 1] \right)}{d\varepsilon} \right)_{\varepsilon=0} \quad (3.2.2-7)$$

$$= \left( T \int y(\mathbf{r}) [\ln(\Lambda_j^3 (\rho_j(\mathbf{r}) + \varepsilon y(\mathbf{r}))) - 1] d\mathbf{r} + T \int (\rho_j(\mathbf{r}) + \varepsilon y(\mathbf{r})) \frac{\Lambda_j^3 y(\mathbf{r})}{\Lambda_j^3 (\rho_j(\mathbf{r}) + \varepsilon y(\mathbf{r}))} d\mathbf{r} \right)_{\varepsilon=0} \quad (3.2.2-8)$$

$$= T \int y(\mathbf{r}) \ln[\Lambda_j^3 \rho_j(\mathbf{r})] d\mathbf{r} \quad (3.2.2-9)$$

Thus as the final solution for the ideal gas contribution is found

$$\left( \frac{dF_{r,id} [\{\rho_i; \rho_j + \varepsilon y(\mathbf{r})\}]}{d\varepsilon} \right)_{\varepsilon=0} = T \int y(\mathbf{r}) \ln[\Lambda_j^3 \rho_j(\mathbf{r})] d\mathbf{r} \quad (3.2.2-10)$$

and

$$\frac{\delta F_{r,id} [\{\rho_i\}]}{\delta \rho_j(\mathbf{r})} = T \ln[\Lambda_j^3 \rho_j(\mathbf{r})] \quad (3.2.2-11)$$

The derivative of the excess part of the hard sphere contribution is found by solving

$$\frac{\delta F_{r,ex}[\{\rho_i\}]}{\delta \rho_j(\mathbf{r})} = T \frac{\delta \int d\mathbf{r} \Phi_{PY}[n_0(\mathbf{r}), n_1(\mathbf{r}), n_2(\mathbf{r}), n_3(\mathbf{r})]}{\delta \rho_j(\mathbf{r})} \quad (3.2.2-12)$$

The common chain rules for the derivatives of functions are used for differentiation of functionals too. Thus for (3.2.2-12) it is found from (3.2.1-16) that

$$\frac{\delta F_{r,ex}[\{\rho_i\}]}{\delta \rho_j(\mathbf{r})} = T \int \left( \begin{array}{l} -n'_{0,j} \ln(1-n_3) + \frac{n_0 n'_{3,j}}{1-n_3} \\ + \frac{n'_{1,j} n_2 + n_1 n'_{2,j}}{1-n_3} + \frac{n_1 n_2 n'_{3,j}}{(1-n_3)^2} \\ + \frac{3n_2^2 n'_{2,j}}{24\pi(1-n_3)^2} + \frac{2n_2^3 n'_{3,j}}{24\pi(1-n_3)^3} \end{array} \right) d\mathbf{r} \quad (3.2.2-13)$$

With the differentiation rule for functionals,

$$n'_{\alpha,j} = \frac{\delta n_\alpha[\{\rho_i\}]}{\delta \rho_j(\mathbf{r})} = \omega_{\alpha,j} \quad (3.2.2-14)$$

Finally, the derivative of the molecular attraction part of the grand potential functional needs to be determined:

$$\left( \frac{dF_a[\{\rho_i; \rho_j + \varepsilon y\}]}{d\varepsilon} \right)_{\varepsilon=0} = \left[ \begin{array}{l} \frac{1}{2} \sum_{\substack{k=1 \\ k \neq j}}^n \iint d\mathbf{r} d\mathbf{r}' (\rho_j(\mathbf{r}) + \varepsilon y(\mathbf{r})) \rho_k(\mathbf{r}') u_{j,k}(|\mathbf{r} - \mathbf{r}'|) \\ \hline d\varepsilon \\ + \frac{1}{2} \sum_{\substack{i=1 \\ i \neq j}}^n \iint d\mathbf{r} d\mathbf{r}' (\rho_j(\mathbf{r}') + \varepsilon y(\mathbf{r}')) \rho_i(\mathbf{r}) u_{i,j}(|\mathbf{r} - \mathbf{r}'|) \\ \hline d\varepsilon \\ + \frac{1}{2} \iint d\mathbf{r} d\mathbf{r}' (\rho_j(\mathbf{r}') + \varepsilon y(\mathbf{r}')) (\rho_j(\mathbf{r}) + \varepsilon y(\mathbf{r})) u_{j,j}(|\mathbf{r} - \mathbf{r}'|) \\ \hline d\varepsilon \end{array} \right]_{\varepsilon=0} \quad (3.2.2-15)$$

$$\begin{aligned}
& \left[ \frac{1}{2} \sum_{\substack{k=1 \\ k \neq j}}^n \int \int d\mathbf{r} d\mathbf{r}' y(\mathbf{r}) \rho_k(\mathbf{r}') u_{j,k}(|\mathbf{r} - \mathbf{r}'|) \right. \\
& = \left. + \frac{1}{2} \sum_{\substack{i=1 \\ i \neq j}}^n \int \int d\mathbf{r} d\mathbf{r}' y(\mathbf{r}') \rho_i(\mathbf{r}) u_{i,j}(|\mathbf{r} - \mathbf{r}'|) \right. \\
& \left. + \frac{1}{2} \int \int d\mathbf{r} d\mathbf{r}' (\rho_j(\mathbf{r}') y(\mathbf{r}) + \rho_j(\mathbf{r}) y(\mathbf{r}')) u_{j,j}(|\mathbf{r} - \mathbf{r}'|) \right] \quad (3.2.2-16)
\end{aligned}$$

$$\begin{aligned}
& = \left[ \frac{1}{2} \sum_{i=1}^n \int \int d\mathbf{r} d\mathbf{r}' y_j(\mathbf{r}) \rho_i(\mathbf{r}') u_{i,j}(|\mathbf{r} - \mathbf{r}'|) \right. \\
& \left. + \frac{1}{2} \sum_{i=1}^n \int \int d\mathbf{r} d\mathbf{r}' y_j(\mathbf{r}') \rho_i(\mathbf{r}) u_{i,j}(|\mathbf{r} - \mathbf{r}'|) \right] \quad (3.2.2-17)
\end{aligned}$$

Both integrations should be carried out over the total volume area. Thus,

$$\left( \frac{dF_a[\{\rho_i; \rho_j + \varepsilon y\}]}{d\varepsilon} \right)_{\varepsilon=0} = \sum_{i=1}^n \int \int d\mathbf{r} d\mathbf{r}' y_j(\mathbf{r}) \rho_i(\mathbf{r}') u_{i,j}(|\mathbf{r} - \mathbf{r}'|) \quad (3.2.2-18)$$

Together with equation 3.2.2-2, it follows from equation 3.2.2-18 that

$$\frac{\delta F_a[\{\rho_i\}]}{\delta \rho_j(\mathbf{r})} = \sum_{i=1}^n \int d\mathbf{r}' \rho_i(\mathbf{r}') u_{i,j}(|\mathbf{r} - \mathbf{r}'|) \quad (3.2.2-19)$$

Substitution of all found derivatives in equation 3.2.2-3 gives

$$\begin{aligned}
& T \ln[\Lambda_j^3 \rho_j(\mathbf{r})] + \frac{\delta F_{r,ex}[\{\rho_i\}]}{\delta \rho_j(\mathbf{r})} \\
& + \sum_{i=1}^n \int \rho_i(\mathbf{r}') u_{i,j}(|\mathbf{r} - \mathbf{r}'|) d\mathbf{r}' + v_j(\mathbf{r}) = \mu_j \quad (3.2.2-20)
\end{aligned}$$

The second term on the left-hand side is worked out further in section 3.2.4 for the geometry of an infinite slit pore.

### 3.2.3. Bulk

#### 3.2.3.1. The bulk chemical potential

Equation 3.2.2-20 is used to calculate the chemical potential of component  $j$  in the bulk ( $\mu_{\infty,j}$ ) when the bulk densities of all components are known. The external potential equals zero and the bulk is assumed to have a homogeneous density. Then, from equation 3.2.2-20 follows that

$$T \ln[\Lambda_j^3 \rho_{\infty,j}] + \frac{\delta F_{r,ex} \{\rho_{\infty,j}\}}{\delta \rho_{\infty,j}} + 4\pi \sum_{i=1}^n \rho_{\infty,i} \int u_{i,j}(r) r^2 dr = \mu_{\infty,j} \quad (3.2.3-1)$$

The smoothed densities, used in the calculation of  $\Phi_{PY}$  according to equations 3.2.1-18 to 3.2.1-21, are simplified to [Kierlik & Rosinberg, 1991, 1992], which makes it easy to calculate the second term in equation 3.2.1-1.

$$n_{0,\infty} = \sum_{i=1}^n \rho_{\infty,i} \quad (3.2.3-2)$$

$$n_{1,\infty} = \sum_{i=1}^n R_{hs,i} \rho_{\infty,i} \quad (3.2.3-3)$$

$$n_{2,\infty} = \sum_{i=1}^n 4\pi R_{hs,i}^2 \rho_{\infty,i} \quad (3.2.3-4)$$

$$n_{3,\infty} = \sum_{i=1}^n \frac{4}{3} \pi R_{hs,i}^3 \rho_{\infty,i} \quad (3.2.3-5)$$

### 3.2.3.2. The bulk pressure

The bulk pressure,  $P$ , is calculated with [Groot, 1987]

$$P = -\left(\frac{\partial F}{\partial V}\right)_{N,T} = -\left(\frac{\partial F_a}{\partial V}\right)_{N,T} - \left(\frac{\partial F_{r,id}}{\partial V}\right)_{N,T} - \left(\frac{\partial F_{r,ex}}{\partial V}\right)_{N,T} \quad (3.2.3-6)$$

in which  $V$  [m<sup>3</sup>] is the systems volume, and  $N$  is the number of particles.

$$\left(\frac{\partial F}{\partial V}\right)_{N,T} = \left(\frac{\partial F}{\partial V}\right)_{\rho V,T} \quad (3.2.3-7)$$

$$\rho = \sum_{i=1}^n \rho_i \quad (3.2.3-8)$$

$$\partial(\rho V) = \rho \partial V + V \partial \rho \quad (3.2.3-9)$$

$$\partial V|_{\rho V} = \frac{\partial(\rho V) - V \partial \rho}{\rho} \Big|_{\rho V} = \frac{-V \partial \rho}{\rho} \quad (3.2.3-10)$$

$$\left(\frac{\partial F}{\partial V}\right)_{N,T} = \rho \left(\frac{\partial F}{V \partial \rho}\right)_{\rho V,T} = \rho^2 \left(\frac{\partial(F / \rho V)}{\partial \rho}\right)_{\rho V,T} \quad (3.2.3-11)$$

$x_i$  is the mole fraction of component  $i$ .

$$\rho_i = x_i \rho \quad (3.2.3-12)$$

$x_i$  remains constant while the number of particles  $N$  remains constant.

From equations 3.2.1-4 and 3.2.3-11 and 3.2.3-12 follows

$$\begin{aligned} \left( \frac{\partial F_a}{\partial V} \right)_{N,T} &= \frac{1}{2} \rho^2 \sum_{i=1}^n \sum_{j=1}^n x_{\infty,i} x_{\infty,j} \int u_{i,j}(|\mathbf{r}|) d\mathbf{r} \\ &= 2\pi\rho^2 \sum_{i=1}^n \sum_{j=1}^n x_{\infty,i} x_{\infty,j} \int u_{i,j}(r) r^2 dr \end{aligned} \quad (3.2.3-13)$$

From equation 3.2.1-13 follows

$$\left( \frac{\partial F_{r,id}}{\partial V} \right)_{N,T} = k_B T \rho \quad (3.2.3-14)$$

From equation 3.2.1-15 follows

$$\left( \frac{\partial F_{r,ex}}{\partial V} \right)_{N,T} = k_B T \rho^2 \left( \frac{\Phi'_{PY}}{\rho} - \frac{\Phi_{PY}}{\rho^2} \right) \quad (3.2.3-15)$$

### 3.2.3.3. Bulk phase separation, gas-liquid and liquid-liquid phase equilibria

At phase coexistence, the chemical potentials  $\mu_i$  in the phases  $\alpha$  and  $\beta$  are equal for all components  $i$ :

$$\mu_{\alpha,i} = \mu_{\beta,i} \quad (3.2.3-16)$$

The phase rule says:

$$\text{degrees of freedom} = \text{number of components} - \text{number of phases} + 2.$$

When the liquid-vapour equilibrium for one pure component at fixed temperature is calculated, there are two phases. Thus, there are no degrees of freedom left. There are two unknowns, namely the liquid and the vapour density. Thus, to solve the problem, equation 3.2.3-16 is used, together with the equation that says that the pressure in the liquid phase must equal that in the vapour phase:

$$P_\alpha = P_\beta \quad (3.2.3-17)$$

If the liquid-liquid equilibrium, for two components at fixed temperature, is calculated, there are two phases and there is one degree of freedom left. In this case, the pressure is fixed too. There are four unknowns. Equation 3.2.3-16 is used for both,  $i=1$  and  $i=2$ , together with:

$$P_\alpha = P_\beta = P_{fixed} \quad (3.2.3-18)$$

Another way to calculate the liquid-liquid equilibrium is to use the vapour pressure of the liquid as the total system pressure. This means that there are 3 phases and thus that there is no degree of freedom left when temperature is fixed.

There are six unknowns, namely the densities of each of the two components in the three phases. The six equations that are used to solve the problem are

$$\mu_{\alpha,i} = \mu_{\beta,i} = \mu_{\gamma,i} \quad (3.2.3-19)$$

for both,  $i=1$  and  $i=2$ , and

$$P_\alpha = P_\beta = P_\gamma. \quad (3.2.3-20)$$

**3.2.4. Adsorption of a Lennard-Jones fluid in a slit pore**  
 Consider the slit pore as illustrated in figure 3.2.4-1.

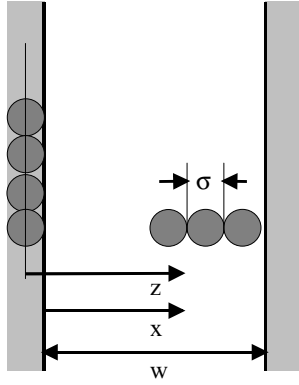


**Fig. 3.2.4-1** Schematic representation of a slit-pore with pore-width  $w$ , and molecular diameter  $\sigma$ .

Also consider a function  $f_x$ , which is only a function of the direction  $x$ , perpendicular to the pore wall and a function  $f_r$ , only a function of the distance from point  $\mathbf{r}$ . Then the integration

$$F(\mathbf{r}) = \int_0^{|\mathbf{r}-\mathbf{r}'|=R} f_x(\mathbf{r}') f_r(|\mathbf{r}-\mathbf{r}'|) d\mathbf{r}' \quad (3.2.4-1)$$

can be written as

$$F(x) = 2\pi \int_{-R}^R f_x(x+x_1) \int_{|x_1|}^R f_r(r) r dr dx_1 \quad (3.2.4-2)$$

Substituting  $f_r = \omega_\alpha$  for the weight functions it can be derived from

$$F_\alpha(x) = 2\pi \int_{-R}^R f_x(x+x_1) \int_{|x_1|}^R \omega_\alpha(r) r dr dx_1 \quad (3.2.4-3)$$

that [Kierlik & Rosinberg, 1990]

$$F_0(x) = \sum_{i=1}^n \left( \begin{array}{l} \frac{1}{2} [f_x(x+R_{hs,i}) + f_x(x-R_{hs,i})] \\ -\frac{R_{hs,i}}{4} [f_x'(x+R_{hs,i}) - f_x'(x-R_{hs,i})] \end{array} \right) \quad (3.2.4-4)$$

$$F_1(x) = \sum_{i=1}^n \left( \begin{array}{l} \frac{1}{4} \int_{-R_{hs,i}}^{R_{hs,i}} f_x(x+x_1) dx_1 \\ -\frac{R_{hs,i}}{4} [f_x(x+R_{hs,i}) + f_x(x-R_{hs,i})] \end{array} \right) \quad (3.2.4-5)$$

$$F_2(x) = \sum_{i=1}^n \left( 2\pi R_{hs,i} \int_{x-R_{hs,i}}^{x+R_{hs,i}} f_x(x_1) dx_1 \right) \quad (3.2.4-6)$$

And thus for the smoothed densities it is found that

$$n_0(x) = \sum_{i=1}^n \left( \begin{array}{l} \frac{1}{2} [\rho_i(x+R_{hs,i}) + \rho_i(x-R_{hs,i})] \\ -\frac{R_{hs,i}}{4} [\rho_i'(x+R_{hs,i}) - \rho_i'(x-R_{hs,i})] \end{array} \right) \quad (3.2.4-7)$$

$$n_1(x) = \sum_{i=1}^n \left( \begin{array}{l} \frac{1}{4} \int_{-R_{hs,i}}^{R_{hs,i}} \rho_i(x+x_1) dx_1 \\ -\left(\frac{R_{hs,i}}{4}\right) [\rho_i(x+R_{hs,i}) + \rho_i(x-R_{hs,i})] \end{array} \right) \quad (3.2.4-8)$$

$$n_2(x) = \sum_{i=1}^n \left( 2\pi R_{hs,i} \int_{x-R_{hs,i}}^{x+R_{hs,i}} \rho_i(x_1) dx_1 \right) \quad (3.2.4-9)$$

$$n_3(x) = \sum_{i=1}^n \left( \pi \int_{-R_{hs,i}}^{R_{hs,i}} \rho_i(x-x_1) [(R_{hs,i})^2 - (x_1)^2] dx_1 \right) \quad (3.2.4-10)$$

Then, for the derivative of the excess hard sphere contribution to the local density,

$$\frac{\delta F_{r,ex}(\rho_j(\mathbf{r}))}{\delta \rho_j(\mathbf{r})} = T \int \left( \begin{array}{l} -n'_{0,j} \ln(1-n_3) + \frac{n_0 n'_{3,j}}{1-n_3} + \frac{n'_1 n_{2,j} + n_{1,j} n'_{2,j}}{1-n_3} \\ + \frac{n_1 n_2 n'_{3,j}}{(1-n_3)^2} + \frac{3n_2^2 n'_{2,j}}{24\pi(1-n_3)^2} + \frac{2n_2^3 n'_{3,j}}{24\pi(1-n_3)^3} \end{array} \right) dr \quad (3.2.4-11)$$

the following result is obtained:

$$\frac{\delta F_{r,ex}(\rho_i(\mathbf{r}))}{\delta \rho_i(\mathbf{r})} = T \left[ \begin{aligned}
& - \left( \frac{1}{2} [\ln[1 - n_3(x + R_{hs,i})] + \ln[1 - n_3(x - R_{hs,i})]] \right. \\
& \left. - \frac{R_{hs,i}}{4} [(\ln[1 - n_3(x + R_{hs,i})])' - (\ln[1 - n_3(x - R_{hs,i})])'] \right) \\
& + \left( \pi \int_{-R_{hs,i}}^{R_{hs,i}} \frac{n_0(x - x_1)}{1 - n_3(x - x_1)} [(R_{hs,i})^2 - (x_1)^2] dx_1 \right) \\
& + \left( \frac{1}{4} \int_{-R_{hs,i}}^{R_{hs,i}} \frac{n_2(x + x_1)}{1 - n_3(x + x_1)} dx_1 \right. \\
& \left. - \left( \frac{R_{hs,i}}{4} \left[ \frac{n_2(x + R_{hs,i})}{1 - n_3(x + R_{hs,i})} + \frac{n_2(x - R_{hs,i})}{1 - n_3(x - R_{hs,i})} \right] \right) \right) \\
& + \left( 2\pi R_{hs,i} \int_{x-R_{hs,i}}^{x+R_{hs,i}} \frac{n_1(x_1)}{1 - n_3(x_1)} \rho_i(x_1) dx_1 \right) \\
& + \left( \pi \int_{-R_{hs,i}}^{R_{hs,i}} \frac{n_1(x - x_1)n_2(x - x_1)}{[1 - n_3(x - x_1)]^2} [(R_{hs,i})^2 - (x_1)^2] dx_1 \right) \\
& + \left( \frac{1}{4} R_{hs,i} \int_{x-R_{hs,i}}^{x+R_{hs,i}} \frac{[n_2(x_1)]^2}{[1 - n_3(x_1)]^2} \rho_i(x_1) dx_1 \right) \\
& + \left( \frac{1}{12} \int_{-R_{hs,i}}^{R_{hs,i}} \frac{[n_2(x - x_1)]^3}{[1 - n_3(x - x_1)]^3} [(R_{hs,i})^2 - (x_1)^2] dx_1 \right)
\end{aligned} \right] \tag{3.2.4-12}$$

The external potential is the pore wall potential, calculated with Steele's formula [Steele, 1973], which describes the interaction between the solid pore wall and the fluid component  $i$ . The solid density  $\rho_w$  is assumed to be uniform over planar sheets of atoms spaced  $\Delta$  apart .

$$u_{w,i}(z) = 2\pi\rho_w \varepsilon_{w,i} \sigma_{w,i}^2 \Delta \left[ \frac{2}{5} \left( \frac{\sigma_{w,i}}{z} \right)^{10} - \left( \frac{\sigma_{w,i}}{z} \right)^4 - \frac{\sigma_{w,i}^4}{3\Delta(z + 0.61\Delta)^3} \right] \quad (3.2.4-13)$$

where  $\varepsilon_{w,i}$  and  $\sigma_{w,i}$  are parameters for interactions between solid pore wall and component  $i$ .

The external potential becomes

$$v_i(x) = u_{w,i}(x) - u_{w,i}(w - x) \quad (3.2.4-14)$$

### 3.3. Calculations and pore filling mechanisms

#### 3.3.1. Introduction

In this section, some details are explained about the procedure which was followed to calculate complete isotherms. To be able to find some of the numerical solutions it was necessary to have some insight in the pore filling mechanisms that occur. Thus, for clarification, the calculation method and some of the calculation results are treated together in this section.

The input parameters of the calculations for a two component mixture are summarised below.

1. The desired pore widths,  $w$ .
2. The number of grid points per (smallest) molecular diameter,  $n_{grid}$ .
3. Lennard Jones potentials,  $\epsilon$ .
4. Lennard Jones diameters,  $\sigma$ .
5. The non-ideality parameters,  $k$ .
6. The Steele parameters (equation 3.2.4-13).
7. The cut off radius for Lennard-Jones potential,  $r_c$ .
8. The molar masses,  $m$ .
9. The system pressure,  $P$ .

The Lennard-Jones interaction parameters obeyed Lorentz-Berthelot rules. This means for the solid-fluid interactions:

$$\sigma_{w,i} = \frac{1}{2}(\sigma_{w,w} + \sigma_{i,i}) \quad (3.3.1-1)$$

$$\epsilon_{w,i} = k_{w,i} \sqrt{\epsilon_{w,w} \epsilon_{i,i}} \quad (3.3.1-2)$$

And for the fluid-fluid interactions:

$$\sigma_{i,j} = \frac{1}{2}(\sigma_{i,i} + \sigma_{j,j}) \quad (3.3.1-3)$$

$$\epsilon_{i,j} = k_{i,j} \sqrt{\epsilon_{i,i} \epsilon_{j,j}} \quad (3.3.1-4)$$

The deviation of the interaction parameter,  $k$ , from unity is a measure for the non-ideality of the mixture.

All integrations were carried out by the trapezoidal rule. The parameters used for the example calculations of the adsorption of a two component mixture, further on in this section, are given in table 3.3.1-1.

The first calculations that were performed are the phase diagrams of the vapour-liquid equilibria of the pure components. Next a miscibility phase diagram was calculated for the fluid mixture at the desired pressure. Also such a phase diagram was calculated for the fluid mixture under its own vapour pressure.

From those diagrams, an upper and lower temperature boundary was chosen for the pore equilibria calculations.

**Table 3.3.1-1** Parameters used for calculations in this section

Parameter	Value	Unit
$\Delta$	$0.335 \cdot 10^{-9}$	m
$\rho_w$	$0.114 \cdot 10^{30}$	$\text{m}^{-3}$
$\sigma_{1,1}$	$0.341 \cdot 10^{-9}$	m
$\sigma_{2,2}$	$0.341 \cdot 10^{-9}$	m
$\sigma_{w,w}$	$0.340 \cdot 10^{-9}$	m
$\varepsilon_{w,w}/k_B$	28.0	$\text{K}^{-1}$
$\varepsilon_{1,1}/k_B$	119.8	$\text{K}^{-1}$
$\varepsilon_{2,2}/k_B$	119.8	$\text{K}^{-1}$
$k_{1,2}$	0.8	-
$k_{w,1}^*$	1.2	-
$k_{w,2}^*$	1	-
$m_1$	$6.64 \cdot 10^{-26}$	kg
$m_2$	$6.64 \cdot 10^{-26}$	kg
$P^*$	0.1	-
$r_c$	2.5	-
$n_{grid}$	10	-

\*component 1 is the adsorbate, component 2 is the solvent.

### *Continuous filling*

The sorption isotherms were calculated, starting at high temperature. One of the components was chosen as adsorbate. The first pore density profile was calculated at high bulk concentration of the adsorbate. This means, at solubility, or in case of complete miscibility, at the pure adsorbate bulk density at the given pressure. The combination of the adsorbate bulk density and the average pore density of the adsorbate forms one isotherm point. The next calculation, the adsorbate concentration in the bulk was lowered and a new pore density profile was calculated. The previous profile was used as an estimate. This procedure was repeated until a given lower bound in the bulk adsorbate concentration was reached. Or otherwise, until the numerical routine, which solved the system of equations, did not converge anymore. If no convergence was reached, this usually meant that a better solution could be found from another starting point. This is why also calculations were performed starting at very low adsorbate concentration in the bulk. The calculated density profiles were then used for the estimation of points at higher bulk concentration. At high enough temperatures (above the critical bulk phase coexisting temperature (see figure 3.3-1)), the two isotherms that were calculated from the different starting bulk concentrations were the same. This, because there was no phase separation in the pore. This case is so-called continuous pore filling. A complete isotherm contained a by the user given number of points. Those points were distributed at approximately equidistant average adsorbate density inside the pore.

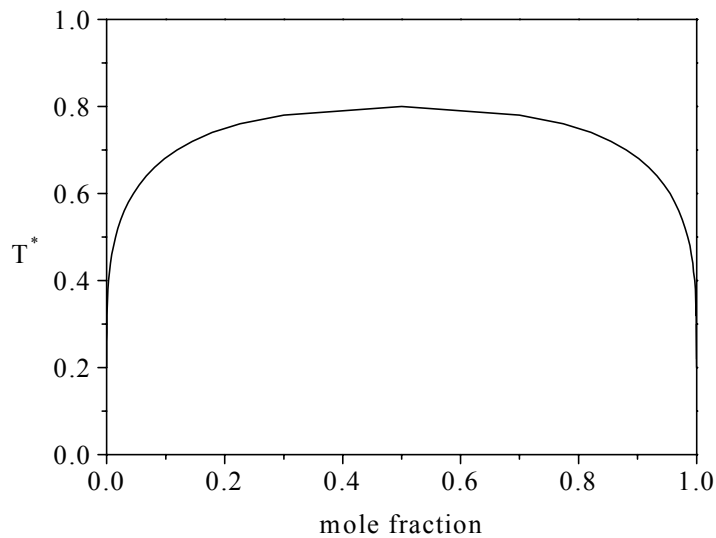


**Fig. 3.3-1.** Coexistence curve for a symmetric two component bulk mixture. The critical bulk phase coexistence temperature  $T^* = 0.79$  at  $P^* = 0.1$ .

#### *Pore phase separation*

At low temperatures, a phase separation could occur inside the pore. In those cases, two different isotherms were found from the different starting positions. At each isotherm point the grand potential,  $\Omega$ , was calculated. After interpolation of the isotherm points and the grand potential as a function of adsorbate bulk density, the most favourable isotherm was found. Namely, this is the isotherm having the lowest grand potential. In figure 3.3-2 an example is given of the calculated stable and meta-stable isotherm points. The average adsorbate densities in the pore are plotted, as well as the grand potential. In this example, a film layer separation was found before capillary phase separation took place. Finding the solutions corresponding to this film layer state demanded a special treatment described later in this section.

In figure 3.3-3, a sequence of isotherms is plotted for different temperatures. The isotherms belong to the same pore size as the isotherm in figure 3.3-2 ( $w^* = 4.26$ ). Figure 3.3-4 shows some characteristic pore density distributions, that belong to the calculation in figure 3.3-2 and the second isotherm from the right in figure 3.3-3 ( $T^* = 0.539$ ).

As was mentioned above, in the case of a film layer separation, the calculations need a special treatment.

At high temperature the isotherm is not discontinuous. A knee is found at the point where the adsorbate has formed a complete layer of molecules near the pore wall (figure 3.3-3). The isotherm point, where the average density in the middle of the pore had increased more in comparison with the previous point than the average density in the film layer, was memorised. This point served as an estimate for calculations at a third starting point, at lower temperature. It was

proven that this is a good way to find the solution for the film layer part of isotherms as in figure 3.3-2 (squares).

From high temperatures, evidence was found for stable multi-layer solutions at lower temperatures. This is shown in figures 3.3-5a and 3.3-5b. No attempt was made to calculate those solutions. In the literature, such stable multi-layer solutions are usually never mentioned or investigated.

After completion of the calculation of an isotherm, the temperature was lowered according to:

$$T_{new} = 0.95 * T_{old}$$

Not only the estimate for the third starting point was found from calculations at higher temperature. This also accounted for the starting points from high and low bulk densities.

After completion of the isotherms for one pore size, at all chosen temperatures, the calculation for the next pore size was started.

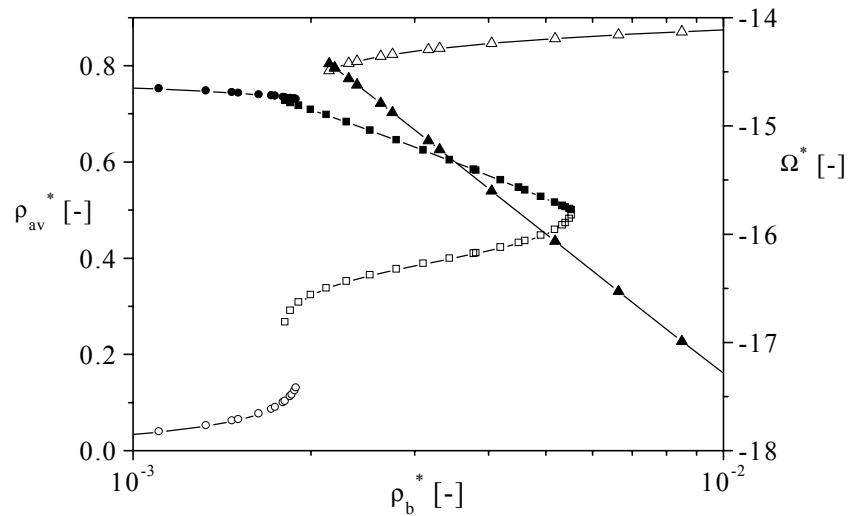


**Fig. 3.3-2** Left vertical axis (open symbols): sorption isotherm, stable and meta-stable points. Right vertical axis (closed symbols): corresponding grand potential. The circles indicate the solution from the starting point at low adsorbate concentration. The squares indicate the film layer solution. The triangles indicate the solution from starting point at high adsorbate concentration.  $w^* = 4.26$ ,  $T^* = 0.539$ .

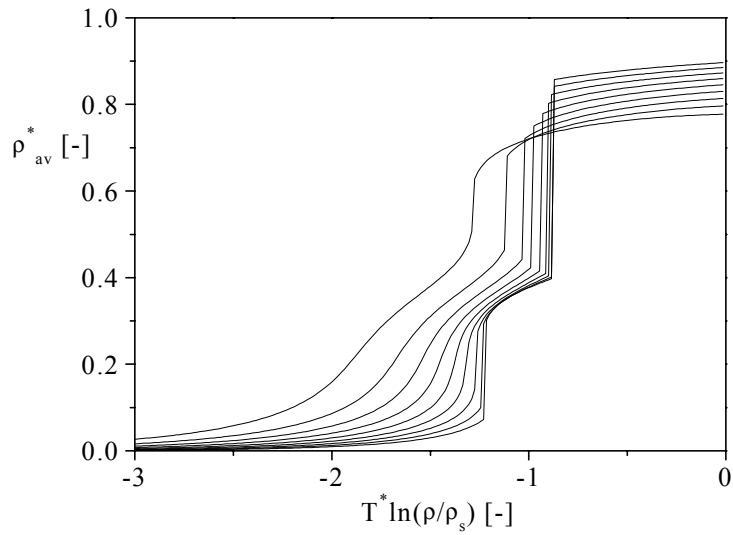


**Fig. 3.3-3** Isotherms from  $T^* = 0.77$  to  $T^* = 0.51$  (from left to right). Successive temperatures differ a factor 0.95.  $w^* = 4.26$ . The calculated isotherms with  $T^* > 0.79$  are not shown because in those cases the 2 components showed complete bulk miscibility (see figure 3.3-1).

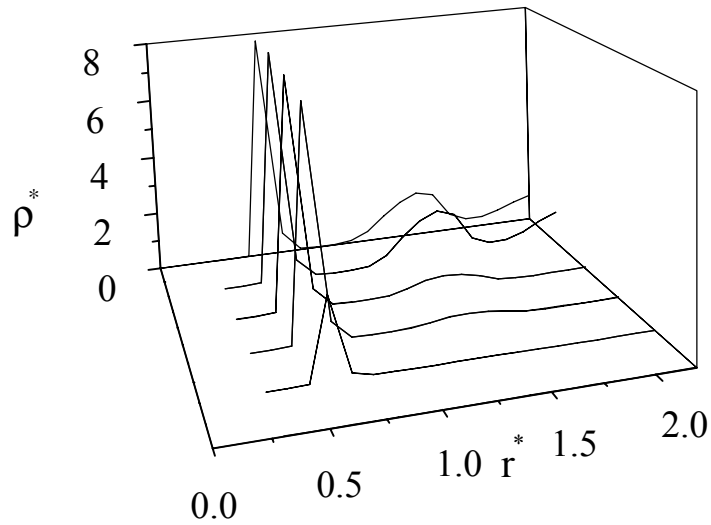


**Fig. 3.3-4** Pore density profiles for  $T^* = 0.539$ ,  $w^* = 4.26$ . Profiles from front to back are equilibria at adsorbate bulk densities  $\rho_b$ :

1. just below  $\rho_b$  at film layer transition
2. just above  $\rho_b$  at film layer transition
3. just below  $\rho_b$  at capillary phase separation
4. just above  $\rho_b$  at capillary phase separation
5.  $\rho_b = \text{solubility}$

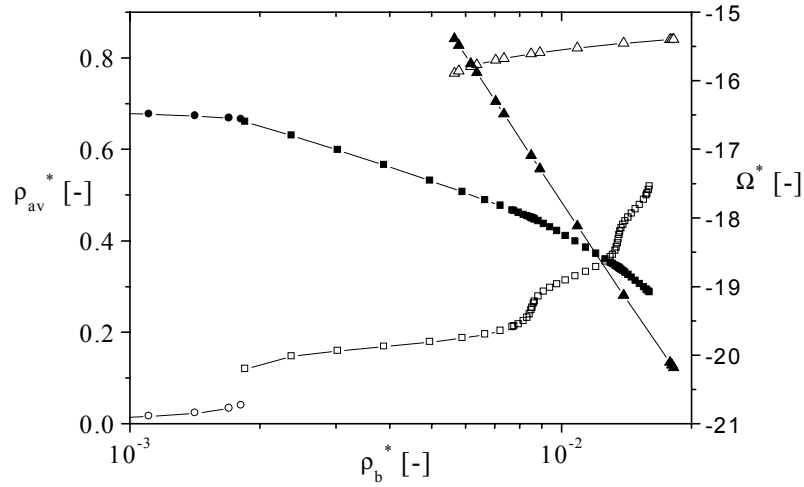


**Fig. 3.3-5a** Left vertical axis (open symbols): sorption isotherm, stable and metastable points. Right vertical axis (closed symbols): corresponding grand potential. The circles indicate the solution from the starting point at low adsorbate concentration. The squares indicate the film layer solution. The triangles indicate the solution from the starting point at high adsorbate concentration.  $w^*=10.49$ ,  $T^*=0.539$ .

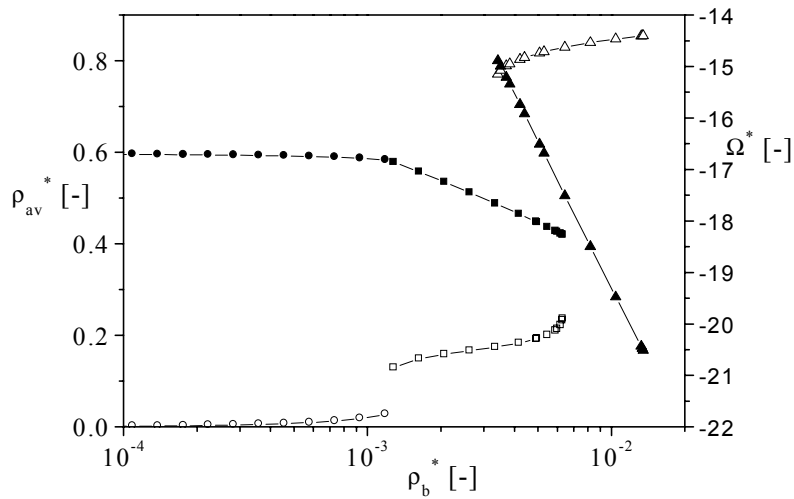


**Fig. 3.3-5b** Left vertical axis (open symbols): sorption isotherm, stable and metastable points. Right vertical axis (closed symbols): corresponding grand potential. The circles indicate the solution from the starting point at low adsorbate concentration. The squares indicate the film layer solution. The triangles indicate the solution from the starting point at high adsorbate concentration.  $w^*=10.49$ ,  $T^*=0.512$ .

### 3.3.2. Nitrogen adsorption in a carbon slit pore

#### 3.3.2.1. Introduction

Nitrogen sorption measurements are the most common method to characterise a micro-porous material with regard to surface area and pore size distribution. In this section, the Kierlik-Rosinberg density functional theory was used to calculate adsorption of nitrogen in a graphitic slit pore. The DFT data were compared to the sorption isotherms of activated carbons via a pore size distribution. The experimental data on those carbons were discussed in section 2.3.2.

In the table below, the DFT parameters that were used in the calculation, are listed.

**Table 3.3.2-1** Parameters used for calculation of nitrogen adsorption in a carbon slit pore.

Parameter	Value	Unit
$T$	77	K
$\Delta$	$0.335 \cdot 10^{-9}$	m
$\rho_w$	$0.114 \cdot 10^{30}$	$\text{m}^{-3}$
$\sigma_{l,l}$	$0.357 \cdot 10^{-9}$	m
$\sigma_{w,w}$	$0.340 \cdot 10^{-9}$	m
$\epsilon_{w,w}/k_B$	28.0	$\text{K}^{-1}$
$\epsilon_{l,l}/k_B^{(1)}$	93.98	$\text{K}^{-1}$
$\epsilon_{l,l}/k_B^{(2)}$	101.2	$\text{K}^{-1}$
$r_c$	7	-
$n_{grid}$	20	-

<sup>(1)</sup> value from Davis [1996, p. 221]

<sup>(2)</sup> value at optimised critical temperature

#### 3.3.2.2. Bulk properties

Experimental bulk properties and bulk properties of nitrogen, calculated with the DFT, are listed in table 3.3.2-2. The theory gave estimations of bulk properties like critical temperature and pressure at boiling points that deviated from experimental values for nitrogen. In some literature, the fluid-fluid Lennard-Jones potential of nitrogen was changed to correct for deviations from critical temperature [Kierlik et. al., 1995]. In this case it meant a shift of  $\epsilon_{l,l}/k_B = 93.98\text{K}$  to  $\epsilon_{l,l}/k_B = 101.2\text{K}$ . In table 3.3.2-2 it can be seen that this correction also gives better results for calculations of pressure and liquid bulk density at the boiling point at 77K.

A note must be made on the cut-off radius of the Lennard-Jones potential, because it was found to have a big influence on the calculated values of the critical temperature if it was taken too small. Taking the value of 7 molecular diameters for this parameter resulted in a deviation of less than 1% in the critical temperature in comparison with a Lennard-Jones potential without cut-off.

**Table 3.3.2-2** Experimental and with DFT calculated bulk properties of N<sub>2</sub>

Physical bulk parameter	Experimental value	DFT value $\epsilon_{ff}/k_B = 93.98\text{K}$	DFT value $\epsilon_{ff}/k_B = 101.2\text{K}$
$T_c$	126	117	126
$P_0 (T=77\text{K})$	$1.01 \times 10^5$	$1.55 \times 10^5$	$1.11 \times 10^5$
$\rho_l$	808	710	727
$\rho_l^*$	-	0.696	0.713
$T_c$	critical temperature		[K]
$P_0$	saturated vapour pressure		[Pa]
$\rho_l$	liquid density		[kg.m <sup>-3</sup> ]
$\rho_l^*$	dimensionless liquid density		[-]

### 3.3.2.3. Adsorption in an infinite slit pore

Figures 3.3.2-1a and b show the sorption isotherms, calculated with DFT for several pore sizes at 77K, with respectively  $\epsilon_{l,l}/k_B = 93.98\text{K}$  and  $\epsilon_{l,l}/k_B = 101.2\text{K}$ . The different nitrogen Lennard-Jones potentials, used in the calculations, cause a difference of only a few percent in the isothermal data, concerning the characteristic points like film layer formation in pores of about 3 molecular diameters and larger ( $R_g T \ln(P/P_0) \approx -6000 \text{ J.mole}^{-1}$ ) and capillary condensation ( $R_g T \ln(P/P_0) > -3500 \text{ J.mole}^{-1}$ ).

Another characteristic feature in figure 3.3.2-1a is the isotherm at  $w^* = 0.82$ . This pore is so narrow that repulsive forces from the pore walls prevent adsorption at as low bulk pressures as in the case of pores that are a little bit larger.

In chapter 2.3.2, it was mentioned that the hysteresis closure point in nitrogen sorption isotherms always closes at about  $P/P_0 = 0.45$ . Hysteresis is caused by different filling and emptying mechanisms for adsorption and desorption. Figure 3.3.2-2b shows a pore that is filled molecular layer by molecular layer, starting from figure 3.3.2-2a where only a mono-layer is present. Figure 3.3.2-2c shows a pore that is emptied by withdrawal of the capillary meniscus, only leaving the first mono-layer present. At the same amount of adsorbate inside the pore, the two filling mechanisms will have different energies. One of the mechanisms must be in a meta-stable situation. Thus when adsorption takes place by layer formation and desorption by capillary flow, which is often assumed [Gregg and Sing, 1982, p.126], hysteresis will occur. This will not happen when the pore is filled by a mechanism of continuous filling, because in that case there are no meta-stable situations (see section 3.3.1).

The hysteresis closure point in nitrogen isotherms does not seem to be very much dependent on the kind of porous material [Gregg and Sing, 1982, p.154]. From this it can be concluded that there is only one mechanism for the formation and deformation of the first molecular layer which undergoes a large influence of the pore wall. Thus the hysteresis loop must be caused by the capillary condensation step in pores of about three molecular diameters in width

and larger. Having a look at figure 3.3.2-1a and b, it follows that a hysteresis closure point may be expected at  $R_g T \ln(P/P_0) \approx -4000$  J/mol. And thus  $P/P_0 \approx 2 \cdot 10^{-3}$ . The capillary condensation step at  $P/P_0 \approx 0.45$  matches with a pore width of about 10 molecular diameters.

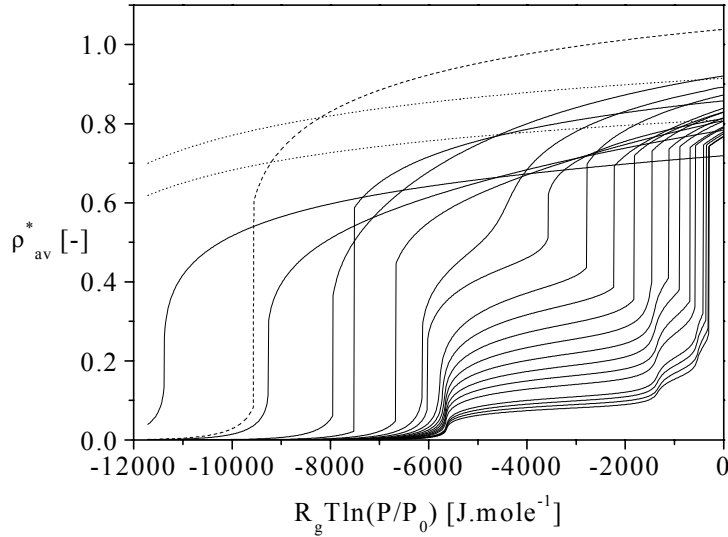


**Fig. 3.3.2-1a** Sorption isotherms of nitrogen at 77K calculated with DFT.

$\epsilon_{ff}/k_B = 93.98K$ .

Dashed line:  $w^* = 0.82$

Dots, resp. upper and lower isotherm:  $w^* = 0.95, 1.11$

Solid lines from left to right at  $\rho^*_{av} = 0.2$ :  $w^* = 1.28, 1.49, 1.73, 2.01, 2.34, 2.72, 3.16, 3.67, 4.26, 4.95, 5.75, 6.69, 7.77, 9.03, 10.49, 13.46, 14.88, 16.44, 18.2$

In the following section, the influence of the size of the slit surface on the adsorption isotherm will be discussed, in order to investigate the large difference between the experimental hysteresis closure point and the one that was theoretically derived from the DFT results above.

The DFT calculations were performed with the assumption of an infinite slit pore. In reality however, the slit-layers in activated carbon are built up of about 39 carbon atoms each [Tamon and Okazaki, 1996]. A derivation, analogue to the Kelvin equation is made to estimate the importance of the size of the slit surface.

Consider the following situation. Starting from figure 3.3.2-2a, an amount of adsorbate is moved from the bulk vapour phase to the pore and the situation of figure 3.3.2-2c is obtained. It is assumed that the adsorbed phase that's not in the first molecular layer has the same structure as pure bulk liquid adsorbate.

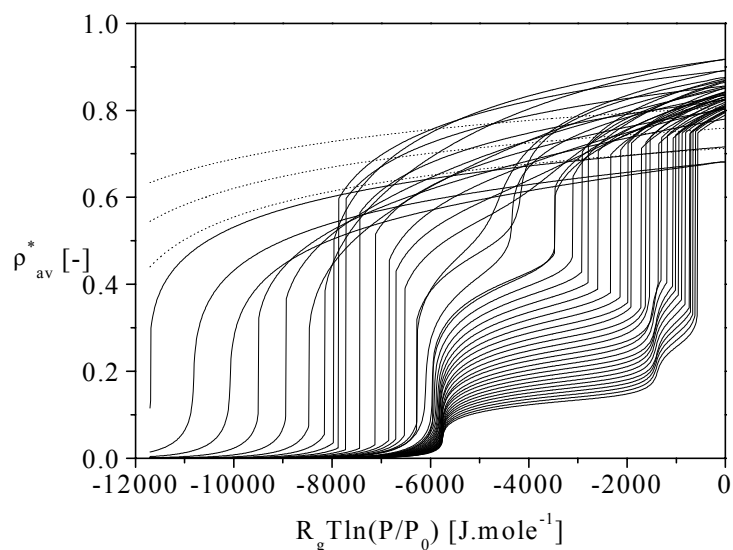


**Fig. 3.3.2-1b** Sorption isotherms of nitrogen at 77K calculated with DFT.

$$\varepsilon_{1,1}/k_B = 101.2\text{K.}$$

$$w^* = e^{0.1+0.05(n-1)}.$$

Dots, from upper to lower isotherm:  $n=1,2,3$

Solid lines from left to right at  $\rho_{av}^*=0.2$ :  $n=4..47$

$n=1$ :  $w^*=1.11$

$n=47$ :  $w^*=11.0$

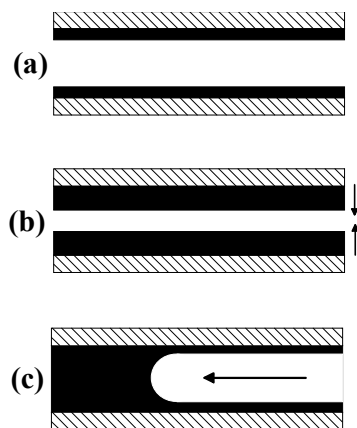


**Fig. 3.3.2-2** (a) Schematic representation of slit pore with one molecular layer adsorbed at each pore wall. (b) Schematic representation of slit pore with growing of multiple molecular layers at each pore wall due to adsorption. (c) Schematic representation of slit pore with withdrawing capillary meniscus due to desorption. The first molecular layer at the pore wall remains.

The curvature of the meniscus is neglected in calculating its surface. The pore wall is assumed to be a rectangular surface, resulting in four menisci. The amount of energy produced when moving the adsorbate from the bulk vapour phase to the pore is then calculated with

$$R_g T \ln\left(\frac{P}{P_0}\right) + \frac{-2A\sigma_{fg} + 2A\sigma_{lf} + 4w\sqrt{A}\sigma_{lg}}{Aw} V_m \quad (3.3.2-1)$$

in which  $A$  is the surface of one slit wall [ $\text{m}^2$ ],  $w$  is the slit width [ $\text{m}$ ],  $\sigma_{lf}$  is the surface tension between liquid adsorbate and the first molecular layer,  $\sigma_{lg}$  is the surface tension between liquid adsorbate,  $\sigma_{fg}$  is the surface tension between the first molecular layer and the gas phase,  $V_m$  is the molar volume of the adsorbate. The Young-Dupré equation [Gregg and Sing, 1982, p.123] is used to describe the relation between  $\sigma_{lf}$  and  $\sigma_{lg}$  via the contact angle of the capillary meniscus with the first molecular layer,  $\theta$ .

$$\sigma_{lf} = \sigma_{lg} \cos(\theta) + \sigma_{fg} \quad (3.3.2-2)$$

Because an equilibrium situation is considered, the energy for exchange of adsorbate between pore and bulk should equal zero. This results in

$$R_g T \ln\left(\frac{P}{P_0}\right) + 2\sigma_{lg} V_m \frac{A \cos(\theta) + 2w\sqrt{A}}{Aw} = 0 \quad (3.3.2-3)$$

which becomes the Kelvin equation for an infinite slit pore when  $A$  goes to infinity. The interpretation of the equation is that in equilibrium with a vapour phase at partial pressures higher than  $P/P_0$  a pore with diameter  $w$  and slit surface  $A$  will be filled with adsorbate.

Equation 3.3.2-3 can be transformed to

$$w = - \left( \frac{R_g T \ln\left(\frac{P}{P_0}\right)}{2\sigma_{lg} V_m} + \frac{2}{\sqrt{A}} \right)^{-1} \quad (3.3.2-4)$$

A graphitic layer of 39 carbon atoms like in activated carbon has a surface area of roughly  $A=7 \times 10^{-19} \text{ m}^2$ . The nitrogen surface tension  $\sigma_{lg}=0.00872 \text{ Nm}^{-1}$  and  $V_m=3.47 \times 10^{-5} \text{ m}^3 \text{ mole}^{-1}$ . Substituting this together with  $P/P_0=0.45$  in equation 3.3.2-4, under the assumption that  $\cos(\theta)=0$ , a negative value for the pore width  $w$  is obtained. However, at this partial pressure a large part of the pores will already be filled with adsorbate. The air/adsorbate surface will be small, compared to the adsorbate/film layer surface. Anyway, it becomes clear from the pore filling approach that resulted in equation 3.3.2-4 that the finiteness of the pores means that they may be filled at much higher partial vapour pressures than infinite pores. It also does not seem to be completely accurate to consider one pore alone, without its surrounding neighbourhood of other pores in the material. Those effects will probably be larger in large pores than in small

pores. In pores of only a few molecular diameters in width the interaction with the wall or the first molecular layer will play a more important role than interactions at the edges of a pore.

#### 3.3.2.4. The use of DFT data to calculate pore size distributions from sorption isotherms of the carbons used in this study

Because the nitrogen bulk properties with  $\varepsilon_{1,1}/k_B=101.2\text{K}$  agree better with experimental data than in case of the use of  $\varepsilon_{1,1}/k_B=93.98\text{K}$ , the DFT data of figure 3.3.2-1b were used in combination with a (bimodal) log-normal pore size distribution (PSD) to model the nitrogen adsorption isotherms of section 2.3.2. The average pore density was determined as a function of pore width and  $R_g T \ln(P/P_0)$  by fitting a bi-cubic spline through the data of figure 3.3.2-1b. This way it was possible to calculate an overall isotherm in combination with a pore size distribution. The coefficients of the log-normal PSD were calculated by fitting the isotherm from the DFT data to the experimental data by minimisation of the sum of squares.

The bimodal log-normal distribution function is given by

$$f(w^*) = \exp\left(-0.5 \left[ \frac{\ln\left(\frac{w^*}{a_1}\right)}{a_2} \right]^2\right) + a_3 \exp\left(-0.5 \left[ \frac{\ln\left(\frac{w^*}{a_4}\right)}{a_5} \right]^2\right) \quad (3.3.2-5)$$

Here,  $f$  is the volume frequency of the pore size, and  $a_1$  to  $a_5$  are the fitting parameters. It was only necessary to use a bimodal distribution, to obtain a satisfactory fit, in the case of the adsorption isotherm of AC R1-extra. For the AC RWB1 and AC AP4-60 the coefficient  $a_3$  was set equal to zero. In figure 3.3.2-3a,b,c the isotherms calculated from the DFT data are compared to the experimental isotherms for the three types of activated carbon. Figure 3.3.2-4 shows the corresponding pore size distributions. In table 3.3.2-3 the fitting coefficients are listed.

**Table 3.3.2-3** Coefficients of the (bimodal) log-normal pore size distributions for activated carbons, calculated from DFT data.

	$a_1$	$a_2$	$a_3$	$a_4$	$a_5$
AC AP4-60	0.869	-0.428	0	-	-
AC R1-extra	-0.977	1.48	1.59	-0.470	0.0113
AC RWB1	-3.348	0.598	0	-	-

Figure 3.3.2-5 shows the pore size distributions that were calculated from the nitrogen adsorption experiments with the Horvath Kawazoe method in section 2.3.2. This method estimates smaller pore sizes than the DFT. Especially for AC AP4-60, the difference between the two methods is large.

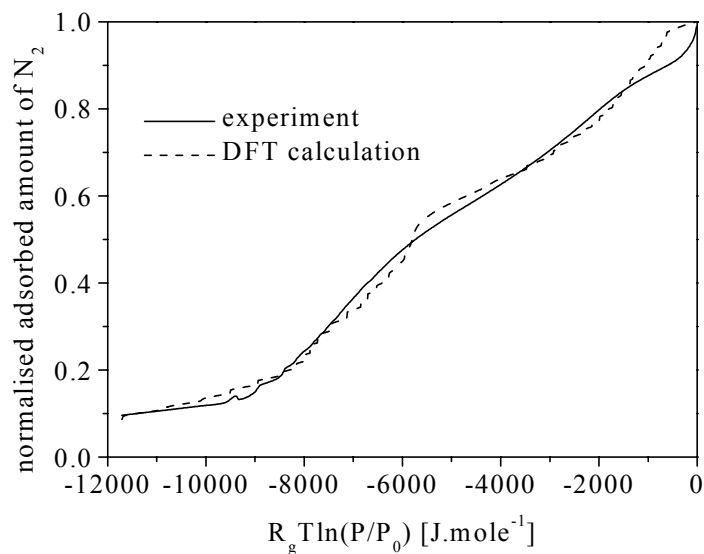


**Fig. 3.3.2-3a** Experimental nitrogen isotherm at AC RWB1 and isotherm from DFT data, fitted to experimental isotherm with log-normal pore size distribution.

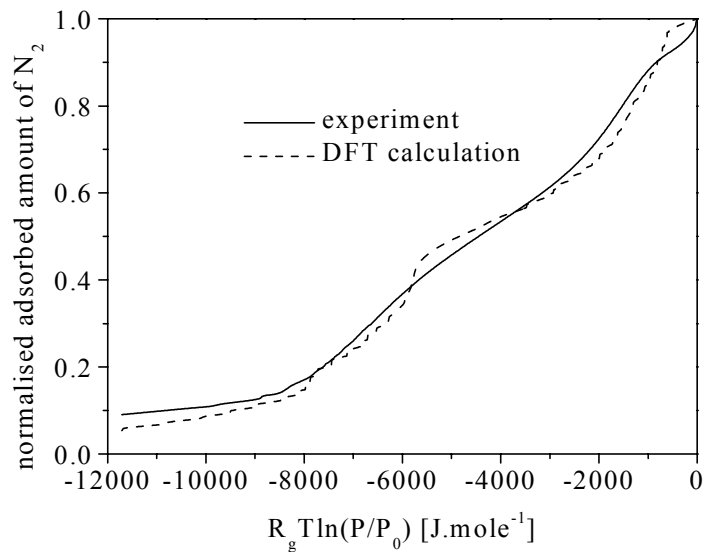


**Fig. 3.3.2-3b** Experimental nitrogen isotherm at AC R1-extra and isotherm from DFT data, fitted to experimental isotherm with a bimodal log-normal pore size distribution.

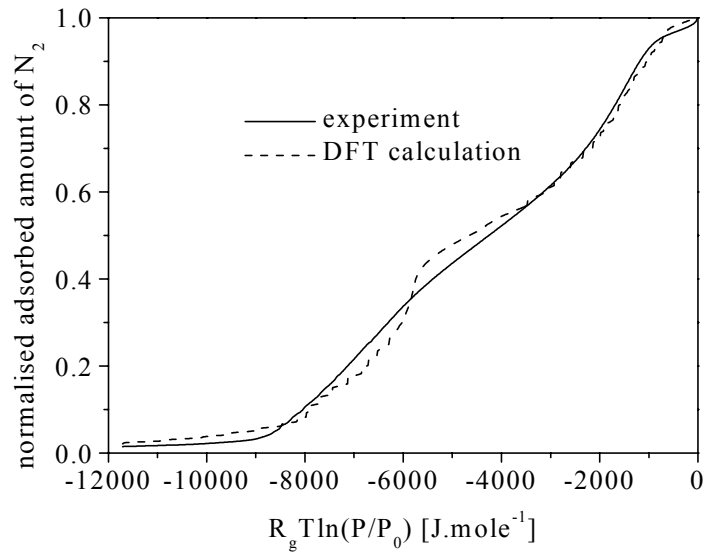


**Fig. 3.3.2-3c** Experimental nitrogen isotherm at AC AP4-60 and isotherm from DFT data, fitted to experimental isotherm with log-normal pore size distribution.

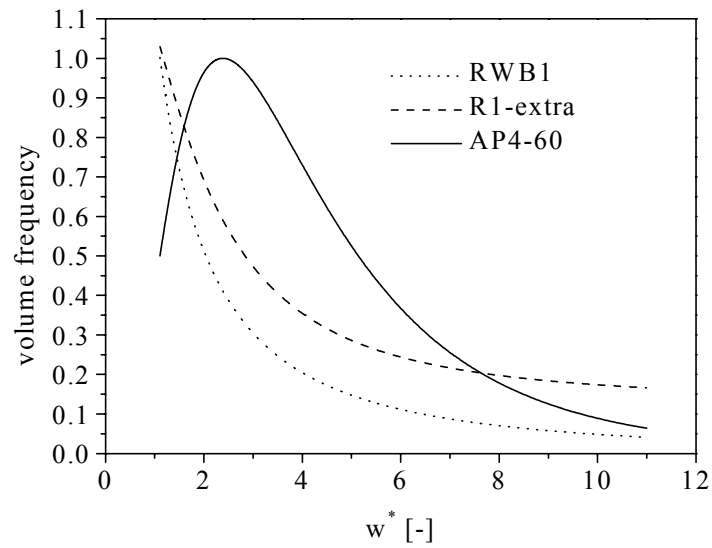


**Fig. 3.3.2-4** Pore size distributions used to calculate the nitrogen adsorption isotherms of figures 3.3.2-3a,b,c.

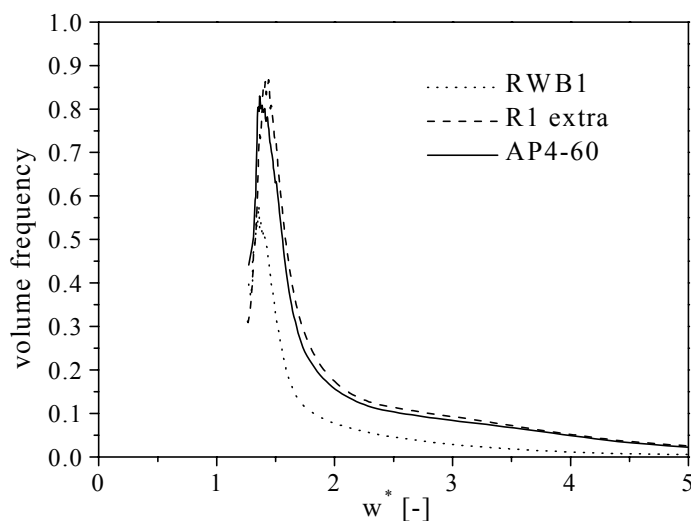


**Fig. 3.3.2-5** Pore size distributions, calculated with the Horvath Kawazoe method from the  $N_2$  sorption isotherm at 77K. (Derived from figure 2.3.2-2, under the assumption that the molar volume of  $N_2$  inside the pores is constant)

The prediction of the pore size may have important consequences in understanding the kinetics of adsorption since the pores are only a few molecular diameters in width and the molecular motion in the first molecular layer near the pore wall differs greatly from the kinetics of molecules that are further away from the pore wall [Bouyermaouen, 2001].

Having a look at the isotherms, calculated from DFT data, in figures 3.3.2-3a,b,c, the curves can be separated in several parts. The first part is where  $R_g T \ln(P/P_0) < -7000 \text{ J.mole}^{-1}$ . In this area pores smaller than 2 molecular diameters in width are being filled. Between  $R_g T \ln(P/P_0) = -7000 \text{ J.mole}^{-1}$  and  $R_g T \ln(P/P_0) = -5000 \text{ J.mole}^{-1}$ , the increase in adsorbate is mainly located in the first molecular layer in pores of three or more molecular sizes in diameter. This filling mechanism results in a steep part in the sorption isotherm. From  $R_g T \ln(P/P_0) > -4000 \text{ J.mole}^{-1}$  another steep part in the isotherm occurs due to filling of the space between the two first molecular layers in pores of three or more molecular sizes in diameter.

Although not as clear in the calculated isotherms, these steps are also found in the experimental data. The activated carbons are more heterogeneous of nature than the model, which is actually a bundle of parallel infinite slit pores. This heterogeneity of the real porous material may cause the smoothing of more or less sharp details compared to the calculated isotherms.

In the additional figures 3.3.2-6a,b,c the amounts adsorbed are separated in the amount adsorbed in the first molecular layer, near the pore wall, and the amount adsorbed in the middle of the pore.

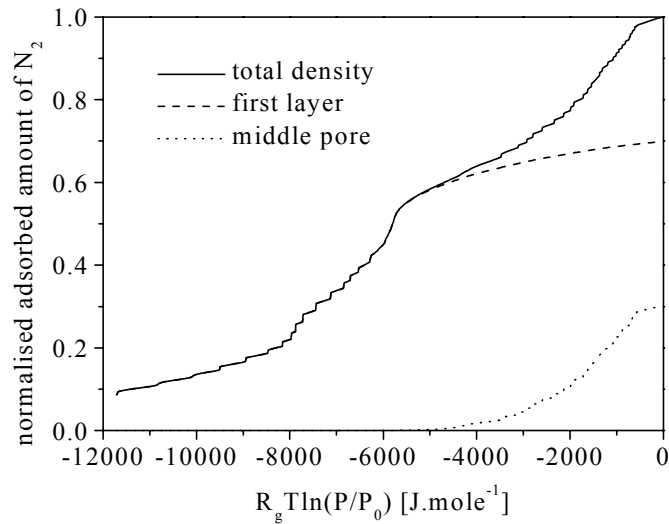


**Fig. 3.3.2-6a** Total isotherm (total density) AC RWB1, separated in part of adsorbate that is located in first molecular layer near pore wall (first layer) and adsorbate that is located in middle of pore, at least one molecular layer away from both pore walls (middle pore). Data from DFT calculations as in figure 3.3.2-3a.

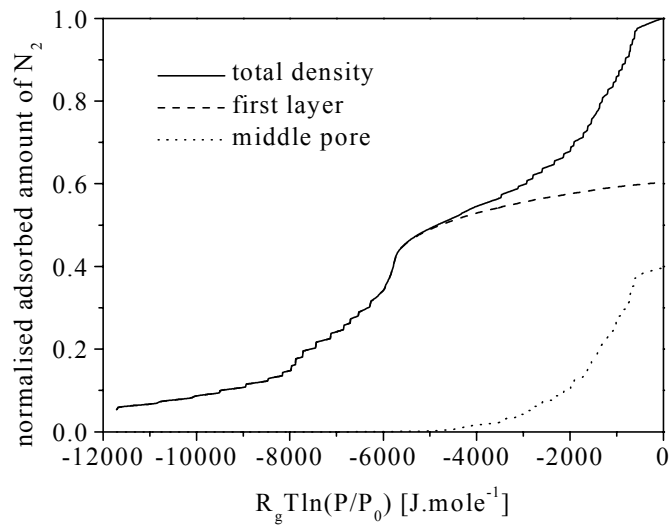


**Fig. 3.3.2-6b** Total isotherm (total density) of AC R1-extra, separated in part of adsorbate that is located in first molecular layer near pore wall (first layer) and adsorbate that is located in middle of pore, at least one molecular layer away from both pore walls (middle pore). Data from DFT calculations as in figure 3.3.2-3b.

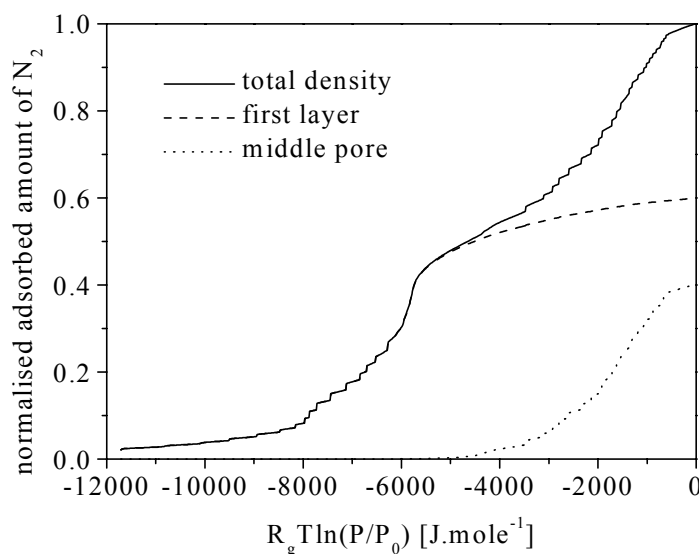


**Fig. 3.3.2-6c** Total isotherm (total density) of AC AP4-60, separated in part of adsorbate that is located in first molecular layer near pore wall (first layer) and adsorbate that is located in middle of pore, at least one molecular layer away from both pore walls (middle pore). Data from DFT calculations as in figure 3.3.2-3c.

### 3.3.3. Multi-component adsorption in a carbon slit pore

#### 3.3.3.1. Results

In this section, the results of a study of the adsorption characteristics of several two-component mixtures in a carbon slit pore are presented. The aim of the study was to investigate the influence of pore size, temperature, molecule-molecule interactions, and molecule-wall interactions. The molecular parameters of each pure component are those of argon. Argon was chosen because it is a simple Lennard-Jones molecule which has often been used in density functional and molecular dynamics adsorption studies. However, a distinction was made between the two components by varying the interaction parameter  $k$  in equations 3.3.1-2 and 3.3.1-4 for the liquid-liquid and liquid-carbon interactions.

The adsorption characteristics were studied as a function of temperature and pore width for several interaction parameters  $k$ . By varying  $k$  a comparison was made between the adsorption of well miscible and poorly miscible mixtures and also between the adsorption of components with a strong interaction with carbon and components with a weak interaction with carbon. Also a comparison was made between the adsorption from vapour phase and the adsorption from liquid phase.

Tables 3.3.3-1 and 3.3.3-2 show the parameters that were used in the DFT-calculations.

**Table 3.3.3-1** General parameters used for calculation of the adsorption of several liquid mixtures in a carbon slit pore

Parameter	Unit	Value
$P^*$	-	0.1
$\Delta$	m	$0.335 \cdot 10^{-9}$
$\rho_w$	$\text{m}^{-3}$	$0.114 \cdot 10^{30}$
$\sigma_{1,l}, \sigma_{2,2}$	m	$0.341 \cdot 10^{-9}$
$\sigma_{w,w}$	m	$0.340 \cdot 10^{-9}$
$\varepsilon_{w,w}/k_B$	$\text{K}^{-1}$	28.0
$\varepsilon_{1,l}/k_B$	$\text{K}^{-1}$	119.8
$\varepsilon_{2,2}/k_B$	$\text{K}^{-1}$	119.8
$r_c$	-	7
$n_{grid}$	-	20

**Table 3.3.3-2** Parameters,  $k$ , used for the calculation of the adsorption of several liquid mixtures in a carbon slit pore

Case	$k_{w,1}$	$k_{w,2}$	$k_{l,2}$
1	1.2	-	-
2	0.8	-	-
3	1.2	1	0.8
4	1.2	0.8	0.8
5	1.2	0.8	0.6
6	1.4	0.8	0.8

The first and second case are the adsorption of a single component from the vapour phase. The difference between the two cases is the adsorbate-wall interaction. The bulk phase diagram for cases 1 and 2 is shown in figure 3.3.3-1. Cases 3 to 6 are the calculations of the adsorption of two components from a liquid phase. All two component calculations were carried out at a dimensionless pressure  $P^*=0.1$ . Figure 3.3.3-2 shows the liquid-liquid bulk phase diagram for cases 3, 4 and 6, which all have the same bulk properties. Figure 3.3.3-3 shows the liquid-liquid bulk phase diagram for case 5.

The sorption isotherms were calculated for several temperatures for a number of pore widths.

In each two-component case, component number one can be considered as the adsorbate and component number two as the solvent. A selection of the adsorbate sorption isotherms is shown in figures 3.3.3-4 to 3.3.3-8. In table 3.3.3-3, the solubilities of the adsorbate in the solvent are shown for the selected temperatures.

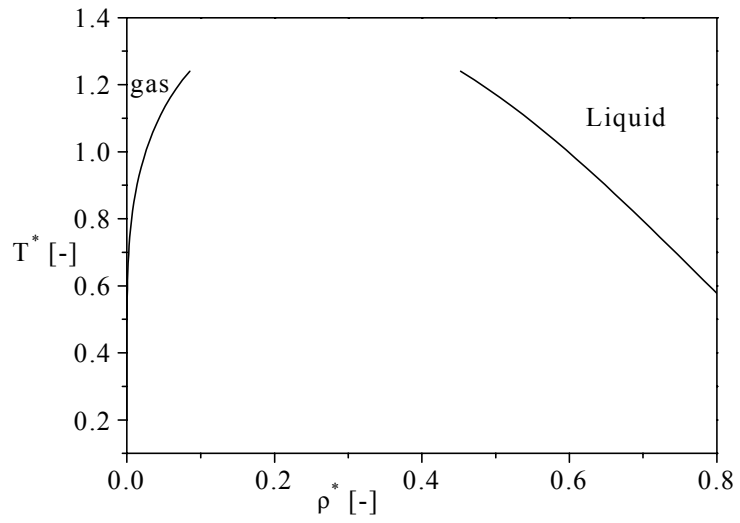


**Fig. 3.3.3-1** Bulk liquid-vapour phase diagram as calculated from the parameters of table 3.3.3-1.

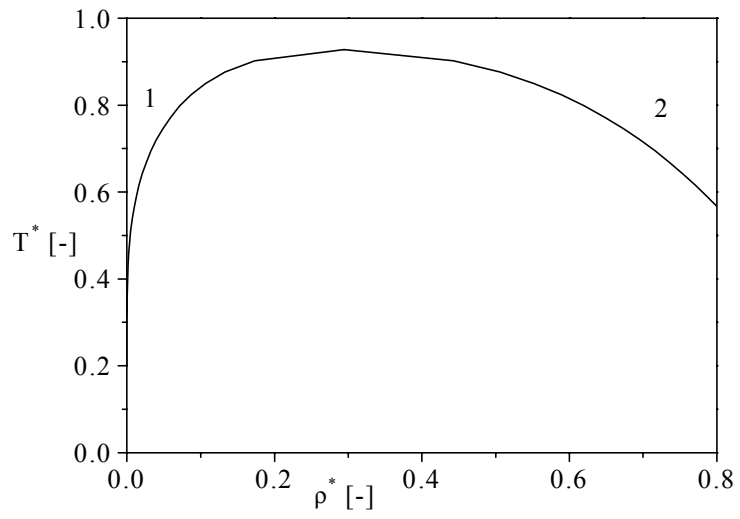


**Fig. 3.3.3-2** Bulk liquid-liquid phase diagram for cases 3, 4 and 6.

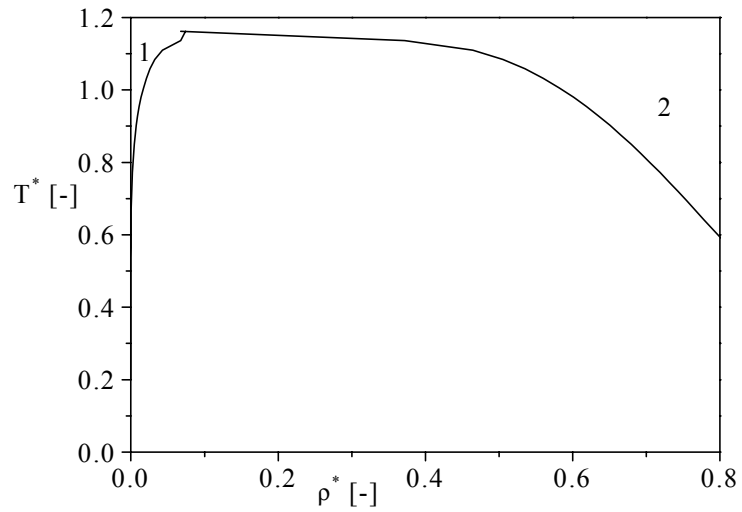


**Fig. 3.3.3-3** Bulk liquid-liquid phase diagram for case 5.

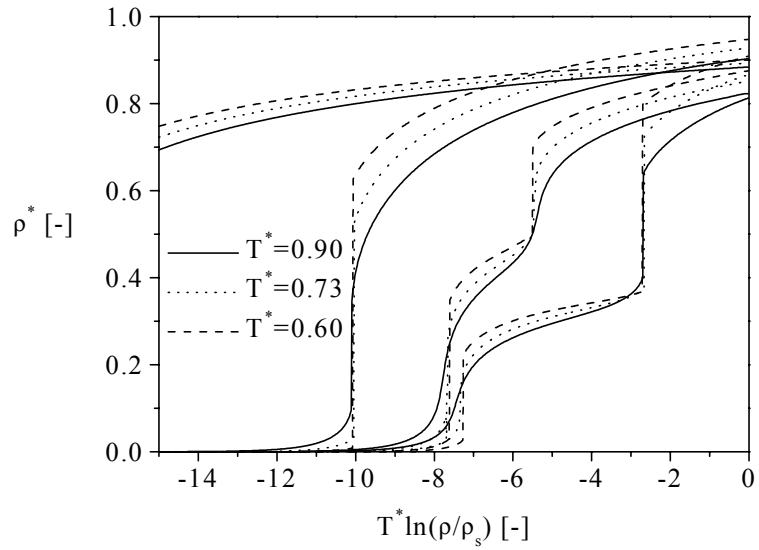


**Fig. 3.3.3-4** Case 1. Sorption isotherms at 3 different temperatures and 4 pore widths. Pore widths from left to right: 1.00, 1.82, 3.00 and 4.48 molecular diameters.

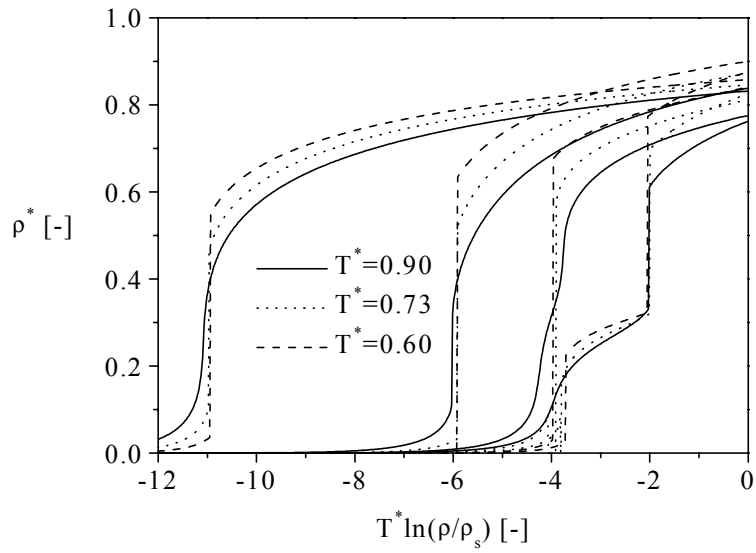


**Fig. 3.3.3-5** Case 2. Sorption isotherms at 3 different temperatures and 4 pore widths. Pore widths from left to right: 1.00, 1.82, 3.00 and 4.48 molecular diameters.

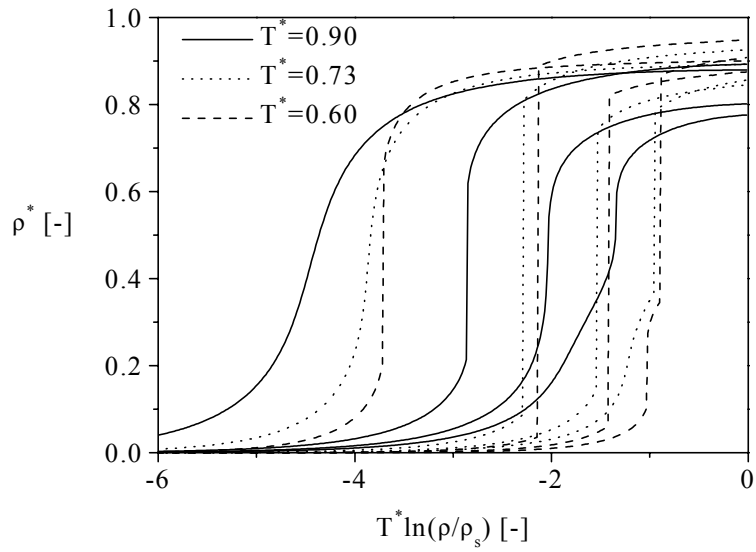


**Fig. 3.3.3-6** Case 3. Sorption isotherms at 3 different temperatures and 4 pore widths. Pore widths from left to right: 1.00, 1.82, 3.00 and 4.48 molecular diameters.

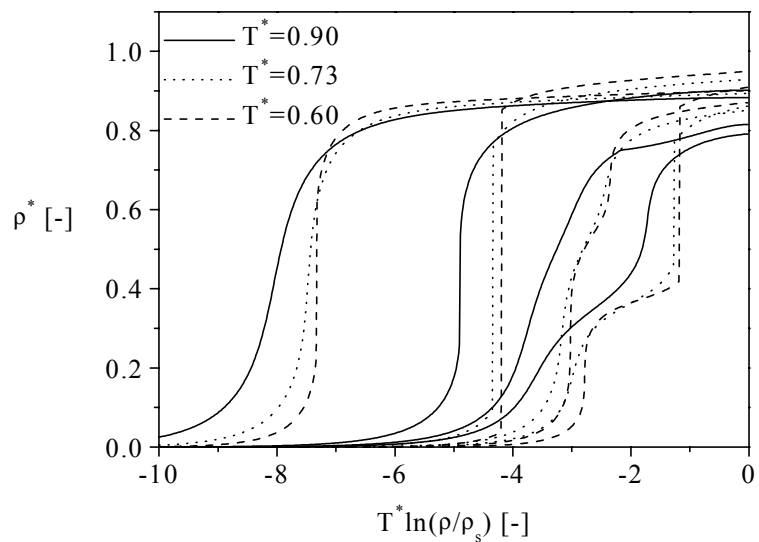


**Fig. 3.3.3-7** Case 4. Sorption isotherms at 3 different temperatures and 4 pore widths. Pore widths from left to right: 1.00, 1.82, 3.00 and 4.48 molecular diameters.

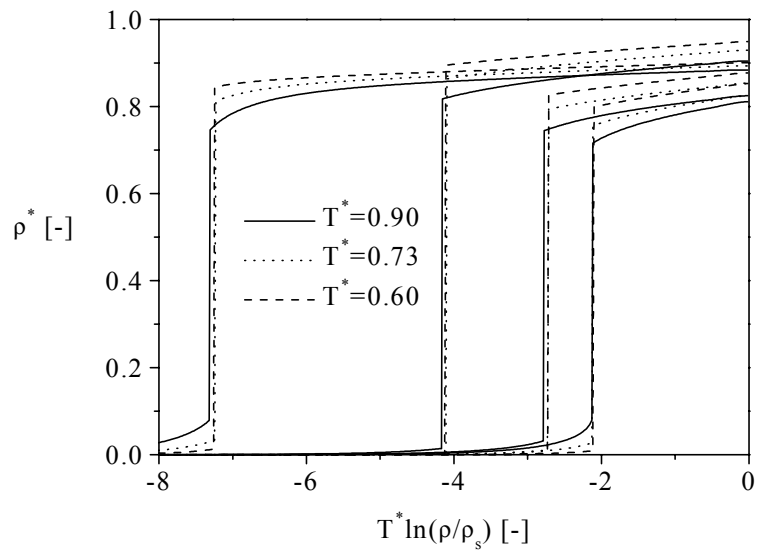


**Fig. 3.3.3-8** Case 5. Sorption isotherms at 3 different temperatures and 4 pore widths. Pore widths from left to right: 1.00, 1.82, 3.00 and 4.06 molecular diameters.

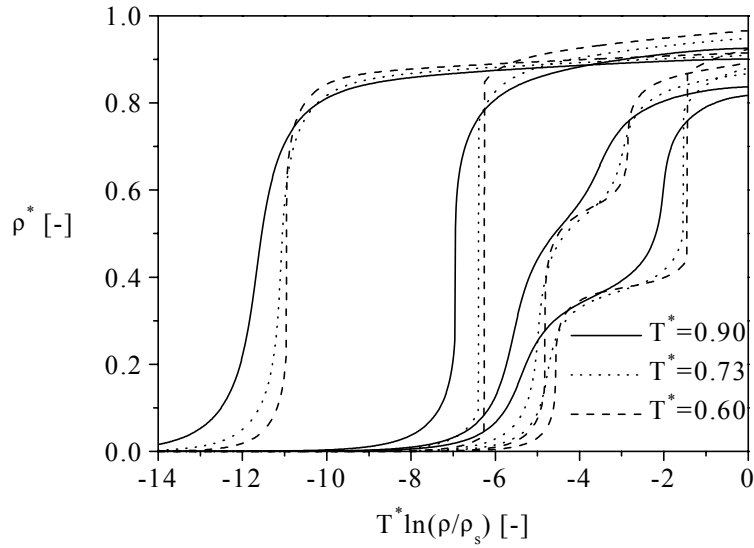


**Fig. 3.3.3-9** Case 6. Sorption isotherms at 3 different temperatures and 4 pore widths. Pore widths from left to right: 1.00, 1.82, 3.00 and 4.48 molecular diameters.

**Table 3.3.3-3** Solubilities of component 1 ( $\rho_{l,s}^*$ ) in the bulk mixture.  $\rho_{tot}^*$  is the total dimensionless bulk density.

Case	$T^*=0.60$		$T^*=0.73$		$T^*=0.90$	
	$\rho_{l,s}^*$	$\rho_{tot}^*$	$\rho_{l,s}^*$	$\rho_{tot}^*$	$\rho_{l,s}^*$	$\rho_{tot}^*$
3,4,6	0.0138	0.796	0.044	0.729	0.170	0.618
5	0.000181	0.798	0.00136	0.737	0.00728	0.659

### 3.3.3.2. Discussion

For the adsorption at different temperatures, it is clear that the pores are filled at about the same  $T^* \ln\left(\frac{\rho}{\rho_s}\right)$ , which is according to the potential theory (see section 2.3.3.3). This is not the case for the liquid-liquid mixtures of calculations 3, 4 and 6 at  $T^*=0.90$ . At this temperature, the solubility for those mixtures is high. Therefore, the chemical potential cannot be approximated with

$$T^* \ln\left(\frac{\rho}{\rho_s}\right).$$

Comparing the different liquid-liquid cases mutually, the following differences are found:

- *Cases 3 and 4.* A larger interaction of the solvent with the pore wall results in pore filling at larger concentrations in case 3 than in case 4. This is even more pronounced for the filling of the first mono-layer. In case 3 the middle of the pore is almost immediately filled after the first mono-layer was completed.
- *Cases 4 and 5.* The solubility of the adsorbate is smaller in case 5 than in case 4. Because in case 5, the interaction between the film layer and the middle of the pore is not very favourable, capillary phase separation takes place without preceding film layer formation. Also, in case 5, there is no continuous pore filling at high temperatures because of the low solubility of the adsorbate in the solvent.
- *Cases 4 and 6.* A larger interaction of the adsorbate with the pore wall results in pore filling at lower concentrations in case 6 than in case 4. This is even more pronounced for the filling of the first mono-layer because the adsorbate in case 6 is situated even more favourably near the pore wall than in the middle of the pore, in comparison with case 4.

In the following, a quantitative comparison is made between the adsorption from the vapour phase and the adsorption from the liquid phase. This is done, using simple thermodynamics, the schematic isotherm in figure 3.3.3-10 and the scheme in figure 3.3.3-11.

Figure 3.3.3-10 represents a sorption isotherm with a phase separation point at adsorbate bulk density  $\rho_{b,psp}^*$ . Situation *A* in figure 3.3.3-11 represents an infinite slit pore that has been filled with solvent. Further, there is an infinite almost pure liquid solvent phase, with a relatively small amount of adsorbate,  $n_{ads}$  [mole] dissolved in it. And also, there is an infinite pure adsorbate phase present.

Remove solvent from the pore to a bulk vapour phase at vapour phase density  $\rho_{b,psp}^*$  does not involve a change in free energy, because pore and bulk are in equilibrium at the phase transition point.

But, when the solvent is removed from the pore to the liquid solvent phase (situation *A* to situation *B*), an energy,  $\Delta E_{A \rightarrow B}$ , is needed, exactly equal to the free energy difference between the two phases [Ruthven, 1984, p. 55]. Suppose,  $dn_{sol}$  [mole] is the amount of solvent that is removed.  $\rho_{0,v,sol}$  is the saturated bulk vapour density of the solvent, which is the vapour density that is in equilibrium with the almost pure solvent phase. Then with  $\rho_{v,sol}^* = \rho_{b,psp}^*$  for the sorption isotherm of the solvent from vapour phase:

$$\Delta E_{A \rightarrow B} = -dn_{sol} R_g T \ln \left( \frac{\rho_{v,sol}}{\rho_{0,v,sol}} \right) \quad (3.3.3-1)$$

because this is the free energy difference between the pure liquid solvent and the solvent at vapour density  $\rho_{v,sol}^*$ , which on its turn is in equilibrium with the solvent in the pore at the phase separation point.

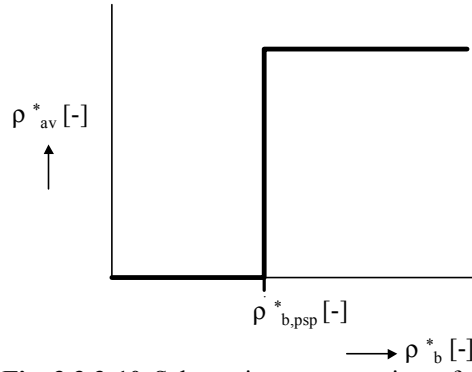


**Fig. 3.3.3-10** Schematic representation of a sorption isotherm for a single pore. At bulk density  $\rho^*_{b,psp}$ , a capillary phase separation step occurs.

Next ( $B \rightarrow C$ ), the pore is filled with adsorbate by moving  $dn_{ads}$  moles from the liquid adsorbate phase to the pore. Analogous to equation 3.3.3-1 an energy

$$\Delta E_{B \rightarrow C} = dn_{ads} R_g T \ln \left( \frac{\rho_{v,ads}}{\rho_{0,v,ads}} \right) \quad (3.3.3-2)$$

is needed, with  $\rho^*_{v,ads} = \rho^*_{b,psp}$  in the sorption isotherm of the adsorbate from vapour phase.

Suppose, the pore and the solvent phase are in equilibrium, exactly at the phase separation point. This means that  $\Delta E_{C \rightarrow D} = 0$ .

For the removal of  $dn_{ads}$  from the liquid solvent phase to the pure adsorbate phase an energy

$$\Delta E_{D \rightarrow E} = -dn_{ads} R_g T \ln \left( \frac{\rho_{l,ads}}{\rho_{s,l,ads}} \right) \quad (3.3.3-3)$$

is needed. Here  $\rho_{s,l,ads}$  is the solubility of the adsorbate in the solvent phase and  $\rho_{l,ads}$  is the density of adsorbate in the solvent phase. Since figures  $A$  and  $E$  represent the same physical situation, the following equation is valid:

$$\Delta E_{A \rightarrow B} + \Delta E_{B \rightarrow C} + \Delta E_{C \rightarrow D} + \Delta E_{D \rightarrow E} = 0 \quad (3.3.3-4)$$

After substitution of the different terms this results in

$$\begin{aligned} -dn_{sol} R_g T \ln \left( \frac{\rho_{v,sol}}{\rho_{0,v,sol}} \right) + dn_{ads} R_g T \ln \left( \frac{\rho_{v,ads}}{\rho_{0,v,ads}} \right) \\ - dn_{ads} R_g T \ln \left( \frac{\rho_{l,ads}}{\rho_{s,l,ads}} \right) = 0 \end{aligned} \quad (3.3.3-5)$$

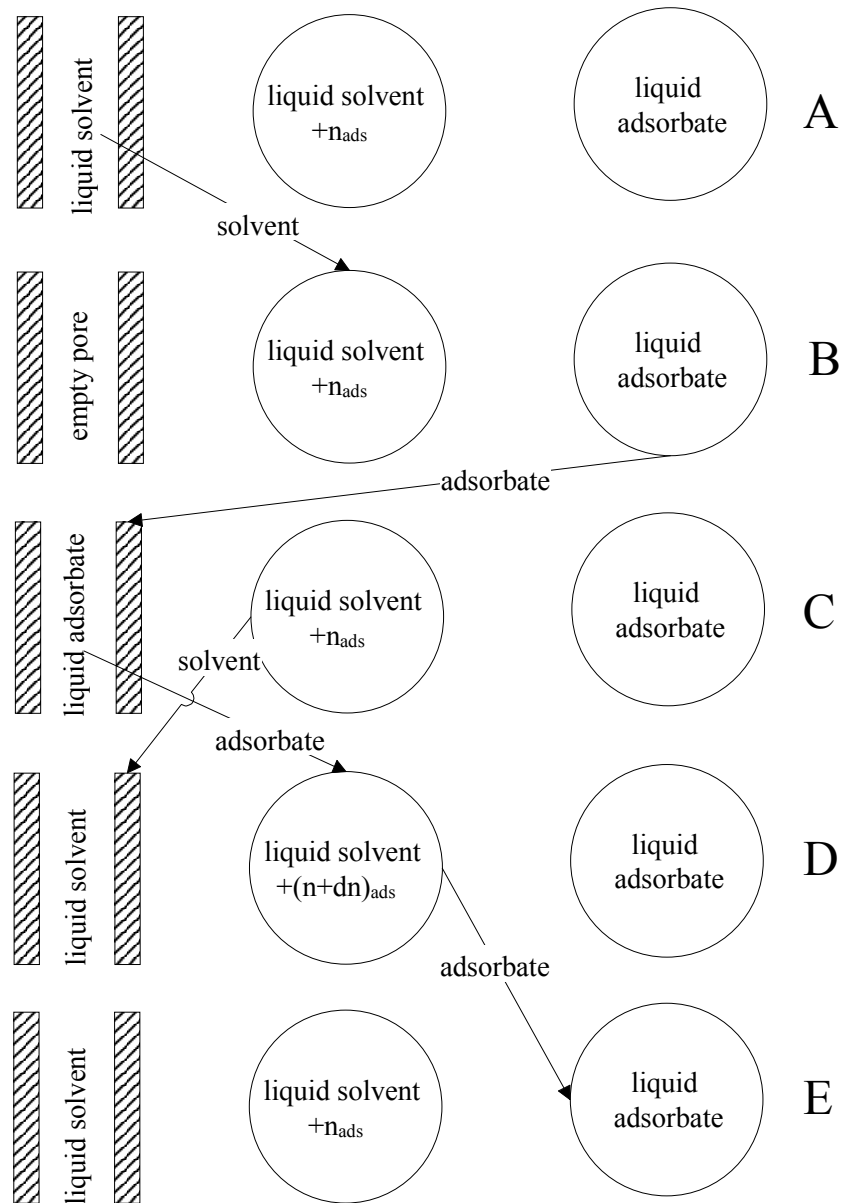


**Fig. 3.3.3-11** Energy diagram for capillary phase separation. Figures from left to right represent respectively an infinite slit pore, an infinite solvent phase and an infinite adsorbate phase.

With the approximation that the molar volumes of both adsorbate and solvent are equal inside the pore in situations *C* and *D*, thus  $dn_{sol} = dn_{ads}$ , it follows from equation 3.3.3-5 that

$$\ln\left(\frac{\rho_{l,ads}}{\rho_{s,l,ads}}\right) = \ln\left(\frac{\rho_{v,ads}}{\rho_{0,v,ads}}\right) - \ln\left(\frac{\rho_{v,sol}}{\rho_{0,v,sol}}\right). \quad (3.3.3-6)$$

For convenience this equation is written as

$$term_1 = term_2 - term_3 \quad (3.3.3-7)$$

Thus,  $term_1$  in equation 3.3.3-7 is calculated from the capillary phase separation point for the liquid-liquid adsorption.  $term_2$  and  $term_3$  are calculated from the capillary phase separation (capillary condensation) point for the vapour phase sorption isotherm of the adsorbate, respectively the solvent.

This result is applied to the sorption isotherms of cases 1, 2, 4 and 5. Because the derivation above is only valid for low solubility of the adsorbate in the solvent, only  $T^*=0.60$  is considered.

The results are shown in table 3.3.3-4. The values of the third and the sixth column are reasonably in agreement. This states that the multi-component sorption isotherm for a poorly soluble adsorbate may be estimated from the pure vapour phase isotherms of adsorbate and solvent, following the procedure that was described above.

**Table 3.3.3-4** Capillary phase separation data

Calc. No.	$w^*$	$T^*.term_1$	$T^*.term_2$	$T^*.term_3$	$T^*.term_2-term_3$
4	1.82	-4.2	-10.1	-5.9	-4.2
	3.00	-2.2	-5.6	-3.9	-1.7
	4.48	-1.2	-2.7	-1.9	-0.8
5	1.82	-4.2	-10.1	-5.9	-4.2
	3.00	-2.7	-5.6	-3.9	-1.7

## References

- Barker, J. and Henderson, D.; J.Chem.Phys 47, p. 4714, 1967.
- Bouyermaouen, A., Kerkhof, P.A.J.M., van der Zanden A.J.J.; 'Molecular-dynamics simulations of fluid benzene adsorbed between graphite surfaces', submitted for publication in Langmuir, 2001.
- Curtin, W.A. and Ashcroft, N.W., Phys. Rev. A, 32, p. 2909, 1989.
- Davis, H.T.; 'Statistical mechanics of phases, interfaces, and thin films', New York:VCH Publishers, Inc., 1996.
- Gregg, S.J. and Sing, K.S.W.; 'Adsorption, surface area and porosity', 2<sup>nd</sup> ed., London, Academic Press, 1982.
- Groot, R.D.; 'Density functional models for inhomogeneous hard sphere fluids', Molecular physics 60 no.1, p. 45-63, 1987.
- Kierlik, E. and Rosinberg, M.L.; 'Density-functional theory for inhomogeneous fluids: Adsorption of binary mixtures', Physical review A 44 no.8, p5025-5037, 1991.

Kierlik, E. and Rosinberg, M.L.; 'Free-energy density functional for the inhomogeneous hard-sphere fluid: Application to interfacial adsorption' Physical review A 42 no.6, p.3382-3387, 1990.

Kierlik, E., Rosinberg, M., Finn, J.E., and Monson, P.A.; 'Binary vapour mixtures adsorbed on a graphite surface: A comparison of mean field density functional theory with results from Monte Carlo simulations' Molecular physics 75 no.6, p.1435-1454, 1992.

Kierlik E., Fan Y., Monson, P.A.; 'Liquid-liquid equilibrium in a slit pore: Monte Carlo simulation and mean field density functional theory', J.Chem.Phys, 102 (9), 1995.

Kozak, E. and Sokolowski, S.; 'Wetting transitions and capillary condensation in Slit-like pores: Comparison of simulation and density functional theory', J.Chem.Soc.Faraday Trans. 87(20), p. 3415-3422, 1991.

Lastoskie, C., Gubbins, K.E., and Quirke, N.; 'Pore size heterogeneity and the carbon slit pore: a density functional theory model', Langmuir 9, p.2693-2702, 1993.

Meister, T.F. and Kroll, D.M.; 'Density-functional theory for inhomogeneous fluids: Application to wetting', Physical review A 31 no. 6, p.4055-4057, 1985.

Ruthven, D.M.; 'Principles of adsorption and adsorption processes', New York:John Wiley & Sons, a Wiley-Interscience Publication, 1984.

Sliwinska-Bartkowiak, M., Gras, J., Sikorski, R., Radhakrishnan, R., Gelb, L., and Gubbins, K.E.; 'Phase transitions in pores: experimental and simulation studies of melting and freezing', Langmuir 15, p. 6060-6069, 1999.

Sliwinski-Bartkowiak, M., Sowers, S.L., and Gubbins, K.E.; 'Liquid-Liquid phase equilibria in porous materials', Langmuir 13, p.1182-1188, 1997.

Steele, W.A.; Surf.Sci 36,p. 317, 1973.

Tamon, H. and Okazaki, M.; 'Desorption characteristics of aromatic compounds in aqueous solution on solid adsorbents', J.Colloid.interf.Sci. 179, p.181-187, 1996.

Tarazona, P.; 'Free-energy density functional for hard spheres', Physical review A 41, no.4, p.2672-2679, 1985.

Weeks, J.D., Chandler, D., and Andersen, H.L; J.Chem.Phys 54, p.5237, 1971.

## Symbols

*Note:* all parameters in sections 3.2.2, 3.2.3 and 3.2.4 are dimensionless according to the definitions in section 3.2.2.

*Greek symbols:*

$\delta(r)$	-	Dirac delta function
$\Delta$	m	distance between pore wall layers
$\epsilon_{i,j}$	J	energy parameter
$\theta$	rad.	contact angle of capillary meniscus
$\Theta(r)$	-	Heaviside function
$\Lambda$	m	deBroglie wavelength
$\mu$	J	chemical potential
$\mu_{\infty}$	J	bulk chemical potential

$\sigma_{i,j}$	m	Lennard-Jones size parameter
$\sigma_{fg}$	N.m <sup>-1</sup>	surface tension between the first molecular layer and the gas phase
$\sigma_{lf}$	N.m <sup>-1</sup>	surface tension between the first molecular layer and the liquid adsorbate
$\sigma_{lg}$	N.m <sup>-1</sup>	liquid/gas surface tension
$\omega_k$		four independent weight functions
$\rho$	m <sup>-3</sup>	number density
$\rho_l$	m <sup>-3</sup>	liquid density
$\rho_b$	m <sup>-3</sup>	density in bulk
$\rho_{av}$	m <sup>-3</sup>	average density in pore
$\rho(\mathbf{r})$	m <sup>-3</sup>	number density at position $\mathbf{r}$
$\Phi_{PY}$	m <sup>-3</sup>	free energy density
$\omega_0, \omega_1, \omega_2, \omega_3$		independent weight functions
$\Omega$	J	grand potential

*Latin symbols:*

$A$	m <sup>2</sup>	surface of a slit wall
$d_{hs}$	m	The hard sphere diameter
$F[\{\rho_i\}]$	J	intrinsic Helmholtz free energy functional
$F_a$	J	results from the attractive forces between the molecules
$F_r$	J	results from repulsive forces
$F_{r,ex}$	J	excess part
$F_{r,id}$	J	ideal gas term
$h_P$	J.s	Planck's constant
$k_B$	J.K <sup>-1</sup>	Boltzmann's constant
$m$	kg	molecular mass
$n$	-	number of components
$n_{ads}$	mole	amount of adsorbate
$n_0, n_1, n_2, n_3$	m <sup>-3</sup>	smoothed densities
$N$	-	number of particles
$P$	Pa	bulk pressure
$P_0$	Pa	saturated vapour pressure
$r_c$	m	cut-off radius
$R_{hs}$	m	hard sphere radius
$r_m$	m	radius (equation 3.2.1-8)
$\mathbf{r}$	m	position vector
$r$	m	position coordinate
$T$	K	absolute temperature
$T_c$	K	critical temperature
$u_{i,j}$	J	fluid-fluid potential
$u_{LJ,i,j}$	J	fluid-fluid potential
$V$	m <sup>3</sup>	systems volume
$v(\mathbf{r})$	J	external potential
$v_i(\mathbf{r})$	J	external potential
$V_m$	m <sup>3</sup> .mole <sup>-1</sup>	molar volume
$w$	m	slit width
$x$	-	mole fraction
$x$	m	position coordinate

*subscripts:*

$\infty$	indicates bulkproperty
$i,j$	component numbers
$psp$	phase separation point
$s$	indicates solubility
$sol$	solvent
$ads$	adsorbate
$v$	vapour
$w$	indicates pore wall

*superscripts:*

*	indicator for dimensionless parameter
---	---------------------------------------

## 4. Capillary transport in adsorption from liquid phase on activated carbon\*

### 4.1. Introduction

Adsorption of organic compounds from aqueous solution on activated carbon is a separation process widely used in industry and environmental technology. The descriptions of adsorption kinetics for activated carbon are considerably less developed than that for microcrystalline solids like zeolites (e.g. Kärger & Ruthven, [1992]).

In general the transport of adsorbate can be described by means of an effective diffusivity,  $D'_a$ , defined by the Fickian equation:

$$J_a = -D'_a \rho_{app} \frac{\partial Q}{\partial x} \quad (4.1-1)$$

$J_a$  is the adsorbate flux,  $\rho_{app}$  the apparent density of the adsorbent,  $Q$  the carbon loading and  $x$  the position co-ordinate. Although equation 4.1-1 is often used to model transport in porous media, it is physically not very relevant. The effective diffusion coefficient will in general depend on carbon structure, loading and temperature. In this chapter two physical expressions are derived for  $D'_a$ , both based on capillary flow as the mechanism for the transport of adsorbed component.

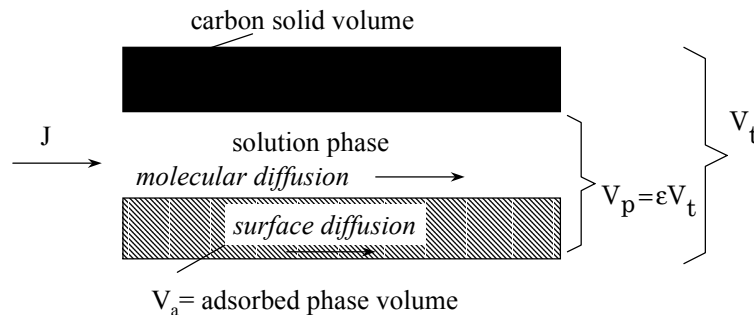


**Fig. 4.1-1** Schematic representation of a model for parallel surface and molecular diffusion.

The transport of some components in activated carbon takes place at a much higher rate than predicted by molecular diffusion transport. The adsorption of nitrobenzene from aqueous solution is often reported in this context [van Lier, 1989; Kouyoumdjiev, 1992; Miyahara and Okazaki, 1993]. An often proposed mechanism for this is the transport by surface diffusion, parallel to the molecular diffusion inside the (macro-)pore liquid. The surface diffusion is imagined as the hopping or sliding of molecules along the pore walls. Local

\* This chapter has been published: Frans B. Aarden, Piet J.A.M. Kerkhof, Antonius J.J. van der Zanden, AIChE Journal, vol. 45, no. 2, pp. 268, 1999.

equilibrium between pore solution and adsorbed phase is assumed. This is illustrated schematically in figure 4.1-1.

Formally, equation 4.1-1, for this parallel transport, is written as:

$$J = J_w + J_a = -(D'_w + D'_a)\rho_{app} \frac{\partial Q}{\partial x} \quad (4.1-2)$$

in which the subscripts *w* and *a* denote the water (solution) phase and adsorbed phase respectively. For the contribution of the aqueous phase diffusion in the larger pores:

$$J_w = -\frac{D_w \varepsilon}{\tau} \left(1 - \frac{V_a}{V_p}\right) \frac{\partial C}{\partial x} = -\frac{D_w \varepsilon}{\tau} \left(1 - \frac{V_a}{V_p}\right) \frac{\partial Q}{\partial x} / \frac{\partial Q}{\partial C} \quad (4.1-3)$$

And so

$$D'_w = \frac{D_w \varepsilon}{\tau} \left(1 - \frac{V_a}{V_p}\right) / \left(\rho_{app} \frac{\partial Q}{\partial C}\right) \quad (4.1-4)$$

is obtained. *C* is the adsorbate concentration in the water phase, *D<sub>w</sub>* the diffusion coefficient of the adsorbate in water, *τ* the tortuosity, *V<sub>p</sub>* the total pore volume, *V<sub>a</sub>* is the pore volume filled with adsorbate and *ε* is the porosity. The term  $\varepsilon(1-V_a/V_p)$  is the fraction of the volume that is available for transport by molecular diffusion. For a known porosity, *ε*, this term and the derivative  $\partial Q/\partial C$  follow from the sorption isotherm.

In figure 4.1-2, the value of *D<sub>w</sub>* is compared with the experimental data of Miyahara and Okazaki for the effective diffusion coefficient of nitrobenzene in Takeda X-7000 activated carbon at three temperatures. The diffusion coefficient *D<sub>w</sub>* of nitrobenzene in water is estimated from the experimental value of  $9.25 \cdot 10^{-10}$  m<sup>2</sup>/s at 21.5 °C [Kouyoumdjiev, 1992] and the Stokes-Einstein relation; the results are given in table 4.1-1.

**Table 4.1-1** Physical data of nitrobenzene and benzonitrile as function of temperature. [Miyahara and Okazaki, 1993; Lide, 1996].

<i>T</i> [K]	Solubility [kg.m <sup>-3</sup> ]	Viscosity [mPa.s]	Density [kg.m <sup>-3</sup> ]	Interfacial tension [N.m <sup>-1</sup> ]	Diffusion coefficient in water* 10 <sup>-9</sup> m <sup>2</sup> s <sup>-1</sup>
Nitrobenzene					
293	1.84	2.06	1200	0.0257	0.89
308	2.2	1.6	1190	-	1.29
323	2.6	1.27	1170	-	1.81
Benzonitrile					
293	4.0	1.36	1000	0.028	0.89
308	4.8	1.09	990	-	1.29

\*For nitrobenzene derived from Kouyoumdjiev and application of Stokes-Einstein relation. For benzonitrile the same values were taken as for nitrobenzene.

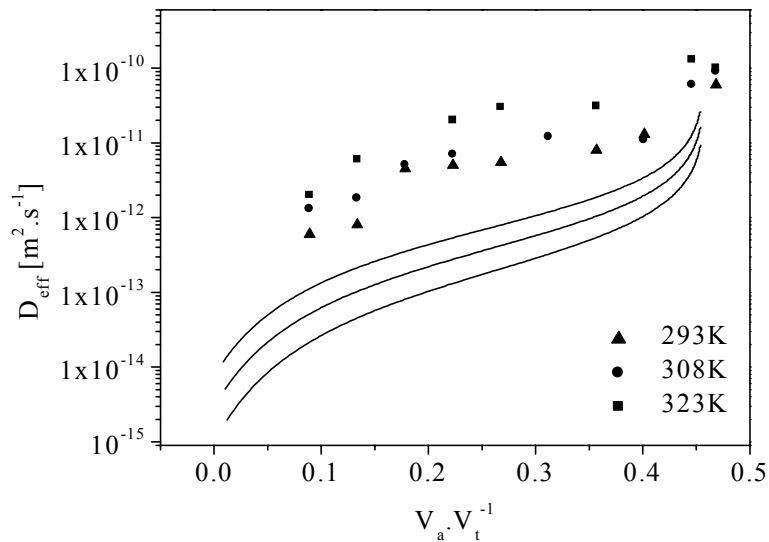


**Fig. 4.1-2** Dependency of diffusivity of nitrobenzene on volume fraction filled with nitrobenzene at different temperatures. Comparison of the experimental data of Miyahara and Okazaki (1993) with  $D'_w$ , the contribution of molecular diffusion in the aqueous phase. Assumed is minimum tortuosity  $\tau=1$ .

Even for the minimal tortuosity factor  $\tau=1$  it can be seen from figure 4.1-2 that the contribution of the aqueous phase diffusion is very low.

For the surface diffusion in the adsorbed phase various models have been presented in the literature. Van Lier [1989], and Miyahara and Okazaki took a Fickian type of equation as equation 4.1-1 in which the gradient in loading is the driving force for surface diffusion. In our laboratory a Maxwell-Stefan model was developed, in which the driving force for surface diffusion is the gradient in chemical potential [Kouyoumdjiev, 1992], starting from the model of Krishna [1990].

Although the results macroscopically can agree reasonably well with experimental data, often the problem arises that the diffusion coefficients found depend on external concentration, particle size etc. [van Lier, 1989], indicating that the modelling is incomplete. Also the parallel model has a disadvantage from a physical point of view: in the macro-pores hardly any surface is present, while in the micro-pores hardly any liquid diffusion may be expected.

More extended models differentiate between macropore and microparticle diffusion, which lead to coupled models on the particle scale [Ma & Lee, 1976, van Lier, 1989]. Overviews are given by Yang [1987] and Kärger & Ruthven [1992]. The bi-porous model is used by van Lier to explain the influence of the initial concentration of the adsorbate and the carbon dose on adsorption kinetics, which cannot be explained with homogeneous models. The biporous

model, however, contains parameters, which can hardly be obtained independently by experiments.

In their study of the transport of gases Tamon et al. [1981] showed that the diffusion in the adsorbed phase could well be described by the additivity of surface hopping and capillary flow, for the region in which capillary condensation occurs. Rajniak and Yang [1996] used a network model for predicting effective Fickian diffusivities of condensable vapours in porous media where capillary condensation and adsorption - desorption hysteresis occur. The network Rajniak and Yang used was a Bethe Tree. Using a combination of surface diffusion and capillary transport caused by a gradient of capillary pressure, as transport mechanisms, they were able to predict successfully the concentration dependency of the effective diffusivity in the whole range of relative pressures for different adsorbent/adsorbate systems.

For drying of porous materials van der Zanden et al. [1996] developed a model for the partially saturated region in which capillary flow was the mechanism for liquid water transport. Their results agreed well with the experimental data on the effective water diffusion coefficient in clay as a function of water content. They explicitly formulated the effective diffusivity in terms of the pore size distribution.

For the adsorption equilibrium between activated carbon and aqueous solutions recently a theory based on Capillary Phase Separation was presented by Miyahara & Okazaki [1992, 1993], Okazaki [1993], Miyahara et al. [1994]. This may be considered as an analogy of the capillary condensation for adsorption from the vapour phase such as developed by Okazaki et al [1978] for the study of binary equilibria between vapour and activated carbon. The basic phenomenon was described decades earlier by Patrick & Jones [1925] and Patrick & Ebermann [1925]. As shown by Miyahara & Okazaki [1992,1993,1994] the adsorption equilibrium isotherms for various organic compounds between water and activated carbon could be described well with the theory according to this concept.

For the case of adsorption from the liquid phase the transport of capillary separated phase under the influence of a gradient in capillary pressure has not been investigated in the literature. Since the equilibrium descriptions based on this model are promising, it was thought worthwhile to investigate also a transport model based on this concept. In the following two capillary flow models are presented, leading to expressions for the effective diffusion coefficient, along the lines of van der Zanden et al. [1996]. In the first model a flow of capillary separated adsorbate phase under influence of a gradient in capillary pressure is assumed, assuming the possibility of continuous percolation throughout the particle. In the second model capillary flow is assumed to occur in small regions, in series with solution-phase molecular diffusion in larger pores. Predictions of the effective diffusivities as a function of concentration and temperature are compared to experimental data from the literature [Miyahara & Okazaki, 1992; 1993].

## 4.2. Theory

### 4.2.1. Model I: Continuous Capillary Transport

The system considered here is depicted schematically in figure 4.2.1-1. The adsorbed phase is thought to be present as a separate phase in a fraction of the pores, separated from the aqueous solution by a curved interface.

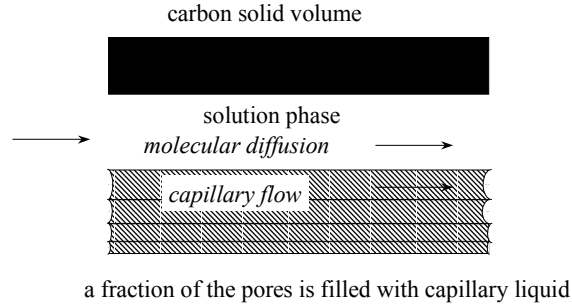


**Fig. 4.2.1-1** Schematic view of parallel capillary flow in adsorbate phase and molecular diffusion in aqueous phase, for continuous capillary flow (model I).

At a given concentration  $C$  in the aqueous phase the equilibrium meniscus radius  $r^*$  is given by the Kelvin equation [Miyahara & Okazaki, 1994]:

$$RT \ln \frac{C_s}{C} = \frac{2\sigma_w M_a \cos \vartheta}{\rho_a r^*} \quad (4.2.1-1)$$

where  $C_s$  is the adsorbate solubility,  $\rho_a$  the adsorbate density,  $M_a$  the molar mass of the adsorbate,  $\sigma_w$  the interfacial tension at the water/adsorbate interface, and  $\theta$  the contact angle of the adsorbate with the adsorbent.

This means that approximately at the given activity  $C/C_s$  the pores with radius  $r_m=r^*$  will be filled, as well as the smaller pores, of which the meniscus will have a smaller radius of curvature. For the load onto the carbon

$$\frac{V_a}{V_p} = \int_0^{r_m} f(r) dr \quad (4.2.1-2)$$

with

$$\frac{V_a}{V_p} = \frac{\rho_{app}}{\varepsilon \rho_a} Q \quad (4.2.1-3)$$

and  $f(r)$  is the volumetric pore size distribution, normalised at the total pore volume. The pore size distribution is calculated from the experimental sorption isotherm with equations 4.2.1-1 and 4.2.1-2.

As stated before, the capillary separated adsorbate phase is assumed to flow under influence of a gradient in capillary pressure. Pressure gradients in the aqueous phase, caused by viscous forces are neglected because the adsorbate

flow takes place in much smaller pores than the aqueous flow. Another assumption is that the pore structure consists of parallel cylindrical pores with a different diameter. Although the properties of the adsorbate, like viscosity, surface tension and density, will change close to the pore walls, in this approximate model such effects are not taken into account.

The superficial velocity  $u_c$  of the capillary separated adsorbate through a porous material under a pressure gradient  $dP/dx$ , is described for a Newtonian fluid by Darcy's law [Quintard & Todorovic, 1992]

$$u_c = -\frac{k_r k_\infty}{\mu_a} \frac{\partial P}{\partial x} \quad (4.2.1-4)$$

where  $P$  is the pressure in the adsorbate phase. The expression  $k_r k_\infty / \mu_a$ , in which  $k_r k_\infty$  is the effective permeability and  $\mu_a$  the adsorbate viscosity, may be regarded as the reciprocal of the resistance against transport of the capillary separated phase.

Then for the flux of adsorbate per unit adsorbent cross-section, the contribution of the capillary flow is:

$$J_a = -D'_a \rho_{app} \frac{\partial Q}{\partial x} = \rho_a u_c = -\rho_a \frac{k_r k_\infty}{\mu_a} \frac{\partial P}{\partial x}, \quad (4.2.1-5)$$

from which follows :

$$D'_a = \frac{1}{\varepsilon} \frac{k_r k_\infty}{\mu_a} \frac{\partial P}{\partial (V_a/V_p)}. \quad (4.2.1-6)$$

If the pores are assumed to have cylindrical geometry, the pressure difference over the water/adsorbate interface is calculated with the Laplace equation

$$P - P_w = -\frac{2\sigma_w \cos \theta}{r_m} \quad (4.2.1-7)$$

in which  $P_w$  is the pressure in the aqueous phase.

Differentiation of equation (4.2.1-7) gives:

$$\frac{\partial P}{\partial r_m} = \frac{2\sigma_w \cos \theta}{r_m^2} \quad (4.2.1-8)$$

From equation (4.2.1-2) it follows that

$$\frac{\partial (V_a/V_p)}{\partial r_m} = f(r_m) \quad (4.2.1-9)$$

and so :

$$\frac{\partial P}{\partial (V_a/V_p)} = \frac{2\sigma_w \cos \theta}{r_m^2 f(r_m)} \quad (4.2.1-10)$$

In one cylindrical pore, filled with adsorbate, the linear velocity  $u$  caused by a pressure gradient in the adsorbate is calculated as a Poiseuille flow

$$u = -\frac{r^2}{8\mu_a} \frac{\partial P}{\partial x} \quad (4.2.1-11)$$

For the average linear velocity  $\langle u \rangle$  over all pores

$$\langle u \rangle = \int_0^{r_m} u(r) f(r) dr = \int_0^{r_m} \left( -\frac{r^2}{8\mu_a} \frac{\partial P}{\partial x} \right) f(r) dr. \quad (4.2.1-12)$$

Relating the superficial velocity of the capillary transport to the linear velocity:

$$u_c = \varepsilon \langle u \rangle \quad (4.2.1-13)$$

gives:

$$k_r k_\infty = \frac{\varepsilon}{8} \int_0^{r_m} f(r) r^2 dr \quad (4.2.1-14)$$

Substitution of equations 4.2.1-10 and 4.2.1-14 in equation 4.2.1-6 then gives:

$$D'_{a,pc} = \frac{1}{4\mu_a} \frac{\sigma_w \cos\theta}{r_m^2 f(r_m)} \int_0^{r_m} r^2 f(r) dr, \quad (4.2.1-15)$$

in which the subscript pc stands for “parallel cylinders”. To include also here tortuosity effects and other deviations from the idealised parallel cylinder model a matching factor F, analogous to van der Zanden et al., is included :

$$D'_a = F D'_{a,pc} = \frac{F}{4\mu_a} \frac{\sigma_w \cos\theta}{r_m^2 f(r_m)} \int_0^{r_m} r^2 f(r) dr \quad (4.2.1-16)$$

and from equations 4.1-1 and 4.1-2, for the effective diffusion coefficient, the following expression is found:

$$D_{eff,l} = D'_w + D'_a = \frac{D_w \varepsilon}{\tau} \left( 1 - \frac{V_a}{V_p} \right) \left/ \left( \rho_{app} \frac{\partial Q}{\partial C} \right) \right. + \frac{F}{4\mu_a} \frac{\sigma_w \cos\theta}{r_m^2 f(r_m)} \int_0^{r_m} r^2 f(r) dr \quad (4.2.1-17)$$

#### 4.2.2. Model II: Discontinuous capillary transport

Now, within a representative element the capillary phase is taken to be continuous over a distance  $d_1$ , in series with an aqueous phase region over a distance  $d_2 = d_1/\delta$ , as represented in figure 4.2.2-1.

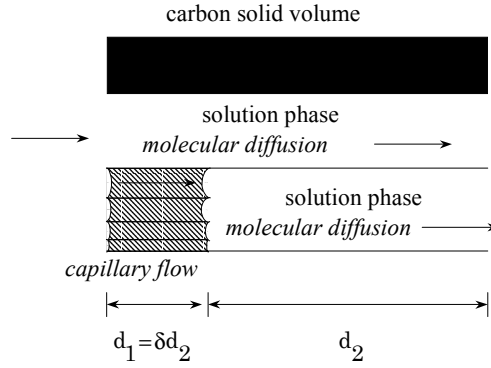


**Fig. 4.2.2-1** Schematic view of parallel capillary flow in adsorbate phase and molecular diffusion in aqueous phase, for discontinuous capillary flow (model II).

For the transport in the left-hand part of the system, the same transport equations hold as derived for Model I. Since all adsorbate is now thought to be present over the distance  $d_1$ , at a given load onto the carbon the cross-sections for water and adsorbate transport should be corrected for this. Thus, in the left-hand part

$$J = -(D'_{w,II} + D'_{a,II}) \rho_{app} \frac{\partial Q}{\partial x} \quad 0 < x < d_1 \quad (4.2.2-1)$$

with

$$D'_{w,II} = \frac{D_w \varepsilon}{\tau} \left( 1 - \frac{V_a}{V_p} \frac{1+\delta}{\delta} \right) / \left( \rho_{app} \frac{\partial Q}{\partial C} \right) \quad (4.2.2-2)$$

and

$$D'_{a,II} = \frac{F}{4\mu_a} \left( \frac{1+\delta}{\delta} \right) \frac{\sigma_w \cos \theta}{r_m^2 f(r_m)} \int_0^{r_m} r^2 f(r) dr. \quad (4.2.2-3)$$

For the aqueous phase part at the right-hand side

$$J = -D''_{w,II} \rho_{app} \frac{\partial Q}{\partial x} \quad d_1 < x < d_2 \quad (4.2.2-3)$$

with

$$D''_{w,II} = \frac{D_w \varepsilon}{\tau} / \left( \rho_{app} \frac{\partial Q}{\partial C} \right). \quad (4.2.2-4)$$

And so from the series arrangement of the two regions it is found that:

$$J = -D_{eff,II} \rho_{app} \frac{\partial Q}{\partial x} \quad (4.2.2-5)$$

with :

$$\frac{1}{D_{eff,II}} = \frac{\delta}{1+\delta} \frac{1}{D'_{w,II} + D'_{a,II}} + \frac{1}{1+\delta} \frac{1}{D''_{w,II}} \quad (4.2.2-6)$$

There are two limiting situations for  $\delta$ . If  $\delta \rightarrow \infty$  a situation is considered in which a continuous capillary separated adsorbate phase exists through the whole porous material. The adsorbate flux will then be given by model I. The minimum value for  $\delta$  follows from equation 4.2.2-1:

$$1 - \frac{V_a}{V_p} \frac{1 + \delta}{\delta} = 0, \quad (4.2.2-7)$$

and thus

$$\delta_{\min} = \frac{1}{\left(\frac{V_a}{V_p}\right)^{-1} - 1} \quad (4.2.2-8)$$

In this case there is only serial transport by molecular diffusion and capillary flow.

### 4.3. Results and discussion

Miyahara and Okazaki [1992,1993] measured the adsorption isotherms of nitrobenzene at 293K, 308K and 323K and benzonitrile at 293K and 308K, both from aqueous solution on activated carbon X-7000. They also measured the diffusion coefficients for both compounds as a function of carbon loading at the different temperatures.

The adsorption equilibria data of one component at different temperatures can be expressed by a single characteristic curve using the potential theory [Miyahara and Okazaki, 1993]. In such a plot the amount adsorbed is given as a function of  $RT \ln(C_s/C)$ . Potential plots were used to calculate the pore size distribution from the isotherms of nitrobenzene and benzonitrile via equations 4.2.1-1 and 4.2.1-2. The result is shown in figure 4.3-1. The validity of the potential theory indicates that the temperature dependency of  $\sigma_w \cos \theta$  in the Kelvin equation (4.2.1-1) is negligible.

The measured sorption isotherms gave no information about the pore volume fraction from zero to 0.05. To obtain this information, the isotherms were extrapolated to the lower carbon loading. In addition, the distribution of pores with a radius larger than 6 nm remains unknown, when using the sorption isotherms in calculating the pore size distribution.

The diffusivity for continuous capillary transport, Model I, was calculated from equation 4.2.1-17. Viscosity data at different temperatures were obtained from the Handbook of Chemistry and Physics [Lide, 1996]. The temperature dependency of the diffusivity via the temperature dependent surface tension is about one order of magnitude smaller than the temperature dependency of the diffusivity via the temperature dependent viscosity. That's why in the calculation of the effective diffusivity the dependency of surface tension on temperature was neglected. In table 4.1-1 some properties of nitrobenzene and benzonitrile are shown.

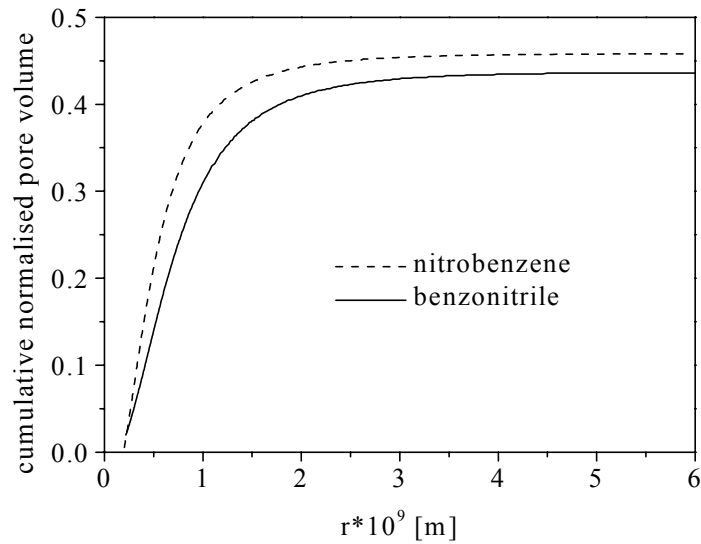


**Fig. 4.3-1** Normalised cumulative pore size distributions of activated carbon X-7000, obtained with equation 5 and 6 from the sorption isotherms of nitrobenzene and benzonitrile.

In figures 4.3-2 and 4.3-3 the effective diffusion coefficient,  $D_{eff}$ , calculated with model I, is compared to the experimental data of Miyahara and Okazaki for respectively nitrobenzene and benzonitrile. The pore size distribution, used in the calculation, was the pore size distribution calculated from the isotherm of the corresponding compound. The correction factor  $F$  in equation 4.2.1-17 equals 0.0125 in both cases. The correction factor is expected to be a constant for a particular porous material, because it is determined mainly by the pore structure. Translated to the model in this work, van der Zanden would have found a correction factor in the same order of magnitude for the drying behaviour of clay ( $F=0.01$ ) [van der Zanden et al., 1996; van der Zanden, 1995].

The model underestimates the temperature dependency of the diffusivity. Miyahara and Okazaki used Eyring's rate theory in combination with the potential theory of adsorption to model the same experimental data as used here [Miyahara and Okazaki, 1993]. If their model is compared to the model of capillary transport, used here, it is found that concerning the temperature dependency the two models are quite similar.

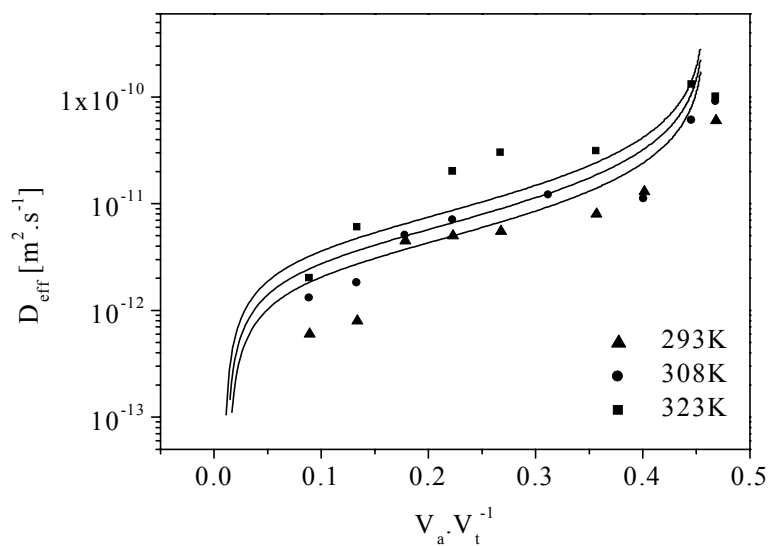


**Fig. 4.3-2** Dependency of diffusivity of nitrobenzene on volume fraction filled with nitrobenzene at different temperatures. Comparison of the experimental data of Miyahara and Okazaki [1993] with  $D_{eff,I}$ , calculated by model I.  $F=0.0125$ .

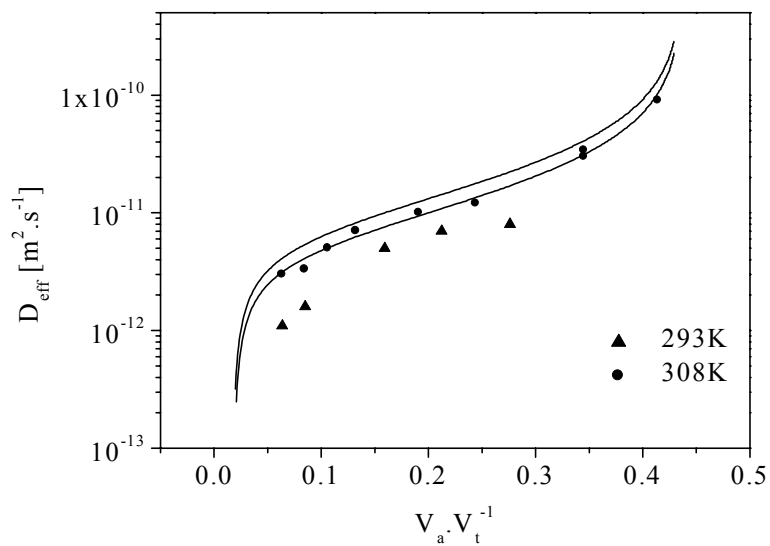


**Fig. 4.3-3** Dependency of diffusivity of benzonitrile on volume fraction filled with benzonitrile at different temperatures. Comparison of the experimental data of Miyahara and Okazaki [1993] with  $D_{eff,I}$ , calculated by model I.  $F=0.0125$ .

Miyahara and Okazaki found for the hole making step an activation free energy, comparable to the activation free energy for the viscosity of liquids.

The large difference between the models is that the capillary models account for the pore structure, as related to the sorption isotherm, and the surface diffusion model does not.

In figure 4.3-4 some results, calculated with model II, are given for the adsorption of nitrobenzene. The tortuosity and the correction factor  $F$  both equal 1.

For  $\delta = \delta_{\min} + 15$  a good coverage of experimental data was found.

The discontinuity of the capillary separated phase results in a calculated effective diffusivity, which is smaller at the same correction factor. Model II gives a good estimation of the temperature dependency of the effective diffusion coefficient. This is caused by the transport by molecular diffusion, which plays a limiting role in model II. This transport has a larger temperature dependency than the transport by capillary flow.

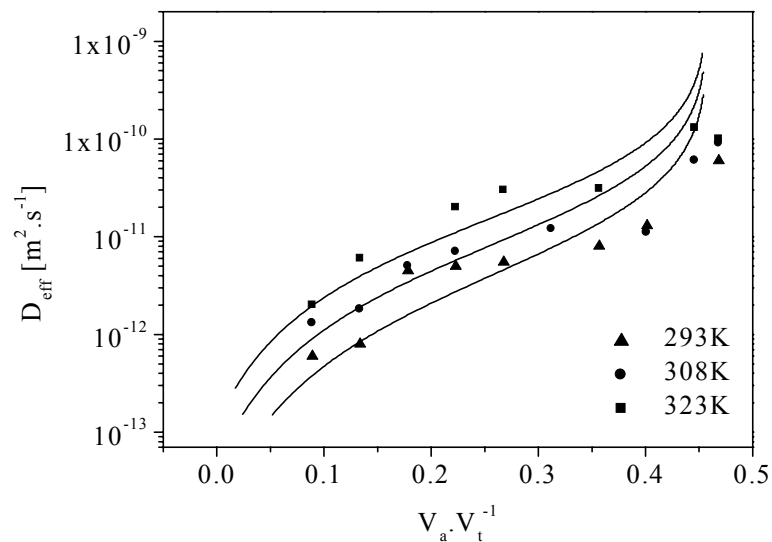


**Fig. 4.3-4** Dependency of diffusivity of nitrobenzene on volume fraction filled with nitrobenzene at different temperatures. Comparison of the experimental data of Miyahara and Okazaki [1993] with  $D_{eff,II}$ , calculated by model II.  $F=1$ ,  $\delta = \delta_{\min} + 15$ .

In this model  $\delta$  is fitted to obtain a good agreement with the experimental data. A possibility to avoid a fitting parameter like  $\delta$  is to model the pore structure as a network of connected cylinders [Koplik, 1982; Matthews, 1993]. In that case

the continuity of the adsorbate phase will be determined by the geometry of the network.

#### **4.4. Conclusions**

It has been shown that the assumption of solely molecular diffusion of adsorbate through the porous system underestimates the experimental effective diffusion coefficient.

Two models, based on capillary transport, were used to predict the diffusivities of the adsorption of nitrobenzene and benzonitrile on activated carbon from aqueous solution. The influence of carbon loading on the diffusivity is included in the pore structure, which is obtained from the adsorption isotherm of the adsorbate. Model I assumes a continuous capillary separated adsorbate phase. One fit parameter is needed, to correct for the pore structure and other deviations from reality. The fit parameter is the same for the two adsorbates, and thus characteristic for the adsorbent. The fit parameter is also found to be in the order of magnitude of the same fit parameter, found in modelling the drying behaviour of clay. The temperature dependency of the diffusivity is slightly underestimated by the model. The dependency of carbon loading on the diffusivity fits reasonably well.

Model II, in which capillary transport and molecular diffusion partly occur in series, gives a good estimation of the temperature and carbon loading dependency of the apparent diffusivity.

Although many physical phenomena will deviate on the molecular level from the simplified models used here, it is remarkable that a relatively simple transport theory such as capillary flow is able to give such a good description of such complex phenomena. It is therefore of interest on one hand to investigate this type of theory further for the purpose of engineering, and on the other hand to try to relate molecular science to the effective parameters used here.

#### **References**

Gregg S.J., and K.S.W. Sing "Adsorption, Surface Area and Porosity", 2nd, p.154, Academic Press, London (1993)

Kärger J., and D.M. Ruthven "Diffusion in Zeolites", John Wiley, NY (1992)

Koplik J. "Creeping flow in two-dimensional networks", J.Fluid Mech.,119, 219-247 (1982)

Kouyoumdjiev M.S. "Kinetics of adsorption from liquid phase on activated carbon", PhD.Thesis, Eindhoven University of Technology, The Netherlands (1992)

Krishna, R. "Multicomponent surface diffusion of adsorbed species: A description based on the generalized Maxwell-Stefan Equations", Chem. Eng. Sci., 45, 1779, (1990)

- Lide, D.R. "CRC Handbook of Chemistry and Physics", 77th, CRC Press, Inc., NY. (1996)
- Ma Y.H., and T.Y. Lee "Transient diffusion in solids with a bipore distribution" *AIChE J.*, 22(1), 147 (1976)
- Matthews G.P. "Network calculation of mercury intrusion and absolute permeability in sandstone and other porous media", *Powder Technology.*, 76, 95-107 (1993)
- Miyahara M., and M. Okazaki "Concentration dependence of surface diffusivity of nitrobenzene and benzonitrile in liquid phase adsorption onto an activated carbon", *J.Chem.Eng.Japan*, 25(4), 408-414 (1992)
- Miyahara M., and M. Okazaki "Correlation of concentration-dependent surface diffusivity in liquid phase adsorption", *J.Chem.Eng.Japan*, 25(5), 510-516 (1993)
- Miyahara M., and M. Okazaki "Studies in Surface Science and Catalysis", ed. Rouquerol J., vol.87, p.353, Elsevier Science B.V., Amsterdam, The Netherlands (1994)
- Okazaki M., H. Tamon, and R. Toei "Prediction of binary adsorption equilibria of solvent and water vapour on activated carbon", *J.Chem.Eng.Japan* 11, 209, (1978)
- Patrick W.A., and D.C. Jones "Studies in the adsorption from solution from the standpoint of capillarity I" *J.Phys.Chem.*, 29, 1 (1925)
- Patrick W.A., and N.F. Eberman "Studies in the adsorption from solution from the standpoint of capillarity II" *J.Phys.Chem.*, 29, 220 (1925)
- Perry R.H., and C.H. Chilton "Chemical Engineers' Handbook", 5th, p.3-246, McGraw-Hill Book Company, New York (1973)
- Quintard M., and M. Todorovic "Heat and Mass transfer in Porous Media", p.294, Elsevier Science Publishers B.V., Amsterdam (1992)
- Rajniak P., and R.T. Yang "Unified model for diffusion of condensable vapours in porous media", *AIChE Journal*, 42(2), 319 (1996)
- Tamon H., M. Okazaki, and R. Toei, "Flow mechanism of adsorbate through porous media in presence of capillary condensation", *AIChE.J.* 27(2), 271-277 (1981)
- van der Zanden A.J.J., W.J. Coumans, P.J.A.M. Kerkhof, and A.M.E. Schoenmakers "Isothermal moisture transport in partially saturated porous media", *Drying Technology*, 14(7&8), 1525-1542 (1996)
- van der Zanden A.J.J. "A possible revision of the results of a model for moisture transport in partially saturated porous media", *Drying Technology*, 13(8&9), 2227-2231 (1995)
- van Lier W.C. "Mass transfer to activated carbon in aqueous solutions", PhD.Thesis, Delft University of Technology, The Netherlands (1989)
- Yang R.T. "Gas separation by adsorption processes", Boston: Butterworth Publishers (1987)

## Symbols

### Latin symbols:

$C$	$[\text{kg m}^{-3}]$	adsorbate concentration in bulk
$C_s$	$[\text{kg m}^{-3}]$	adsorbate solubility
$d_1, d_2$	$[\text{m}]$	distance
$D_{eff}$	$[\text{m}^2 \text{s}^{-1}]$	effective diffusivity
$D'_a$	$[\text{m}^2 \text{s}^{-1}]$	effective diffusivity of adsorbate in adsorbate phase
$D'_w, D''_w$	$[\text{m}^2 \text{s}^{-1}]$	effective diffusivity of adsorbate in water phase
$D_w$	$[\text{m}^2 \text{s}^{-1}]$	diffusivity of adsorbate in water
$f(r)$	$[\text{m}^{-1}]$	normalised volumetric pore size distribution
$J_c$	$[\text{m}^3 \text{m}^{-2} \text{s}^{-1}]$	volumetric adsorbate flux
$J$	$[\text{kg m}^{-2} \text{s}^{-1}]$	mass adsorbate flux
$J_w$	$[\text{kg m}^{-2} \text{s}^{-1}]$	adsorbate flux in aqueous phase
$J_a$	$[\text{kg m}^{-2} \text{s}^{-1}]$	adsorbate flux in adsorbate phase
$k_a$	$[\text{m}^2]$	permeability
$k_r$	$[-]$	relative permeability
$M_a$	$[\text{kg mole}^{-1}]$	mole mass adsorbate
$P$	$[\text{Pa}]$	pressure in adsorbate phase
$P_w$	$[\text{Pa}]$	pressure in aqueous phase
$r$	$[\text{m}]$	pore radius
$r_m$	$[\text{m}]$	radius of pores in which water/adsorbate interface is situated
$r^*$	$[\text{m}]$	meniscus radius
$R$	$[\text{J mole}^{-1} \text{K}^{-1}]$	gas constant
$Q$	$[\text{kg kg}^{-1}]$	carbon loading
$T$	$[\text{K}]$	absolute temperature
$u$	$[\text{m s}^{-1}]$	linear velocity
$\langle u \rangle$	$[\text{m s}^{-1}]$	average linear velocity
$u_c$	$[\text{m s}^{-1}]$	superficial velocity
$V_a$	$[\text{m}^3]$	volume of adsorbate
$V_t$	$[\text{m}^3]$	volume of adsorbate at total saturation
$x$	$[\text{m}]$	position coordinate

### Greek symbols:

$\delta$	$[-]$	$d_1, d_2^{-1}$
$\delta_{min}$		minimum value for $\delta$ $[-]$
$\varepsilon$	$[\text{m}^3 \text{m}^{-3}]$	porosity
$\theta$	$[\text{rad.}]$	contact angle
$\mu_a$	$[\text{Pa s}]$	adsorbate viscosity
$\rho_a$	$[\text{kg m}^{-3}]$	adsorbate density
$\rho_{app}$	$[\text{kg m}^{-3}]$	apparent adsorbent density in water
$\sigma_w$	$[\text{N m}^{-1}]$	surface tension water/adsorbate interface
$\tau$	$[-]$	tortuosity

### subscripts:

$I, II$	model I, model II
$pc$	parallel cylinders

## 5. UPTAKE EXPERIMENTS

### 5.1. Introduction

An experimental study of the uptake kinetics of several organic compounds onto three different activated carbons was made to gain understanding of transport processes that take place in porous materials during adsorption. Each experiment was carried out within a small concentration range to study the effects of carbon loading on adsorption kinetics.

The experimental data were modelled with a Maxwell-Stefan approach for diffusion in porous materials.

### 5.2. Equipment

The experimental set-up used for performing kinetic experiments is shown in figure 5.2-1. In order to perform parallel experiments, 3 vessels, each with its own circulation system were installed. All used the same spectrophotometer, water-bath and computer. This permitted the running of three independent experiments at the same time. The different parts of one such installation are described below.

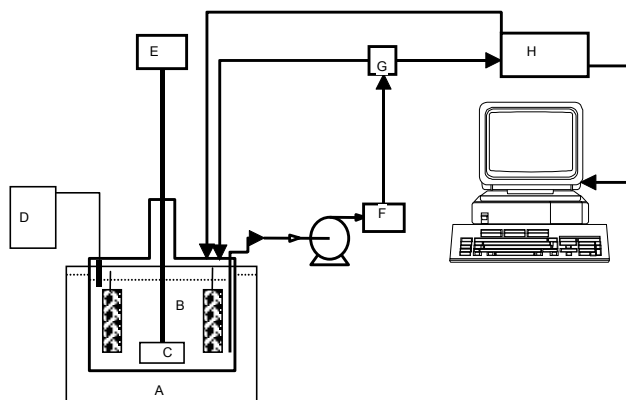


**Fig. 5.2-1.** Scheme of the experimental set-up for batch kinetic adsorption experiments, consisting of: a thermostated water-bath (A), batch vessel (B) with 2 baffles, 6-blade turbine stirrer (C,E), temperature recorder (D), filter holder (F), air-trap (G), UV/VIS spectrophotometer (H).

The batch vessels were 3.5 litre glass vessels. Each vessel stored two baffles (80\*20\*20 mm), made of stainless steel wire screen which contained the carbon. The baffles could be lifted above the liquid level to be able to add solution and to mix without changing the carbon loading. The stirrer speed was fixed at 500 rpm during the experiments.

The solution was pumped via a closed circuit of stainless steel capillaries, with an internal diameter of 2 mm, through a filter and a quartz flow-through cuvet in the spectrophotometer. The stainless steel filter holder contained a 47 mm membrane filter with a pore diameter of 0.45  $\mu\text{m}$  (Schleicher and Schüll). This filter was selected after performing experiments with several different filters. The filter prevented efficiently carbon particles from entering the cuvetts. The carbon particles can have large influence on the absorbency reading of the spectrophotometer.

The air-trap was placed in the pressure line of the pump to prevent air-bubbles from getting into the cuvetts.

In the case of the experiments that were performed above room temperature, the solution was cooled to room temperature, before entering the spectrophotometer using a cooling mantle between the pump and the air-trap. The solution was brought back to the experimental temperature after leaving the spectrophotometer by leading the capillaries through the water bath before entering the batch vessels again.

Concentrations were measured using a Beckman DU-64 single-beam spectrophotometer with a wavelength range of 200 to 900 nm. A PC was used for data acquisition from the spectrophotometer.

### **5.3. Experiments in small concentration steps**

To be able to measure the dependence of adsorption kinetics on the concentration of adsorbate in the carbon, the uptake experiments were carried out in small concentration steps.

At the first step, an amount of carbon granules, which had been saturated with water, was put inside the baffles that were pulled up in a position above the liquid level. A vessel with adsorbate, solved in de-mineralised water, was hung in its position. The stirrer and the pump were started. When the temperature of the solution had reached the desired level and the UV-spectrophotometer was reading a constant signal, which meant that the solution had been mixed well in the whole system, the stirrer was stopped and the baskets with carbon were pushed down in the solution. Thereafter the stirrer was turned on again at 500 rpm and the measurement was started.

In the beginning of the first step the spectrophotometer read the absorption in one cuvet at one wavelength, every ten seconds. From these measurements information was obtained about the external mass transfer coefficient (see section 5.4.2.). After about ten minutes the measurement continued reading the absorption in the cuvetts of the other uptake experiments too, also measuring at multiple wavelengths. The measurements were repeated between every 90 and 450 seconds, depending on the amount of readings that had to be done.

When the experiment had reached equilibrium a second step was performed. The stirrer was stopped and the baskets with carbon particles were pulled out of the solution. An amount of solution was added to the system, the stirrer was turned on again and the procedure described above was repeated. At the steps

following the first one, the frequent measurements, every ten seconds, for determination of the mass transfer coefficient were not carried out.

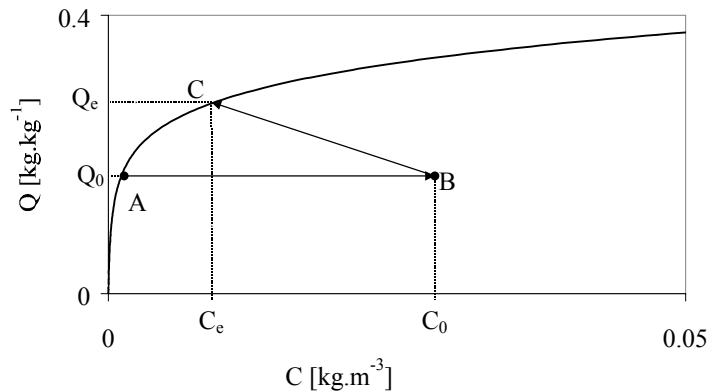


**Fig. 5.3-1** Sorption isotherm with scheme of adsorption step from equilibrium position A. Point B is the starting position of the new uptake experiment which will equilibrate in point C.

In figure 5.3-1 an isotherm is shown with a scheme of the steps described above. The system starts at equilibrium in point A. The carbon loading is  $Q_0$ . The concentration in the solution is raised to  $C_0$  (point B), the initial bulk concentration of the new adsorption step. When the baffles with carbon are put down in the solution, the carbon loading will increase and the concentration in the solution will decrease. The new equilibrium is found in point C with bulk concentration  $C_e$  and carbon loading  $Q_e$ .

## 5.4. Maxwell-Stefan diffusion model for transport in porous materials

In order to analyse the uptake experiments that were described in chapter 5.3, a surface diffusion coefficient was calculated for each adsorption step with a model based on the generalised Maxwell-Stefan equations, for both pore and surface diffusion (see fig.5.4-1). In this model the gradient of the chemical potential is the driving force for transport, consistent with the theory of Irreversible Thermodynamics [Krishna, 1987].

In the following, the theory will be outlined, resulting in a system of differential equations. Subsequently, the method is described with which the equations were solved in order to obtain surface diffusion coefficients from the experimental data.

### 5.4.1. Theory

The adsorbent was assumed to contain an almost pure aqueous phase in the larger pores and an almost pure adsorbate phase in the smallest pores. A schematic picture of the transport model is given in figure 5.4-1.

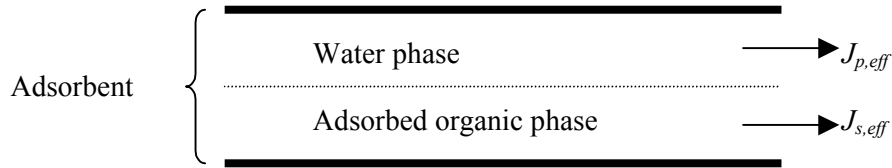


**Fig. 5.4-1** Schematic figure of the mass fluxes inside the porous material. Transport of organic component through the water phase in larger pores by molecular diffusion with a flux  $J_{p,eff}$  and transport of organic component through the adsorbed phase in the smallest pores with a flux  $J_{s,eff}$  are assumed to take place in parallel.

It was assumed that at position  $x$  in the adsorbent, a local equilibrium existed between the concentration of adsorbate in the aqueous phase and its concentration in the adsorbate phase. This equilibrium was described with the sorption isotherm.

#### *Pore diffusion*

In the aqueous phase, transport takes place by molecular diffusion of adsorbate, in the literature often called pore diffusion.

In the systems that were investigated in this thesis, it was dealt with low concentrations of adsorbate in the aqueous phase. This meant that the Maxwell-Stefan model for diffusion approached the Fickian model for diffusion [Kouyoumdiev, 1992, p.48]. Thus the molecular pore diffusion flux was written as:

$$J_p = -D_{a,w} \nabla C \quad (5.4-1)$$

where  $D_{a,w}$  is the molecular diffusion coefficient of the adsorbate in water.

Because diffusion in a porous material was considered, effects of tortuosity and porosity were taken into account.  $\epsilon_{corr}$  is the porosity of the aqueous phase inside the porous material. This is the carbon porosity minus the fraction of the volume that is occupied by the adsorbate phase.

$$\epsilon_{corr} = \epsilon_{pa} - Q \frac{\rho_{pa}}{\rho_a} \quad (5.4-2)$$

$\epsilon_{pa}$  is the particle porosity,  $\rho_{pa}$  is the particle density and  $\rho_a$  is the adsorbate density.

The density of the adsorbate phase is approached with the bulk density of the adsorbate.

A local equilibrium was assumed between the adsorbate in the aqueous phase and in the adsorbate phase. Hence, equation 5.4-1 is written as a function of carbon loading:

$$J_{p,eff} = -\frac{\epsilon_{corr}}{\tau} D_{a,w} \left( \frac{\partial C}{\partial Q} \right)^* \nabla Q \quad (5.4-3)$$

where  $\tau$  is the tortuosity factor and the asterisk denotes the equilibrium values of  $C$  and  $Q$ .

#### Surface diffusion

The Maxwell-Stefan approach, used to describe multi-component surface diffusion is outlined in detail in Kouyoumdjiev [1992].

Two important assumptions form the basis of this approach. The first one is that the vacant adsorption sites are considered to be pseudo species in the diffusing mixture, which is analogous to the model of Krishna [1993]. The second assumption is that the friction between water and organic molecules on the carbon surface is neglected. This way, for a system with one adsorbing component, a simple equation is obtained for the adsorbate flux along the pore surface without cross-diffusion coefficients [Kouyoumdjiev, 1992, p. 56]:

$$J_{s,eff} = -\rho_{pa} \left( \frac{Q}{C} \frac{\partial C}{\partial Q} \right)^* D_{s,MS} \nabla Q \quad (5.4-4)$$

A tortuosity factor does not appear in this equation because it is lumped in the Maxwell-Stefan surface diffusion coefficient  $D_{s,MS}$ .

#### Single particle mass balances

The carbon particles that were used in this study have a cylindrical shape. The differential equation describing diffusion inside a cylindrical particle with an effective Fickian diffusion coefficient, defined with

$$J = -\rho_{pa} D_{eff} \nabla Q, \quad (5.4-5)$$

in which  $J$  is the total adsorbate flux, looks as follows:

$$\frac{\partial Q}{\partial t} = \frac{1}{r} \frac{\partial}{\partial r} \left( r D_{eff} \frac{\partial Q}{\partial r} \right) + \frac{\partial}{\partial x} \left( D_{eff} \frac{\partial Q}{\partial x} \right) \quad (5.4-6)$$

$D_{eff}$  was built up from the parallel mechanisms of molecular pore diffusion and surface diffusion. Hence, according to equations 5.4-3 and 5.4-4 the effective diffusion coefficient  $D_{eff}$  was

$$D_{eff} = \left( \frac{Q}{C} \frac{\partial C}{\partial Q} \right)^* D_{s,MS} + \frac{\varepsilon_{corr}}{\tau} \left( \frac{\partial C}{\partial Q} \right)^* D_{a,w} \quad (5.4-7)$$

The boundary conditions that applied are:

$$\text{At } t = 0, \text{ every position: } Q = Q_0 \quad (5.4-8a)$$

$$\text{At } t > 0: \left( \frac{\partial Q}{\partial r} \right)_{r=0} = \left( \frac{\partial Q}{\partial x} \right)_{x=0} = 0 \quad (5.4-8b)$$

External mass transfer was taken into account via a film layer model:

$$\text{At } r = R_{pa}, \text{ all } x, \text{ all } t: k_f (C_b - C_i) = \left( D_{eff} \rho_{pa} \frac{\partial Q}{\partial r} \right)_{r=R_{pa}} \quad (5.4-8c)$$

$$\text{At } x = L_{pa}/2, \text{ all } r, \text{ all } t: \quad k_f (C_b - C_i) = \left( D_{eff} \rho_{pa} \frac{\partial Q}{\partial x} \right)_{x=L_{pa}/2} \quad (5.4-8d)$$

Here, the centre of the particle was set as the origin of co-ordinates. The radius and length of the particle are respectively  $L_{pa}$  and  $R_{pa}$ ,  $k_f$  is the external mass transfer coefficient,  $C_b$  the bulk concentration and  $C_i$  the concentration in the aqueous phase at the bulk/particle interface.

#### *System mass balance*

The measured quantity in the uptake experiments was the concentration in the bulk solution that surrounded the carbon particles. The bulk concentration at time  $t$  was a function of the integrated adsorbate profiles in the carbon particle at that time.

$$C_b(t) = C_{b,0} - \frac{4\pi n_{pa} \rho_{pa}}{V} \int_{r=0}^{R_{pa}} r \int_{x=0}^{L_{pa}/2} Q(x, r, t) dx dr \quad (5.4-9)$$

where  $n_{pa}$  is the number of carbon particles and  $V$  is the volume of the solution.

### **5.4.2. Solving the equations**

#### *Numerical solution*

To solve equation 5.4-6, a two-dimensional diffusion equation, the alternating direction implicit method (ADI-method) was used, which is a finite-difference method [Press, 1989, p.703]. The ADI-method uses the concept of time splitting. The idea is to divide each time step into two equal time steps. In each sub-step, a different dimension is treated implicitly. The advantage of this method in comparison with the Crank-Nicholson method, which is the recommended way to solve any simple diffusion equation [Press, 1989, p.696], is that each sub-step requires only the solution of a simple tri-diagonal system. The ADI-method is second-order accurate in time and space, and unconditionally stable. A number of 75 and 25 regular grid points in the  $x$  and  $r$  direction respectively proved to be sufficient for simulation of all adsorption steps with a constant  $D_{s,MS}$ . An exception was the first step that started at a carbon loading of  $0 \text{ kg.kg}^{-1}$ . A variable time grid was used with small steps at the beginning of the simulation. The number of time steps used was several thousands.

#### *Determination of the external mass transfer coefficient $k_f$*

The external mass transfer coefficient  $k_f$  was determined from the beginning of the very first adsorption step, where  $Q_0=0$ . To evaluate  $k_f$ , the assumption was made that in the very beginning of the process the external mass transfer controlled the rate of adsorption. The equation required for calculating the external mass transfer coefficient is the mass balance of the component in the bulk solution:

$$V \frac{\partial C_b}{\partial t} = -k_f n_{pa} A_{pa} (C_b - C_i) \quad (5.4-10)$$

with  $A_{pa}$ , the external surface of one carbon particle. At  $t=0$ ,  $C_i=0$ , and equation 5.4-11 is obtained from equation 5.4-10.

$$V \frac{\partial C_b}{\partial t} = -k_f n_{pa} A_{pa} C_b \quad (5.4-11)$$

Integration of equation 5.4-11 with starting condition  $C_b = C_{b,0}$  at  $t=0$  gives:

$$\ln \left( \frac{C_b(t)}{C_{b,0}} \right) = -\frac{k_f n_{pa} A_{pa}}{V} t \quad (5.4-12)$$

Thus for the external mass transfer coefficient it is found that

$$k_f = -\frac{V}{A_{pa}} \frac{\ln \left( \frac{C_b(t)}{C_{b,0}} \right)}{t} \quad (5.4-13)$$

This equation holds for the very beginning of the adsorption experiments. The mass transfer coefficients were obtained within an accuracy of a few percent from the first hundreds of seconds of the experiments.

#### *Input parameters*

The parameters that were used as input to solve equation 5.4-9 are:  $k_f$ ,  $C_{b,0}$ ,  $Q_0$ ,  $D_{a,w}$ ,  $V$ ,  $R_{pa}$ ,  $L_{pa}$ ,  $n_{pa}$ ,  $\rho_{pa}$ ,  $\varepsilon_{pa}$ ,  $\tau$  and the sorption isotherm. Obtaining the parameters  $Q_0$ ,  $D_{a,w}$  and  $\tau$  needs an extra explanation which is given below.

$Q_0$  follows from the mass balance of the preceding adsorption steps. The tortuosity was taken as  $\tau=7$ , which was estimated from values of tortuosity factors from the literature of several activated carbons. In order to estimate the molecular diffusion coefficients of small organic components in water,  $D_{a,w}$  was taken as  $10^{-9} \text{ m}^2\text{s}^{-1}$  at  $20^\circ\text{C}$  for all used components.

The molecular diffusion coefficients at other temperatures were calculated using [Perry, 1963, p. 14-23]

$$D_{a,w} = \frac{T k_D}{\mu_w} \quad (5.4-14)$$

where  $\mu_w$  is the water viscosity at temperature  $T$ .  $k_D$  is a constant.

#### *Fitting the simulations*

The Maxwell-Stefan surface diffusion coefficient was determined by fitting the simulations to the experimental data. This was done by minimising the sum of squares (SOS) of the dimensionless bulk concentration as a function of time.

The dimensionless concentrations were defined as

$$C_{b,\text{dim}} = \frac{C_b - C_{b,e}}{C_{b,0} - C_{b,e}} \quad (5.4-15)$$

Thus,

$$SOS = \sum_1^N (C_{b,dim,exp}(t) - C_{b,dim,sim}(t))^2 \quad (5.4-16)$$

was minimised.  $N$  is the number of data points. The subscripts *exp* and *sim* respectively stand for experimental and simulated data.

#### *Estimation of error bars*

In order to make an estimation of the sensitivity of the calculated value of  $D_{s,MS}$ , depending on the experimental data, intervals for  $D_{s,MS}$  were calculated between which

$$\left( \sqrt{\frac{SOS}{N}} \right) - \left( \sqrt{\frac{SOS}{N}} \right)_{\min} = 0.01$$

Here, the second term refers to the case where the  $SOS$  is minimal.

In matter of fact these intervals are the values of  $D_{s,MS}$  between which the average deviation of the simulated data points from the simulation at which the  $SOS$  is minimised is smaller than 1%.

#### *External and internal mass transfer limitation*

The error intervals as described above will partially depend on whether the adsorption process is internally or externally mass transfer limited. In the latter case the intervals will be larger. The ratio between the mass transfer resistance inside the carbon particle and the resistance at the boundary of the carbon particle was described by the Biot number for a particle with radius  $R_{pa}$ :

$$Bi = \frac{k_f R_{pa}}{\rho_{pa} D_{eff} \left( \frac{\partial Q}{\partial C} \right)^*} \quad (5.4-17)$$

where  $\frac{\partial Q}{\partial C}$  is the derivative at equilibrium at the carbon particle boundary concentration. The Biot number changed while adsorption took place, because the concentration at the particle boundary changed. The Biot numbers were calculated for  $t=0$ , thus using  $C_0$  and  $Q_0$ . Traegner [Traegner and Suidan, 1989] found that for batch kinetic experiments with  $Bi \ll 1$  the numerical values for the diffusion coefficient are not reliable.

## **5.5. Results and conclusions**

Figures 5.5-1 to 5.5-7 show the calculated  $D_{s,MS}$  as a function of carbon loading for the different activated carbons and organic components. The intervals for  $Q$  show the minimum and maximum local amount of adsorbate inside the activated carbon. The data point itself is located at the average of the minimum and maximum. The intervals for  $D_{s,MS}$  are explained in section 5.4.2.

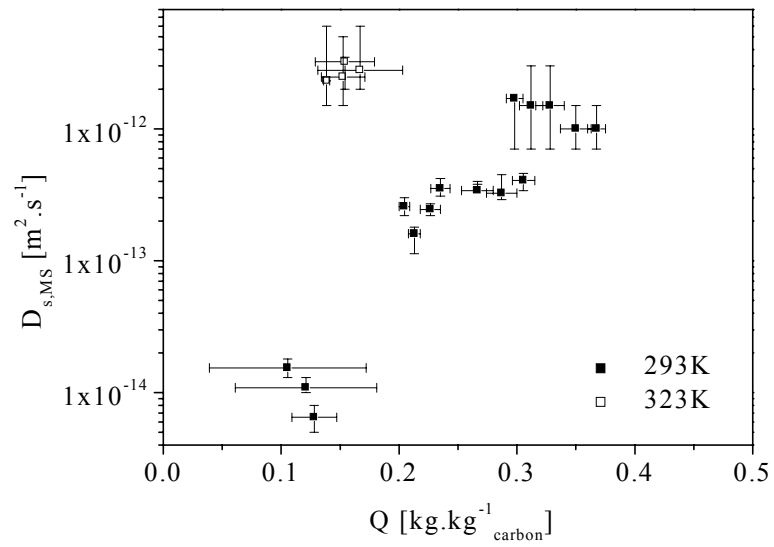


**Fig. 5.5-1**  $D_{s,MS}$  as a function  $Q_{NBZ}$  for AC RWB1 at 293K (nbz201) and 323K (nbz501).

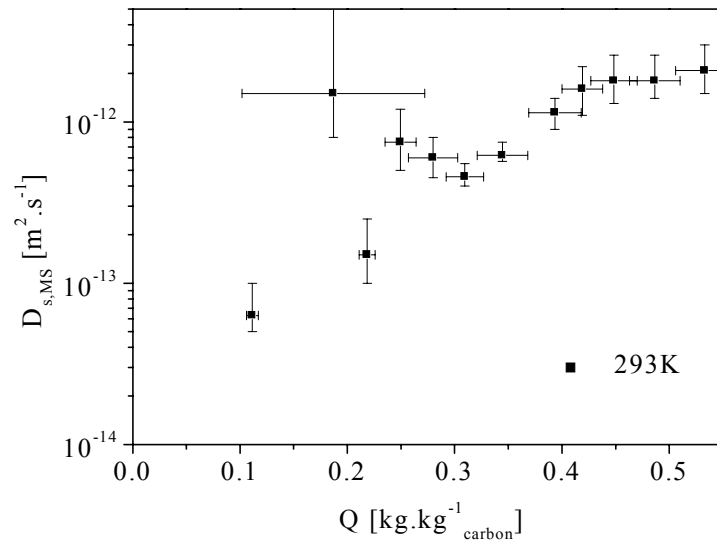


**Fig. 5.5-2**  $D_{s,MS}$  as a function  $Q_{NBZ}$  for AC R1-extra at 293K (nbz202).

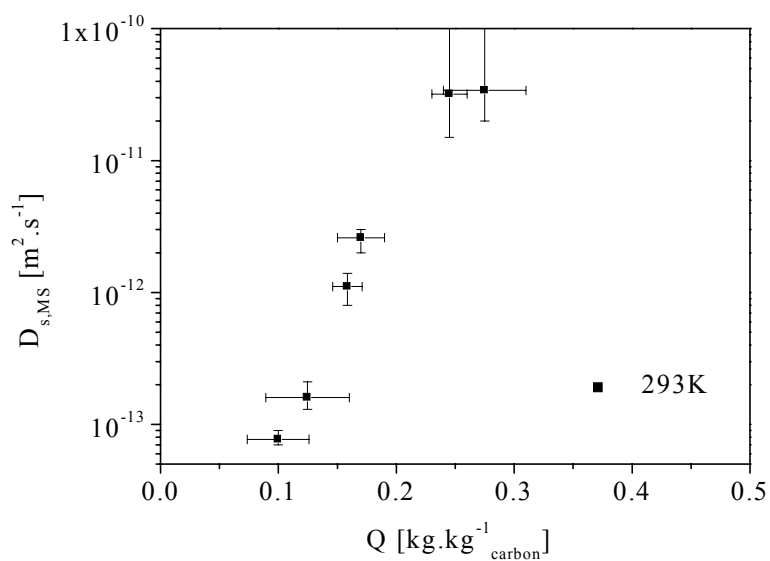


**Fig. 5.5-3**  $D_{s,MS}$  as a function  $Q_{NBZ}$  for AC AP4-60 at 293K (nbz203).

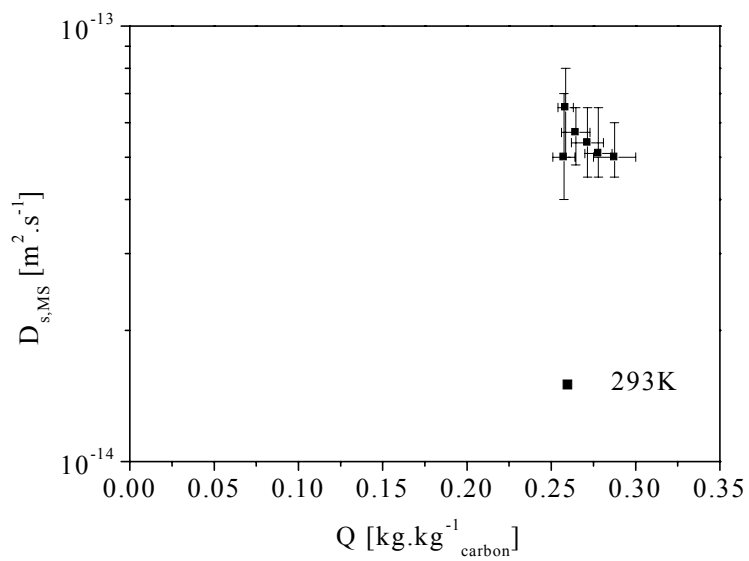


**Fig. 5.5-4**  $D_{s,MS}$  as a function  $Q_{PNA}$  for AC RWB1 at 293K (pna201).

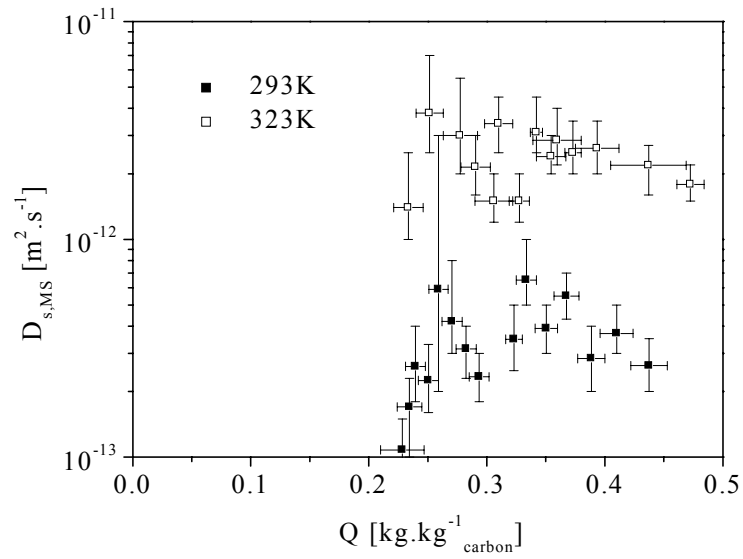


**Fig. 5.5-5**  $D_{s,MS}$  as a function  $Q_{PNA}$  for AC R1-extra at 293K (pna202) and 323K (pna502).

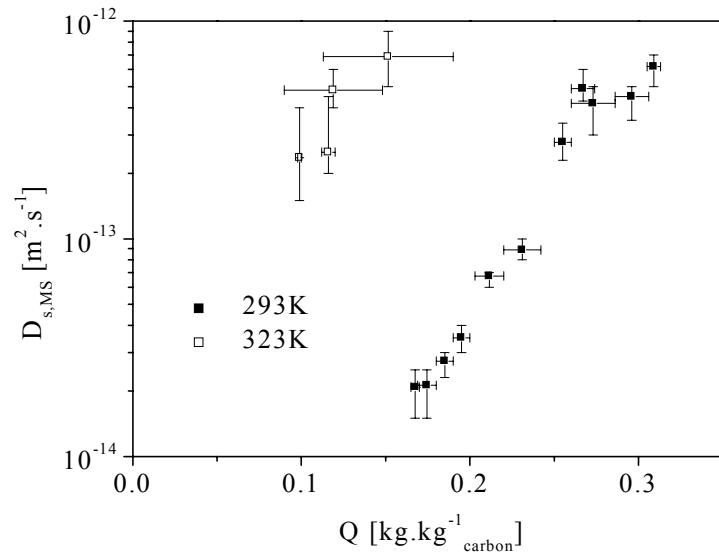


**Fig. 5.5-6**  $D_{s,MS}$  as a function  $Q_{QNX}$  for AC RWB1 at 293K (qnx201) and 323K (qnx501).

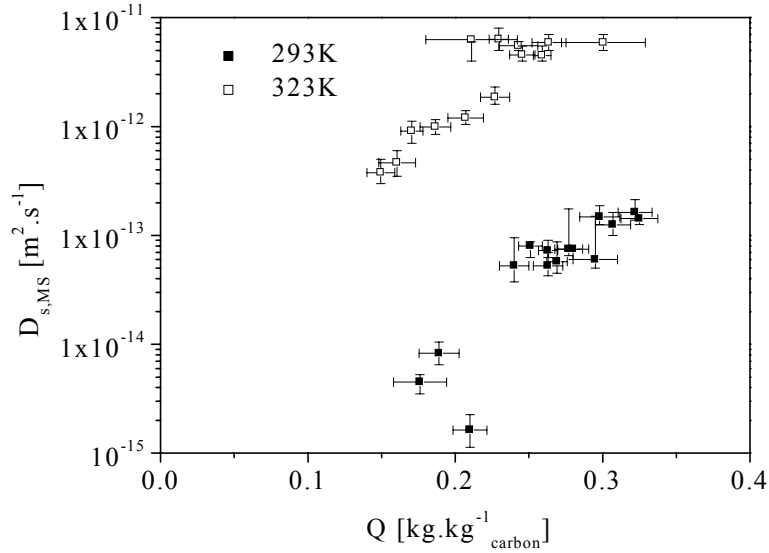


**Fig. 5.5-7**  $D_{s,MS}$  as a function  $Q_{QNX}$  for AC R1-extra at 293K (qnx202) and 323K (qnx502).

The table in Appendix 1 gives more detailed information about the experiments. In this table,

$$D_{p,eff} = \frac{\varepsilon_{corr}}{\tau} D_{a,w} \left( \frac{C}{Q} \right)^* \quad (5.4-18)$$

is the effective pore diffusion coefficient which value is directly comparable to  $D_{s,ms}$ .

It is clear that adsorbate transport by pore diffusion was negligible compared to transport by surface diffusion in all experiments.

The Biot numbers were large enough in almost every experiment to calculate a realistic value of  $D_{s,ms}$  from the experimental data.

It is noticeable that the Maxwell-Stefan surface diffusion coefficients  $D_{s,MS}$ , show a large dependence on the carbon loading (figures 5.5-1 to 5.5-7). This dependence is several orders of magnitude for the experiments of NBZ and QNX. For PNA, this is less, but that may be due to that the experimental data set of PNA is less complete. Kouyoumdjiev [1992] modelled adsorption experiments, of NBZ and PNA onto AC RWB1 over a wide concentration range, with a constant  $D_{s,MS}$ .

The increase of  $D_{s,MS}$  with increasing concentration of adsorbate is understandable, because at higher concentration, the adsorbate is adsorbed at energetically less favourable places, which gives it a higher mobility. Another contribution to the increase in  $D_{s,MS}$  with increasing carbon loading may be due to the discontinuity of the adsorbate phase. If transport of adsorbate takes place by serial transport of surface diffusion and molecular diffusion as in model II

(chapter 4), transport of adsorbate will be faster at higher carbon loading because the faster mechanism of transport by surface diffusion will have a relatively larger contribution compared to the slower mechanism of transport by molecular diffusion.

The AC AP4-60 shows a much larger  $D_{s,MS}$  at comparable NBZ concentrations than the other two carbons. The pore size distribution of AP4-60 (fig. 3.3.2-4) shows that the adsorbate is adsorbed in larger pores than in the case of the other two carbons. This also means a weaker bond between the adsorbate and the pore-wall, resulting in a higher mobility of the adsorbate.

The change of  $D_{s,MS}$  with temperature, of NBZ on AC RWB1 and of PNA on AC R1 extra, is about one order of magnitude between 293K and 323K. For QNX, however, on both the AC RWB1 and R1 extra, the change of  $D_{s,MS}$  with temperature is about two orders of magnitude between 293K and 323K. QNX is a special case in at least three ways. Firstly, as a pure bulk component, it is a solid at 293K and a liquid at 323K. This could explain the large difference in  $D_{s,MS}$  for QNX between the two temperatures, because a liquid is much more mobile than a solid. However, the question is how relevant this melting point is inside pores with a diameter of one to three molecular sizes. Also, the difference between  $D_{s,MS}$  of NBZ and PNA is not very big, while PNA has a melting point of 442K and NBZ has a melting point of 279K. Secondly, QNX consists of two rings of molecules. It may be expected that this makes the interaction with the carbon larger than in the case of the other two components. And it may be the reason for the higher temperature dependence of  $D_{s,MS}$  in the case of QNX. The third characteristic feature of QNX in comparison with NBZ and PNA is its solubility in water. At 293K it is very well soluble in water and at 323K it is completely miscible with water. In section 3.3.3, a theoretical comparison was made between the sorption isotherms of adsorbates with different physical properties. A higher interaction with the pore wall means adsorption at lower  $R_g T \ln \frac{C}{C_s}$ , especially for the first mono-layer (compare cases 4 and 6 in

section 3.3.3.2, figs. 3.3.3-7 and 3.3.3-9). A high solubility means that the pores are continuously filled, and with the formation of a mono-layer before the rest of the pore is filled. A very low solubility means discontinuous filling of the pore, without mono-layer formation before the capillary phase separation step (compare cases 4 and 5 in section 3.3.3.2, figs. 3.3.3-7 and 3.3.3-8). Because the filling of the pores is spread over a larger concentration range for the high solubility case, the adsorbate will be distributed more equally over pores of different pore widths. This, however, has no clear relation with the high temperature dependence of  $D_{s,MS}$  for QNX that was mentioned above.

## References

- Kouyoumdjiev, M.S.; 'Kinetics of adsorption from liquid phase on activated carbon', Eindhoven University of Technology, 1992.
- Krishna R.; 'A unified theory of separation processes based on irreversible thermodynamics', Chem. Eng. Comm. 59, p.33, 1987.
- Krishna R.; 'Problems and pitfalls in the use of the Fick formulation for intra-particle diffusion', Chem. Eng. Sci, Vol. 48, No. 5, p.845, 1993.
- Perry, John. H.; 'Chemical Engineers' Handbook', 4<sup>th</sup> edition, New York: McGraw-Hill book company, 1963.
- Traegner, U.K, Suidan, M.T.; 'Parameter evaluation for carbon adsorption', J. of Env. Eng., 115, p. 109, 1989.
- Press, William. H., Flannery, Brian. P., Teukolsky, Saul. A. Vetterling, William. T.; 'Numerical Recipes in Pascal, The art of scientific computing', Cambridge University Press, Cambridge, 1989.

## Symbols

### Greek symbols:

$\epsilon_{corr}$	$m^3.m^{-3}$	corrected porosity
$\epsilon_{pa}$	$m^3.m^{-3}$	particle porosity
$\mu_w$	Pa.s	water viscosity
$\rho_{pa}$	$kg.m^{-3}$	particle density
$\rho_a$	$kg.m^{-3}$	adsorbate density
$\tau$	-	tortuosity factor

### Latin symbols:

$A_{pa}$	$m^2$	external surface particle
$Bi$	-	Biot number
$C$	$kg.m^{-3}$	concentration
$C_0$	$kg.m^{-3}$	initial concentration
$C_b$	$kg.m^{-3}$	bulk concentration
$C_{b,dim,exp}$	-	dimensionless bulk concentration in experiment
$C_{b,dim,sim}$	-	dimensionless bulk concentration in simulation
$C_e$	$kg.m^{-3}$	equilibrium concentration
$C_i$	$kg.m^{-3}$	boundary concentration
$D_{a,w}$	$m^2.s^{-1}$	diffusion coefficient of adsorbate in water
$D_{eff}$	$m^2.s^{-1}$	effective diffusion coefficient
$D_{p,eff}$	$m^2.s^{-1}$	effective pore diffusion coefficient (equation 5.4-18)
$D_{s,MS}$	$m^2.s^{-1}$	Maxwell-Stefan diffusion coefficient for surface diffusion
$J_p$	$kg.m^{-2}.s^{-1}$	adsorbate flux by pore diffusion
$J_{p,eff}$	$kg.m^{-2}.s^{-1}$	effective adsorbate flux by pore diffusion
$J_{s,eff}$	$kg.m^{-2}.s^{-1}$	effective adsorbate flux by surface diffusion
$k_D$	-	constant
$k_f$	$m.s^{-1}$	external mass transfer coefficient
$L_{pa}$	m	particle length
$m$	kg	carbon mass
$n_{pa}$	-	number of particles

$Q$	$\text{kg.kg}^{-1}$	carbon loading
$Q_0$	$\text{kg.kg}^{-1}$	initial carbon loading
$Q_e$	$\text{kg.kg}^{-1}$	equilibrium carbon loading
$R$	m	position in radial direction
$R_{pa}$	m	particle radius
$SOS$	-	sum of squares
$T$	K	temperature
$t$	s	time
$V$	$\text{m}^3$	volume solution
$x$	m	position in axial direction

## 6. The application of $^1\text{H}$ -MRI to measurement of adsorption processes

### 6.1. Introduction to Magnetic Resonance Imaging (MRI) techniques

In this section the basic principles of MRI will be shortly explained. A more detailed description is given by Haacke [2000] and Kuperman [2000].

MRI is based on the interaction of a nuclear spin with an external magnetic field.

In the absence of an external magnetic field the spins are randomly oriented (figure 6.1-1a). In the presence of an external magnetic field  $\vec{B}_0$ , the spins tend to align themselves in the direction of the magnetic field (figure 6.1-1b).

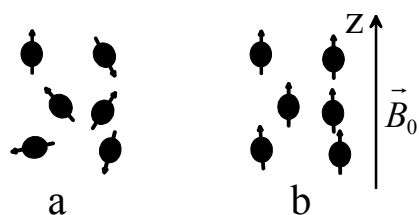


**Fig. 6.1-1** Placing a sample in an external magnetic field causes its nuclear spins to align. Note that all the spins in this diagram align with the field (parallel alignment). Fig. a is without a magnetic field and fig. b is with a magnetic field. In reality, only about half of the spins aligns parallel to the field, the rest aligns anti-parallel.

For nuclear spins there are two possible alignments or quantum states, parallel, which has a lower energy, and anti-parallel. At room temperature, the number of parallel spins exceeds the number of anti-parallel spins only with a small amount because the thermal energy is much larger than the energy difference between the two quantum states.

A spin does not simply align with the external magnetic field but performs a precession movement about the field direction. It behaves as a magnetic dipole moment, that is capable of interacting with external magnetic fields as well as producing its own rotating magnetic field that may induce an electrical current in a nearby coil. The strength of the interactions is described in terms of the magnetic dipole moment vector or magnetisation,  $\vec{\mu}$  (figure. 6.1-2).

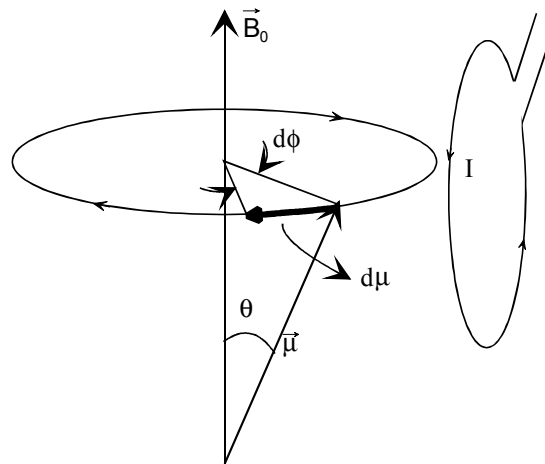


**Fig. 6.1-2** A precession movement of a nuclear spin induces an electrical current in a nearby coil.

The precession frequency,  $\omega_0$ , called the Larmor frequency, for the spin depends on the strength of the magnetic field and is given by the Larmor equation

$$\omega_0 = \gamma \vec{B}_0 \quad (6.1-1)$$

in which  $\gamma$  is the gyromagnetic ratio of the nuclei ( $\gamma/2\pi = 42.6$  MHz/Tesla for  $^1\text{H}$ ).

#### *Signal detection*

The magnetic moments of the spins of many nuclei are additive. Because the nuclei are not rotating in phase, their transverse magnetisations cancel out and the vector sum of the magnetic moments of all individual nuclei points in the direction of the external field. There is, in effect, no magnetisation flux change in the coil and thus there is no induced current.

To obtain a detectable signal in the coil, a radio frequency (RF) magnetic field pulse, that is tuned to the Larmor frequency, is applied, causing a magnetic field  $\vec{B}_1$  perpendicular to  $\vec{B}_0$ . This causes the magnetic moment vector or magnetisation to rotate away from its alignment along the  $\vec{B}_0$  axis. The angle with the z-axis of the magnetisation is related to the length and strength of the RF pulse. So-called  $90^\circ$  pulses are used in the experiments.

The RF pulse is produced in a coil by applying RF power for typical times of 10  $\mu\text{s}$  (fig. 6.1-3). Thereafter the electronics are switched from transmitting to receiving.

The rotating magnetic field produced by the precession movement of the transverse component of the magnetisation causes a current in the RF coil. This measured signal is directly related to the number of protons. The coil used for signal detection is the same as the one used for producing the RF pulse.

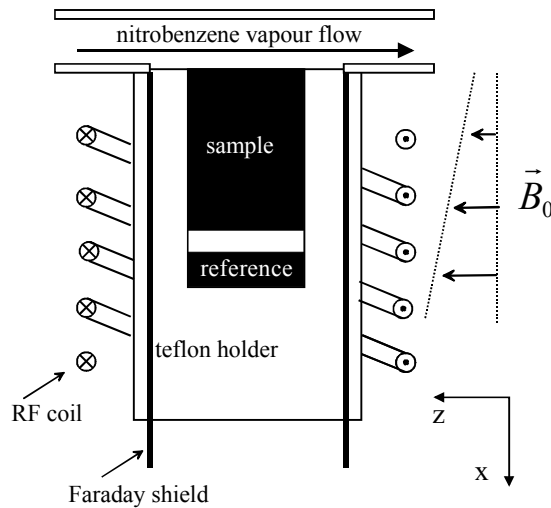


Fig. 6.1-3 MRI probe head with sample.

### Imaging

A magnetic field gradient in the  $x$ -direction (see fig. 6.1-3) causes the Larmor frequency of the protons in the magnetic field to depend on  $x$ . This offers the possibility to manipulate only the protons in a small slice of the sample by choosing the corresponding frequency of the RF pulse. By Fourier analysis of the received signal it is possible to image the sample without changing its position.

### Relaxation times

After the magnetisation has been rotated away from the direction of  $\vec{B}_0$  by an RF pulse it tends to align itself again. The rate of alignment can be characterised by the longitudinal relaxation time  $T_1$  that arises from the interaction between the spins and the atomic neighbourhood. Dephasing of the transverse magnetic moments different spins due to spin-spin interactions causes another relaxation effect. This effect is characterised by the transverse relaxation time  $T_2$ .

Dephasing by external field inhomogeneities additionally lowers this relaxation time. The latter kind of dephasing however, can be reversed by application of an additional RF pulse at time  $\frac{1}{2}T_E$  after the first pulse. Such a pulse can flip the spins  $180^\circ$  in the plane that is perpendicular to the  $z$ -axis. This results in a so-called Hahn spin-echo at a time  $T_E$ , where  $T_E$  is called the echo time [Hahn, 1950; Kuperman, 2000, p.21-23]. The data is sampled in a time interval around  $T_E$ .

The magnitude of the NMR spin-echo signal is given by

$$S \propto \rho \left[ 1 - \exp\left(-\frac{T_R}{T_1}\right) \right] \exp\left(-\frac{T_E}{T_2}\right) \quad (6.1-2)$$

in which  $S$  is the signal,  $\rho$  the proton density and  $T_R$  the repetition time of the spin-echo pulse sequence.  $T_R$  is taken as  $T_R \geq 4T_1$ , which approximately reduces the equation to

$$S \propto \rho \exp\left(-\frac{T_E}{T_2}\right) \quad (6.1-3)$$

Measurement of  $T_2$  may be interesting because it contains information about the atomic neighbourhood.  $T_2$  is measured by using a series of  $180^\circ$  pulses after the first  $90^\circ$  pulse, with time steps  $T_E$  between them. This is called a CPMG sequence, which results in a series of spin-echo signals. From this series, the transverse relaxation time  $T_2$  or the  $T_2$  distribution can be calculated.

### *<sup>1</sup>H-MRI*

Many nuclei have unpaired spins and are thus observable by MR methods. However, the strength of the signals that different nuclei produce differ greatly. The measurements discussed in this thesis are all based on hydrogen proton spins, which are the nuclei that give the strongest MR signal.

## **6.2 Measurement of nitrobenzene adsorption profiles with the aid of <sup>1</sup>H-MRI**

### **6.2.1 Introduction**

Adsorption processes, like for example wastewater treatment with activated carbon, are often influenced by intra-particle mass transfer. Thus, for design of these processes, it is important to have understanding of the intrinsic adsorption kinetics. Uptake experiments are the most common way to measure the kinetics of adsorption processes. In those experiments the integrated adsorption profiles are followed as a function of time, for example by measuring the total mass of adsorbate plus adsorbent, or by measuring concentration changes in the continuous phase surrounding the adsorbent. With those experiments, a model is needed to calculate the adsorption profiles inside the particle. Such models are usually based on Fickian or Maxwell-Stefan diffusion and assume a constant effective diffusion coefficient (see for example Kouyoumdiev [1992]). Direct measurement of the evolution of adsorption profiles with time would give considerably more information about the adsorption kinetics without model assumptions.

Magnetic Resonance Imaging (MRI) offers a possibility to perform such measurements.

MRI techniques have found its main applications in the medical field. They are used for imaging soft tissue in the human body and metabolic processes therein. The application to adsorption systems, however, has been limited by the short relaxation times of many adsorbed molecules [Ruthven, 2000]

An MRI application, with a close relation to adsorption processes, is the scanning of moisture profiles during drying of building materials like mortar

and bricks [Pel, 1995]. Because a lot of those building materials contain large amounts of paramagnetic components, relaxation times are shortened dramatically, therefore problems occur when use is made of standard MRI equipment.

The Department of Applied Physics of the Eindhoven University of Technology has developed specific MRI equipment to overcome those problems.

This study is concerned with the measurement of nitrobenzene adsorption onto activated carbon. Activated carbon is the most widely used adsorbent. There are many different types of activated carbon, depending on the raw material that is used and depending on the manufacturing process. Because of its complicated pore structure and its heterogeneous surface, that may contain several active groups, it is hard to catch adsorption processes in activated carbon in a theoretical framework. Therefore, MRI measurements can have an important contribution in the understanding of those processes. However in the case of activated carbon an additional problem occurs in the MRI measurements due to its electric conductivity. The possibility to adapt the MRI-equipment is used to solve this problem.

In the next section, the equipment and parameters used to perform the measurements are described. Profiles of nitrobenzene in activated carbon were measured during adsorption from vapour phase. The results will be presented in the subsequent section. The final section discusses those results, making use of material characteristics and the calculation of an effective diffusion coefficient for the adsorption process.

## 6.2.2. Equipment

### 6.2.2.1 The adsorption process

A nitrobenzene vapour flow was led over a carbon sample. The carbon sample consisted of 4 cylindrical particles of the extruded activated carbon Chemviron AP4-60. Each particle had a diameter of 4 mm and a length of 10 mm. The sides and bottom of the carbon particles were sealed. Therefore the nitrobenzene adsorption only took place in the x-direction (figure 6.1-3).

The temperature in the sample-holder during the adsorption process was 33°C. The vapour flow was saturated at 6°C by leading it through liquid nitrobenzene. In this case no condensation of nitrobenzene would occur in the sample holder.

The equation

$$\ln P_0 = \frac{-6122.7}{T} + 24.272 \quad (6.2.2-1)$$

was used to calculate the saturated vapour pressures,  $P_0$  [Pa], of nitrobenzene at the temperatures,  $T$  [K], mentioned above. The equation resulted from fitting to literature data [Perry, 1963, p. 3-57, 4-48].  $P_0(6^\circ\text{C})/P_0(33^\circ\text{C})=0.144$ .

### 6.2.2.2 *The MRI equipment and parameters*

The carbon sample was placed in the NMR probe head that was positioned in a magnetic field  $\vec{B}_0$  of 0.7 T. Below the sample, separated by a Teflon wall, a piece of rubber was placed which served as a reference for calibration. The probe head consisted of an RF coil, which formed a part of a tuned LC circuit, used for creating and receiving the radio frequency fields during the experiments.

Because the electric permittivity inside the resonance coil changes a lot during an adsorption experiment, the coil could get de-tuned. To prevent this, two modifications to a more common NMR set-up were applied. First, a Faraday shield was put between the carbon sample and the coil. This shield is used for all regular measurements in this set-up. Secondly, the quality factor of the coil was made lower than normal ( $Q \approx 10$ ). The disadvantage of this low  $Q$  is a low signal to noise ratio. However, the advantage is a relatively low energy storage in the coil, which was needed because of the conductivity of the carbon.

A well-defined magnetic field gradient was applied (0.4 T/m). A spin-echo experiment would therefore probe the nitrobenzene concentration in a small slice of the sample. The one-dimensional resolution, i.e., the thickness of the slice over which the nitrobenzene content was averaged, amounted to 1.0 mm. A complete nitrobenzene profile was measured by performing spin-echo experiments at various fixed frequencies that corresponded to various positions because of the magnetic field gradient. The spin-echo signal was excited by straightforward Hahn pulse sequences ( $90_x\text{-}\tau\text{-}180_{\pm x}$  and  $t_{90^\circ} = 12 \mu\text{s}$ ). The  $T_1$  of a carbon sample, fully saturated with nitrobenzene, was measured with a saturation recovery sequence. It yielded 0.2 s. To be able to make use of equation 6.1-3,  $T_R$  was taken  $5 * T_1 = 1$  s. To obtain a reasonable signal to noise ratio, 256 averages were performed.

The  $\vec{B}_1$ -inhomogeneity of the coil was corrected for by measuring a reference profile of a water sample. Profiles in the adsorption experiment were calibrated with this reference profile. After measurement of each profile, a CPMG measurement with 512 spin-echo's was carried out at 3 positions in the sample to determine the  $T_2$  as a function of nitrobenzene content. The total measurement of a profile and the 3 CPMG-sequences took about 50 minutes.

## 6.2.3. Results

### 6.2.3.1. *Calibration curve*

The NMR spin-echo intensity was measured as a function of nitrobenzene content. Therefore a number of carbon particles was out-gassed during 24 hours under vacuum at 160°C. For each sample four particles with an accurately weighted mass were brought in a flask with a certain amount of nitrobenzene. The flasks were sealed. It was assumed that equilibrium had been reached after two weeks. The particles were weighed again to obtain the amount of nitrobenzene adsorbed per gram of carbon. The evaporation of nitrobenzene during the weighing of the samples could be neglected.

The Hahn spin-echo signal was measured as a function of position. In order to obtain a workable calibration curve the signal was transformed using the following equation.

$$S = \frac{\sum_x S_{c,x}}{\sum_x S_{ref,x}} \frac{4\rho_{pa}\pi R_{pa}^2 d_{res}}{n_F m} \quad (6.2.3-1)$$

where  $S_{c,x}$  is the Hahn spin-echo signal at position  $x$  in the carbon sample and  $S_{ref,x}$  is the Hahn spin-echo signal at position  $x$  in the reference rubber (not to be confused with the water reference mentioned in section 6.2.2).

$m$  is the carbon sample mass [kg].  $\rho_{pa}$  is the carbon particle density [ $\text{kg}\cdot\text{m}^{-3}$ ].  $R_{pa}$  is the carbon particle radius [m].  $d_{res} = 1$  mm, is the slice thickness over which is averaged.  $n_F = 3$ , is the number of Fourier components (signal points) per slice.  $d_{res}$  and  $n_F$  were kept constant during all experiments.

Division by the (rubber) reference signal was carried out to correct for measurement artefacts.

The signal  $S$  that was obtained this way is in fact the average signal per Fourier point, normalised to the reference rubber.

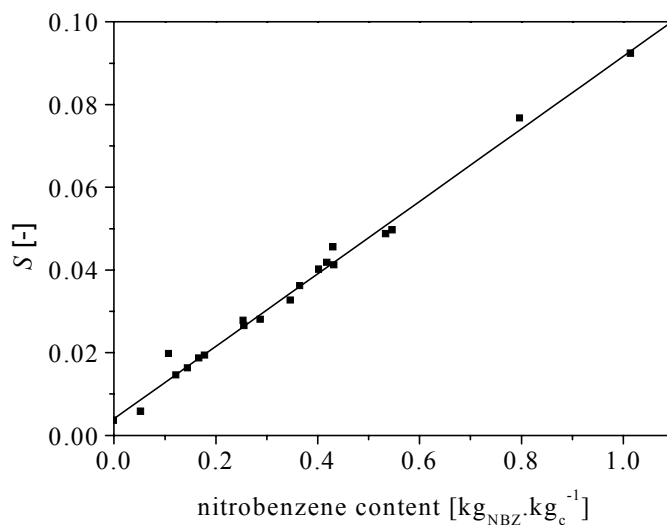


**Fig. 6.2.3-1** The calibration curve of nitrobenzene on activated carbon Chemviron AP4-60, calculated using equation 6.2.3-1.

From the calibration curve in figure 6.2.3-1, it becomes clear that the NMR signal is directly proportional to the amount of adsorbed nitrobenzene over the complete range of micro-, meso- and macro-pores. The sorption isotherm of nitrobenzene on activated carbon in aqueous phase has been measured. From this isotherm, combined with the nitrogen isotherm at 77 K, it is concluded that

the micro-pores are completely filled at about  $0.45 \text{ kg}_{\text{NBZ}} \cdot \text{kg}^{-1}_{\text{carbon}}$  (fig 2.3.3-3). At about 1 kg nitrobenzene per kg carbon the complete pore volume has been filled.

From the intercept of the calibration curve with the horizontal axis it is seen that the carbon itself shows a very small but significant spin-echo signal. This is more explicitly shown in the profile in figure 6.2.3-2. The carbon spin-echo signal was probably caused by hydrogen protons that had been bound to the carbon surface.

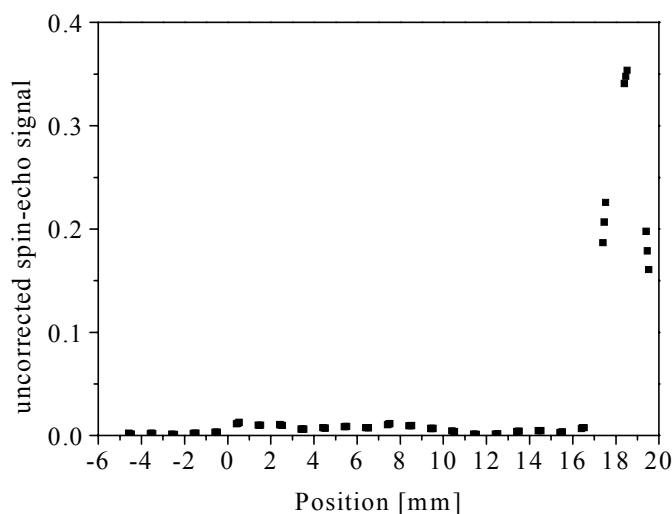


**Fig. 6.2.3-2** Profile of outgassed carbon sample and rubber reference. The outgassed carbon sample is situated between positions 0 and 10 mm. The reference is situated at about position 19 mm.

### 6.2.3.2. Nitrobenzene profiles as a function of time

Since the measurement of one profile took about 50 minutes, the data points in one profile were not measured at the same time. Therefore at each position in the sample a cubic spline was used to interpolate the data as a function of time. Figure 6.2.3-3a shows the profiles that only have been corrected with the reference signal. Figure 6.2.3-3b shows profiles that also have been time corrected by spline interpolation.

### 6.2.3.3 $T_2$ -data

#### Calibration

Like the normal Hahn spin echo measurement for a profile, also the CPMG spin echo decay was calibrated. Therefore  $T_2$ -CPMG measurements with an interpulse time of  $80 \mu\text{s}$ , number of echoes is equal to 512 and number of averages is equal to 32, were performed on every calibration sample of figure 6.2.3-1.

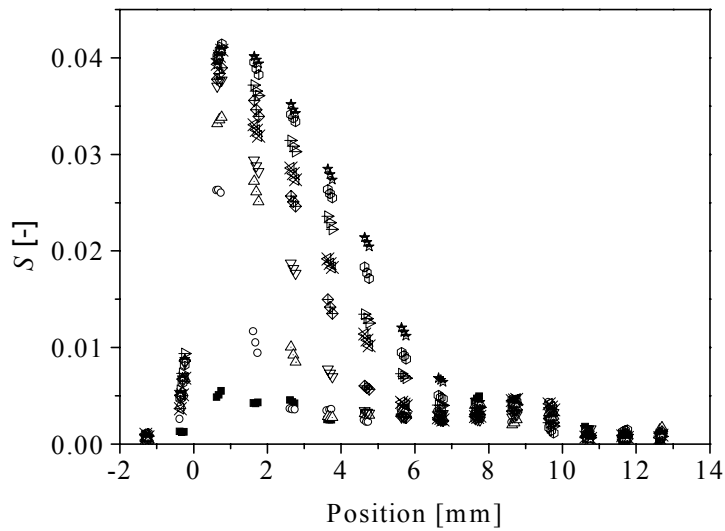


**Fig. 6.2.3-3a** Profiles that have been normalised to the rubber reference signal. The time between subsequent profiles is about 8.5 hours. The sample is in contact with the nitrobenzene vapour flow at position  $x=0$  mm.

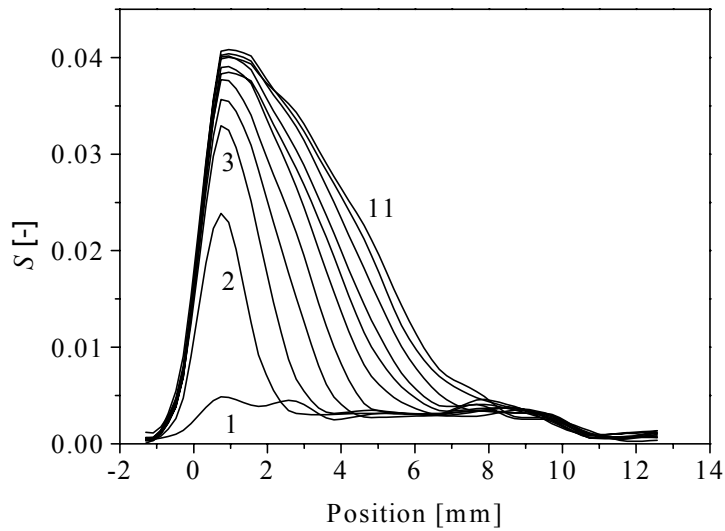


**Fig. 6.2.3-3b.** Profiles that have been normalised to the rubber reference signal. Data have been interpolated to equidistant time steps with a cubic spline. Time between subsequent profiles is about 7 hours. The sample is in contact with the nitrobenzene vapour flow at position  $x=0$  mm.

The corresponding spin echo intensities were Inverse Laplace transformed by the program CONTIN [Provencher, 1982] in order to get the relaxation time distribution. Figure 6.2.3-4 shows this relaxation time distribution for 4 calibration samples. All calibration samples show at least 2 peaks, provided that the signal to noise ratio is high enough. Calibration samples with a carbon loading smaller than  $0.25 \text{ kg}_{\text{NBZ}} \cdot \text{kg}^{-1}_{\text{carbon}}$  show only one very broad and small peak, but in these cases the signal to noise ratio was too low to obtain an accurate Inverse Laplace Transform. Calibration samples with a carbon loading that is larger than about  $0.5 \text{ kg}_{\text{NBZ}} \cdot \text{kg}^{-1}_{\text{carbon}}$  show three peaks in the relaxation time distribution.

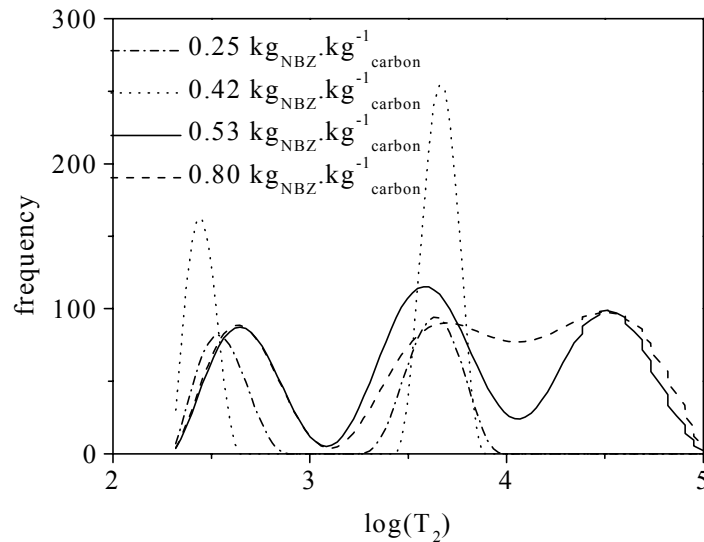


**Fig. 6.2.3-4.**  $T_2$  distribution for 4 calibration samples.

#### *Adsorption experiment*

The relaxation time distribution was measured with the same NMR pulse sequence and parameters at position  $x = 1.5 \text{ mm}$  during the adsorption experiment. Figure 6.2.3-5 shows the  $T_2$  distributions for every measured profile at this position. Profile number 1 marks the beginning of the adsorption experiment. Subsequent profiles differ approximately 50 minutes on the time-scale. The distribution has one very broad peak at the beginning of the adsorption experiment, which is due to the small signal to noise ratio. When the NBZ adsorbs onto the carbon, the signal gets more intense and two peaks in the distribution appear. The separate contributions of the protons corresponding to the two  $T_2$  peaks in figure 6.2.3-5 to the MRI signal are shown in figure 6.2.3-6.

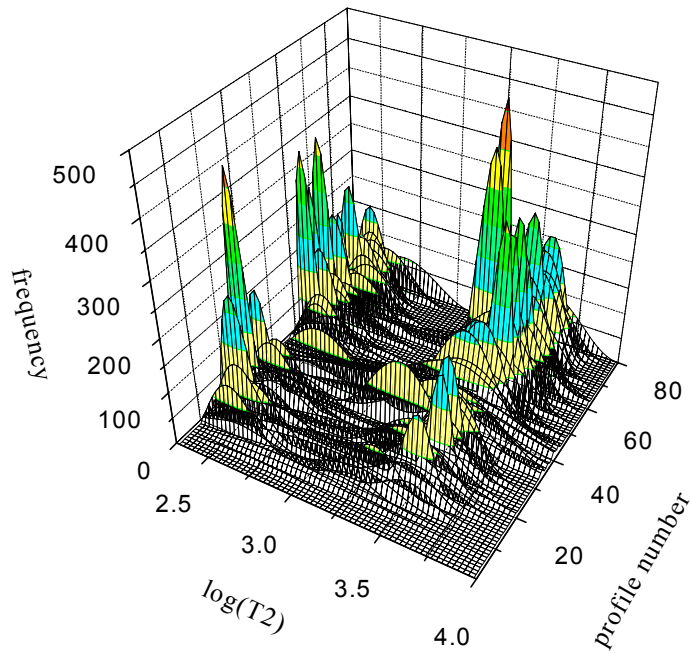


**Fig. 6.2.3-5**  $T_2$  distribution at position  $x=1.5$  mm as a function of the profile number. The first profile denotes the start of the adsorption experiment. There are about fifty minutes between the subsequent profiles. The area under the curve at a certain profile number is proportional to the amount of protons (calculated with CONTIN [Provencher, 1982]).

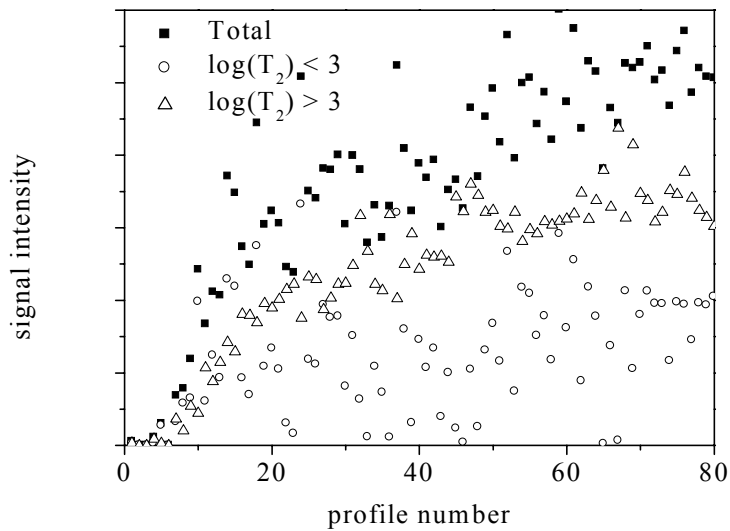


**Fig. 6.2.3-6** The separate contributions, of the protons corresponding to the two  $T_2$  peaks in fig. 6.2.3-5, to the MRI signal.

## 6.2.4. Discussion and conclusions

### 6.2.4.1. Determination of the diffusion coefficient

Fick's law was used to calculate an effective diffusion coefficient as a function of the nitrobenzene amount.

$$J = -\rho_{pa} D_{eff} \frac{\partial Q}{\partial x} \quad (6.2.4-1)$$

in which  $D_{eff}$  [ $\text{m}^2\text{s}^{-1}$ ] is the effective diffusion coefficient,  $Q$  [ $\text{kg}_{\text{nbz}}\text{kg}^{-1}_{\text{carbon}}$ ] the amount of nitrobenzene adsorbed,  $J$  the nitrobenzene flux [ $\text{kg}\cdot\text{m}^{-2}\text{s}^{-1}$ ] and  $x$  the position co-ordinate.

The differential equation describing transport in one dimension is given by Fick's law:

$$\frac{\partial Q}{\partial t} = \frac{\partial}{\partial x} \left( D_{eff} \frac{\partial Q}{\partial x} \right) \quad (6.2.4-2)$$

The external mass transfer resistance was incorporated using a film model. Since the gas phase sorption isotherm of nitrobenzene on the activated carbon were not known, the flux through the film layer was described with

$$J = -k_f \rho_{pa} (Q_{x=0} - Q_{max}) \quad (6.2.4-3)$$

where  $k_f$  is the external mass transfer coefficient,  $Q_{x=0}$  the carbon loading at the top of the sample, position  $x = 0$ . It was assumed that the partial nitrobenzene vapour pressure above the sample was constant and that the equilibrium carbon loading of the sample equalled  $Q_{max}$ , the maximum nitrobenzene content that can be reached in the sample. From figure 2.4.3-3 it follows that  $Q_{max}$  is about  $0.45 \text{ kg}_{\text{nbz}}\text{kg}^{-1}_{\text{carbon}}$  under the assumption that only the micro-pores were filled under the experimental conditions.

From equations 6.2.4-1 and 6.2.4-3 the following equation was obtained for the boundary condition at the top of the sample.

$$k_f \rho_{pa} (Q_{x=0} - Q_{max}) = \rho_{pa} \left( D_{eff} \frac{\partial Q}{\partial x} \right)_{x=0} \quad (6.2.4-4)$$

Equation 6.2.4-2 was numerically solved with a finite difference method using boundary condition 6.2.4-4 at  $x = 0$  and boundary condition

$$\frac{\partial Q}{\partial x} = 0 \quad (6.2.4-5)$$

at  $x = L_{pa}$ , which is the bottom of the sample.  $L_{pa}$  is the particle length. The profiles that were obtained numerically were transformed to a MRI spin-echo signal using the calibration curve. Subsequently the experimental resolution was taken into account. The measured signal at each position  $x$  was calculated with the average simulated signal of a sample slice between  $x - \frac{1}{2}d_{res}$  and  $x + \frac{1}{2}d_{res}$ .

The simulated profiles were fitted to the experimental profiles of figure 6.2.3-3b by minimisation of the sum of squares. Variable parameters were the external mass transfer coefficient and the coefficients of a polynomial, used to describe the effective diffusion coefficient as a function of carbon loading. The results are shown in figures 6.2.4-1 to 4. Because it is very common to use a constant effective diffusion coefficient in the Fickian model to describe the adsorption

process, a simulation with a constant diffusion coefficient is shown in figure 6.2.4-5. It is clear that the model with a constant diffusion coefficient results in adsorption profiles that are of a different shape than the experimental profiles.

#### 6.2.4.2. $T_2$ analysis

For a carbon loading larger than about  $0.53 \text{ kg.kg}^{-1}$ , the relaxation time distribution, as obtained from the calibration samples, contains three peaks. The third peak, at high relaxation times, can be contributed to NBZ in macro-pores. Because the self-diffusion constant of nitrobenzene is about  $10^{-9} \text{ m}^2\text{s}^{-1}$ , the micro and meso-pores are in the so-called fast diffusion limit [Brownstein and Tarr, 1979]. Therefore, the two peaks in the relaxation time distribution for carbon loadings smaller than  $0.53 \text{ kg.kg}^{-1}$  correspond to two peaks in the pore size distribution. It could be possible that the peak for the smallest pores is actually not a pore, but a surface layer of NBZ on the carbon. This surface layer is expected to be occupied at low carbon loading. At higher carbon loading also the space in the middle of the pores will be filled. Because of the high noise level the  $T_2$  data, from either the calibration samples (figure 6.2.3-4) or the adsorption data (figure 6.2.3-6), do not reveal whether the peak at the lowest relaxation times really rises first when filling the carbon with nitrobenzene.

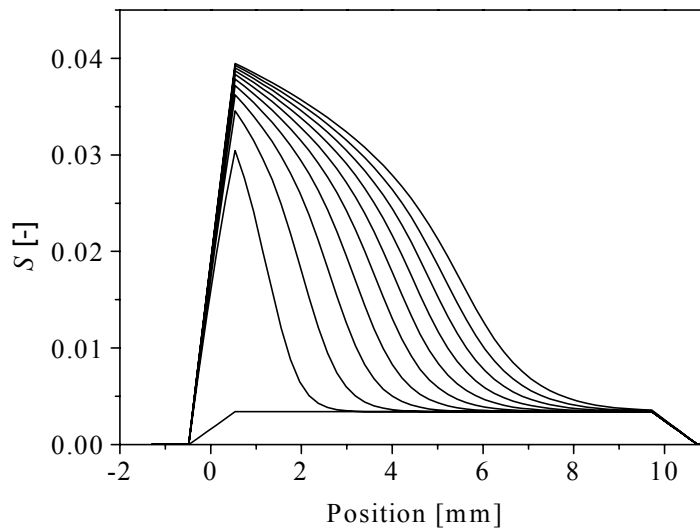


**Fig. 6.2.4-1** Simulated profiles with  $k_f = 0.569 \cdot 10^{-7} \text{ m.s}^{-1}$  and a variable diffusion coefficient that is shown in figure 6.2.4-2. Time between subsequent profiles is about 7 hours.

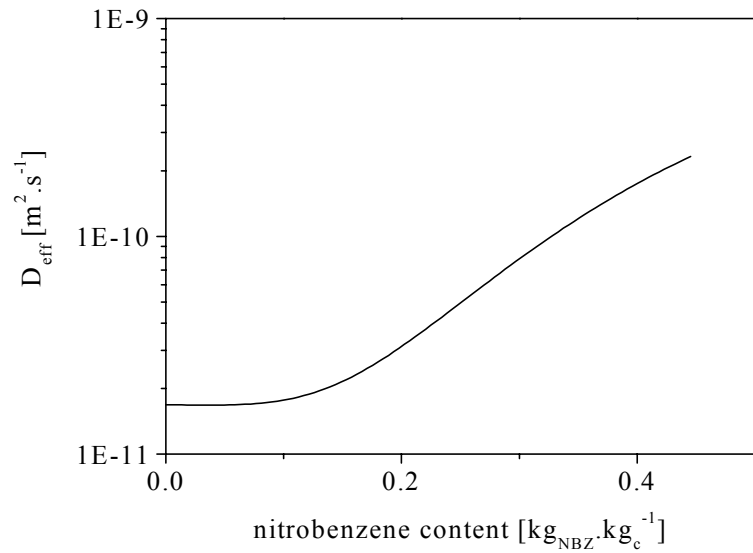


**Fig. 6.2.4-2** Diffusion coefficient used to the obtain profiles in figure 6.2.4-1 and 3.

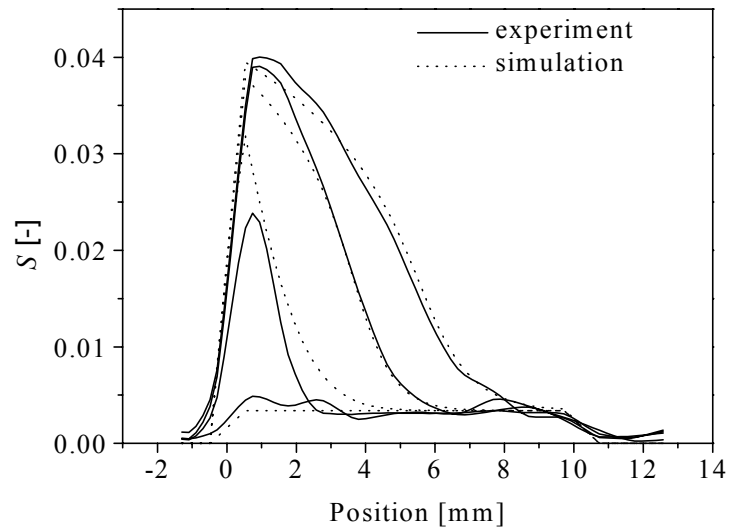


**Fig. 6.2.4-3** Background plus selection of 3 profiles from experimental data (fig. 6.2.3-3b) and simulated data with variable diffusion coefficient (fig. 6.2.4-1). The time between the subsequent profiles is about 35 hours.

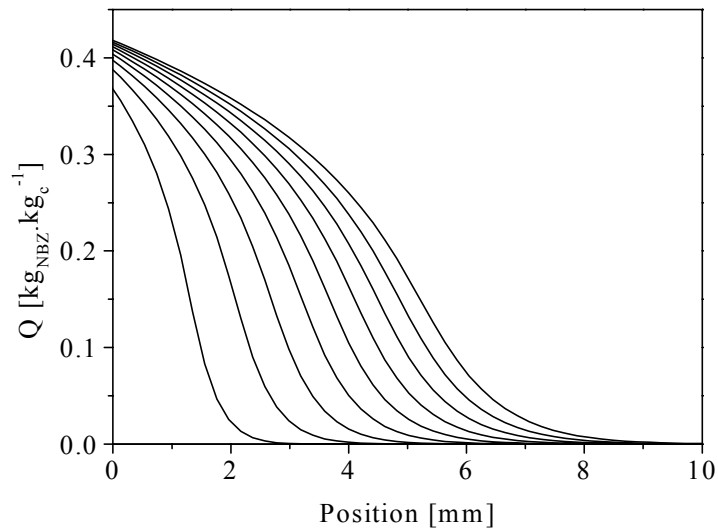


**Fig. 6.2.4-4** Profiles of carbon loading from simulation with concentration dependent diffusion coefficient, according to figure 6.2.4-2.

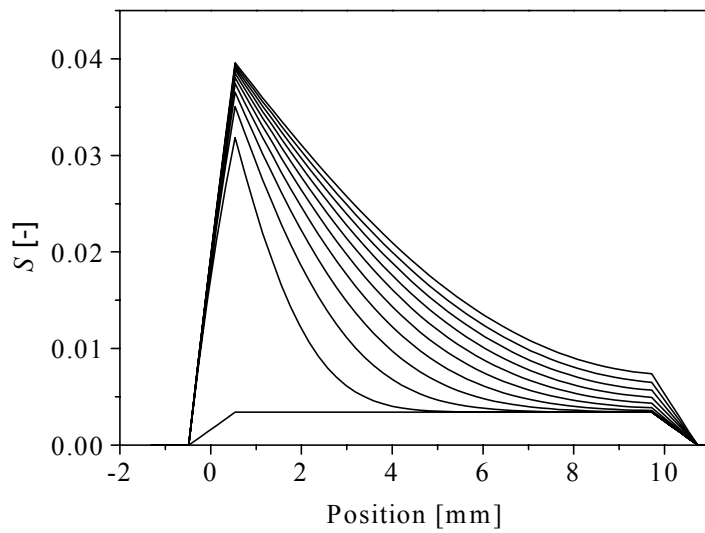


**Fig. 6.2.4-5** Simulated profiles with  $k_f = 1.92 \cdot 10^{-7} \text{ m.s}^{-1}$ . and constant diffusion coefficient  $D_{eff} = 5.61 \cdot 10^{-11} \text{ m}^2\text{s}^{-1}$ . Time between subsequent profiles is about 7 hours.

### 6.3. Measurement of nitrobenzene adsorption profiles on activated carbon saturated with D<sub>2</sub>O with the aid of <sup>1</sup>H-MRI

#### 6.3.1. Introduction

An experiment was carried out in which nitrobenzene was adsorbed on AC AP4-60 that had been saturated with D<sub>2</sub>O. The nitrobenzene profiles inside the carbon were measured with the MRI-method as described in sections 6.1 and 6.2. The D<sub>2</sub>O is not visible in the <sup>1</sup>H-NMR experiments.

This experiment is an ‘adsorption from liquid phase’ experiment. Therefore, it is comparable to the batch uptake experiments that are described in chapter 5. In those experiments the kinetics of adsorption were measured by following the concentration in the solution surrounding the carbon particles as a function of time. A Maxwell-Stefan model for surface diffusion was used to calculate an effective diffusion coefficient with which the adsorption profiles inside the carbon particles could be calculated. By using small concentration steps, the effective diffusion coefficient was obtained as a function of the amount of nitrobenzene adsorbed.

In this section a quantitative comparison is made between the adsorption profiles, directly measured with the MRI-method and the profiles, indirectly obtained from the conventional experiments in chapter 5.

#### 6.3.2. The experiment

A carbon sample, consisting of four cylindrical particles of the extruded activated carbon Chemviron AP4-60, was boiled in D<sub>2</sub>O for 1 hour in order to saturate it with heavy water. Each carbon particle had a diameter of 4 mm and a length of 10 mm. The sides and bottom of the carbon particles were sealed with teflon before the particles were put in the sample holder of the MRI equipment that is shown in figure 6.1-3. Instead of leading a nitrobenzene vapour flow over the sample, an amount of liquid nitrobenzene was put on top of the sample. The sample holder was sealed in order to prevent evaporation. Thus, nitrobenzene adsorption started to take place in the x-direction.

The temperature in the sample-holder during the adsorption process was 33°C.

The nitrobenzene density profiles were measured with the MRI equipment as described in section 6.1.

#### 6.3.3 Results and discussion

##### 6.3.3.1. Adsorption profiles from MRI measurements

In figure 6.3-1, the nitrobenzene spin-echo signal is shown as a function of position and time. The top of the sample is situated at  $x = 0$ . The one-dimensional resolution amounted 1 mm. Thus, near the top of the carbon sample, the signals of the pure nitrobenzene on top of the sample and the adsorbed nitrobenzene inside the sample interfered. Because pure nitrobenzene has a larger  $T_1$  than adsorbed nitrobenzene, equation 6.1-3 is not valid and the profiles near  $x = 0$  are questionable.

In order to estimate the influence of the resolution on the spin-echo profiles, the profiles were recalculated at each position  $x$  by averaging the measured profile within a sample slice between  $x - \frac{1}{2}d_{res}$  and  $x + \frac{1}{2}d_{res}$ . For positions at  $x < 2$  mm there is a significant difference between the original spin-echo profiles and the recalculated profiles. Also, for larger  $x$ , from about 1 mm from the profile front, there is a difference between the original and recalculated profiles.

### 6.3.3.2. Adsorption profiles from the batch uptake experiments

Figure 5.5-3 shows the nitrobenzene Maxwell-Stefan surface diffusion coefficient as a function of the adsorbed amount of nitrobenzene. Those results were obtained from batch uptake experiments as described in chapter 5. Transport of nitrobenzene by molecular diffusion through the  $D_2O$  phase in the large pores of the activated carbon is negligible in comparison to the transport of nitrobenzene that is adsorbed at the carbon surface (section 5.5). Thus, the flux at each position in the activated carbon is calculated with (equations 5.4-5 and 5.4-7)

$$J = -\rho_{pa} D_{s,MS} \left( \frac{\partial C}{\partial Q} \frac{Q}{C} \right)^* \frac{\partial Q}{\partial x} \quad (6.3.3-1)$$

in which  $D_{s,MS}$  [ $m^2s^{-1}$ ] is the Maxwell-Stefan surface diffusion coefficient.

The differential equation describing transport in one dimension is given by:

$$\frac{\partial Q}{\partial t} = \frac{\partial}{\partial x} \left( D_{s,MS} \frac{\partial Q}{\partial x} \right) \quad (6.3.3-2)$$

Equation 6.3.3-2 was numerically solved with a finite difference method using the boundary condition

$$\frac{\partial Q}{\partial x} = 0 \quad (6.3.3-3)$$

at  $x = L_{pa}$ .

The concentration of nitrobenzene,  $Q$ , at  $x = 2.2$  mm, calculated from the spin-echo signals of the MRI experiment, using the calibration curve of fig. 6.2.4-1, formed the other boundary condition. The signals for  $x < 2.2$  mm were not taken into account because of complications to the resolution, as mentioned in section 6.3.3.1.

The surface diffusion coefficient  $D_{s,MS}$  of fig. 5.5-3 was obtained from experiments at 20°C. It was described with the function

$$D_{s,MS} = \exp \left( -30 + \frac{7.25}{1 + \exp \left( \frac{-(Q-0.171)}{0.0196} \right)} \right) \quad (6.3.3-4)$$

To make a comparison with the MRI experiment that was performed at a temperature of 33°C, the surface diffusion coefficient was multiplied with by factor 3. This factor was estimated from nitrobenzene adsorption experiments

onto the AC RWB1. Those experiments were carried out at different temperatures (fig. 5.5-1). The aqueous phase sorption isotherm of nitrobenzene on AC AP4-60 was approximated from the sorption isotherm at 20°C (fig. 2.3.4-3) using the potential theory of adsorption (section 2.3.2.2).

The adsorption profiles that were obtained numerically by solving the equations were transformed to a MRI spin-echo signal using the calibration curve. For the positions  $x > 3$  mm, the profiles were corrected for the MRI resolution according to the procedure outlined in section 6.2.5.1. This correction was not necessary for positions  $2.2 < x < 3$  mm. The results are shown in fig. 6.3-2.

The profiles in figures 6.3-1 and 6.3-2 show a difference regarding their shape and the position of the profile front. It must be kept in mind that the MRI profiles that are shown, were obtained from a limited amount of data points, with a resolution of 1 mm (compare figure 6.2.4-3a). In addition, the profiles at low times are low, and thus contain relatively much noise. In order to obtain clearer information from the MRI experiments, the resolution and noise level must be improved. Possibilities in this matter are the use of a larger sample and the use of a larger external magnetic field.

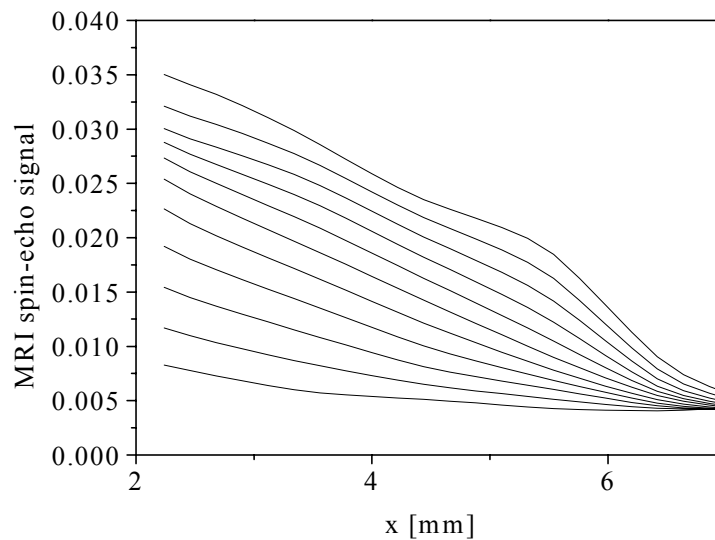


**Fig. 6.3-1** MRI spin-echo profiles from nitrobenzene adsorption onto AC AP4-60. The time between subsequent profiles is about 2000 seconds.

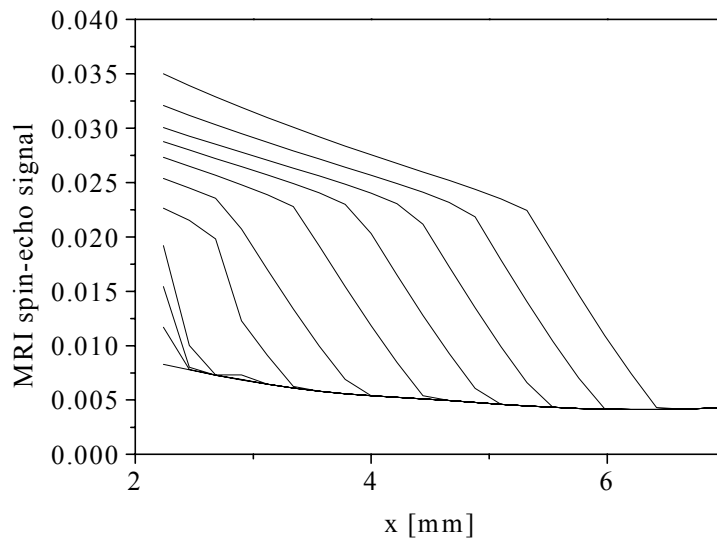


**Fig. 6.3-2** Simulated MRI spin-echo profiles for nitrobenzene onto AC AP4-60, using the data of batch uptake experiments. The time between subsequent profiles is about 2000 seconds.

A major advantage of the MRI experiment above the batch uptake is the time cost. The MRI experiment was completely performed in about one day, since all the parameters for measuring nitrobenzene adsorption onto activated carbon were known from previous experiments. The batch uptake experiments had been running for over a month, using the full capacity of the adsorption equipment that was described in chapter 5. The operations that had to be performed for the batch uptake experiments cost much more time than for the MRI measurements.

## References

- Brownstein, K.R. and Tarr, C.E., 'Importance of classical diffusion in NMR studies of water in biological cells', *Phys. Rev. A*, 19, pp. 2446-2453, 1979.
- Haacke, E. Mark; Brown, Robert W.; Thompson, Michael R., Venkatesan, Ramesh; 'Magnetic Resonance Imaging, Physical Principles and Sequence Design', John Wiley & Sons, Inc., New York, 1999.
- Hahn, E.L., 'Spin Echoes', *Phys. Rev.* 80, pp. 580-594, 1950.
- Kopinga, K. and Pel, L.; 'One-dimensional scanning of moisture in porous materials with NMR'. *Rev. Sci. Instrum.* 65 (12):3673-3681, 1994.

Kouyoumdjiev, M.S.; 'Kinetics of adsorption from liquid phase on activated carbon', Eindhoven University of Technology, 1992.

Kuperman, V.; 'Magnetic Resonance Imaging, Physical Principles and Applications', London: Academic Press, 2000.

Perry, John. H.; 'Chemical Engineers' Handbook', 4<sup>th</sup> edition, New York: McGraw-Hill book company, 1963.

Provencher, S.W., 'A constrained regularization method for inverting data represented by linear algebraic or integral equations', *Comput. Phys. Comm.* 27, pp. 213-229, 1982.

## Symbols

*Greek symbols:*

$\rho$	a.u.	proton density
$\rho_{pa}$	kg.m <sup>-3</sup>	carbon particle density

*Latin symbols:*

$\vec{B}_0$	T	magnetic field
$\vec{B}_1$	T	magnetic field
$D_{eff}$	m <sup>2</sup> .s <sup>-1</sup>	effective diffusion coefficient
$d_{res}$	m	MRI slice thickness
$J$	kg.m <sup>-2</sup> .s <sup>-1</sup>	nitrobenzene flux
$k_f$	m.s <sup>-1</sup>	external mass transfer coefficient
$L_{pa}$	m	particle length
$m$	kg	carbon mass
$n_F$	-	number of Fourier components
$P_0$	Pa	saturated vapour pressure
$Q$	kg.kg <sup>-1</sup>	carbon loading
$Q_0$	kg.kg <sup>-1</sup>	initial carbon loading
$Q_{max}$	kg.kg <sup>-1</sup>	carbon loading at complete filling of micropores
$R_{pa}$	m	particle radius
$S$	a.u.	signal
$S_{c,x}$	-	Hahn spin-echo signal at position x in the carbon sample
$S_{ref,x}$	-	Hahn spin-echo signal at position x in the reference rubber
$T$	K	temperature
$T_1$	s	longitudinal relaxation time
$T_2$	s	transverse relaxation time
$T_R$	s	repetition time of the spin-echo pulse
$T_E$	s	echo time
$t$	s	time
$x$	m	position in axial direction
$z$	m	position in direction of external magnetic field.

## 7. General conclusions

The Radke-Prausnitz model was used to model the isotherms for adsorption on activated carbon from aqueous solution for the components nitrobenzene, p-nitroaniline, quinoxaline, benzene and pyridine. This model proved to give a good fit over a large concentration range compared to popular models such as the Langmuir, Freundlich and Jossens isotherms.

The Kierlik-Rosinberg density functional theory (DFT) predicts several pore filling mechanisms for multi-component adsorption in an infinite slit pore, i.e.: continuous pore filling, pore filling by capillary phase separation, and pore filling by film layer formation followed by capillary phase separation. These mechanisms are dependent on the pore width, temperature, interactions of the components with the pore wall and interactions of the components mutually.

From DFT calculations, theoretical evidence was found for the existence of stable multi-layer solutions for sorption equilibria in an infinite slit pore. In the literature, usually, only mono-layer solutions are investigated, omitting the possible existence of stable multi-layers.

Different methods for the calculation of the micro-pore size distribution of a porous material predict different results (in this thesis, a comparison was made between the Kierlik-Rosinberg DFT and the Horvath-Kawazoe method). The prediction of the pore size may have important consequences in understanding the kinetics of adsorption. The micro-pores are only a few molecular diameters in width. In addition, the molecular motion in the first molecular layer near the pore wall differs greatly from the kinetics of molecules that are further away from the pore wall. Thus, a difference of a few molecular diameters in the pore width can make a big difference in the molecular kinetics.

When calculating sorption equilibria in a porous material, the pores are often considered as infinite and independent of each other. The length of a pore, and its surrounding area however, can have a large influence on the sorption equilibria.

It is clear that the choice of a theoretical model, for the interpretation of the micro-porous structure of a material, has a large influence on conclusions that are drawn with regard to sorption kinetics and equilibria. This stresses the importance for a better understanding of sorption processes in micro-porous materials, using more realistic simulation methods, as molecular dynamics, and taking into account pore-structure effects.

It is shown with the Kierlik-Rosinberg DFT that the liquid phase sorption isotherm of a poorly soluble adsorbate can be estimated simply from the vapour phase isotherms of the pure adsorbate and solvent.

The Maxwell-Stefan surface diffusion coefficient ( $D_{MS}$ ), using a model in which molecular diffusion in macro-pores and surface diffusion in micro-pores take place in parallel, increases several orders of magnitude with increasing carbon loading when adsorbing nitrobenzene, p-nitroaniline or

quinoxaline from an aqueous solution onto several activated carbons. This is in contrast with the popular assumption of a constant  $D_{MS}$ , made, for example, by Kouyoumdijev [1992].

One explanation for the increase of  $D_{MS}$  with the carbon loading is the location of adsorbate in larger pores at higher carbon loading. This results in a larger mobility of the molecules, due to a smaller interaction with the pore wall.

Another explanation is that the transport by molecular diffusion in macro-pores and the transport in micro-pores take place in series. This micro-pore transport is often assumed to be some kind of surface diffusion. However, regarding the results of chapters 2 and 4, this transport may also be viewed as capillary transport. At higher carbon loading, the faster mechanism of micro-pore transport (surface diffusion or capillary transport) will become more dominant, resulting in a larger  $D_{MS}$ .

The temperature dependence of  $D_{MS}$  of quinoxaline was found to be much larger than that of nitrobenzene and p-nitroaniline. No satisfactory explanation could be found for this behaviour.

Adsorption profiles of nitrobenzene in activated carbon were measured with MRI. Due to its electric conductivity, the measurements with activated carbon cannot be performed with standard MRI equipment. From the MRI measurements, more information can be obtained much faster than with the traditional batch uptake methods to measure adsorption kinetics. With the latter methods, only the integrated adsorption profiles can be measured as a function of time.

$T_2$  measurements give information about the location of molecules in the pores. Nitrobenzene molecules in macro-pores and micro-pores have a different  $T_2$ . The molecules in the micro-pores showed two different  $T_2$ 's. This may be caused by different behaviour of molecules located in the first mono-layer near the pore wall and of molecules located further away from the pore wall.

To obtain even better information about the adsorption process with MRI, it is desired to measure the adsorption profiles with a higher resolution and to measure the  $T_2$  data with less noise. This should be possible by applying a stronger external magnetic field or by using a larger carbon sample.

**Appendix 1.** Results batch uptake experiments of chapter 5  
 Symbols are explained in chapter 5

Exp. No.	$C_0$	$Q_0$	$m$	$V$	$L_{pa}$	$k_f$	$D_{p,eff}$	$D_{s,ms}$	$Bi$	$SOS/N$
--	kg.m <sup>-3</sup>	kg.kg <sup>-1</sup>	10 <sup>-3</sup> kg	10 <sup>-3</sup> m <sup>-3</sup>	10 <sup>-3</sup> m	10 <sup>-4</sup> m.s <sup>-1</sup>	10 <sup>-15</sup> m <sup>2</sup> s <sup>-1</sup>	10 <sup>-13</sup> m <sup>2</sup> s <sup>-1</sup>	--	*10 <sup>-4</sup>
nbz201a2	0.00322	0.195	0.298	2.02	2.71	2.2	0.95	2.57	11	0.49
nbz201a3	0.00365	0.202	0.298	2.02	2.71	2.2	--	1.6	19	1.7
nbz201a4	0.00456	0.210	0.298	2.02	2.71	2.2	--	3.84	9.7	4.4
nbz201a5	0.00517	0.220	0.298	2.02	2.71	2.2	--	2.45	16	0.022
nbz201a6	0.00583	0.230	0.298	2.03	2.71	2.2	--	3.53	12	0.66
nbz201a7	0.00829	0.239	0.298	2.03	2.71	2.2	--	3.32	18	0.090
nbz201a8	0.0122	0.254	0.298	2.04	2.71	2.2	--	3.4	24	2.0
nbz201a9	0.0167	0.275	0.298	2.05	2.71	2.2	--	3.25	32	1.0
nbz201a10	0.0202	0.297	0.298	2.07	2.71	2.2	--	4.06	29	0.81
nbz201b3	0.0215	0.312	1.38	2.06	2.71	3.9	--	17	13	30
nbz201b4	0.0285	0.322	1.38	2.09	2.71	3.9	--	15	18	26
nbz201b5	0.0376	0.336	1.38	2.11	2.71	3.9	--	15	23	38
nbz201b6	0.0498	0.351	1.38	2.14	2.71	3.9	--	10	44	42
nbz201b7	0.0544	0.367	1.38	2.19	2.71	3.9	--	10	46	42
nbz201c2	0.00269	0.0370	0.198	2.86	2.49	3.3	0.13	0.154	1.2E3	8.4
nbz201c3	0.00282	0.0753	0.198	2.87	2.49	3.3	--	0.109	9.1E2	19
nbz201c4	0.00136	0.0753	0.198	2.87	2.49	3.3	--	0.065	7.3E2	49
nbz501a2	0.00316	0.141	0.999	2.00	2.64	2.0	2.6	32.2	1.1	25
nbz501a3	0.00471	0.143	0.999	2.01	2.64	2.0	3.0	27.8	1.8	12
nbz501a4	0.0232	0.148	0.999	2.09	2.64	2.0	3.0	23.1	10	4.0
nbz501a5	0.00744	0.186	0.999	2.09	2.64	2.0	5.0	24.7	2.5	14
nbz202a3a	0.00126	0.127	1.90	2.01	3.29	1.1	0.50	0.63	14	14
nbz202a4a	0.0755	0.128	1.90	2.11	3.29	1.1	0.50	15	34	2.3
nbz202a5a	0.0755	0.210	1.90	2.12	3.29	1.1	1.0	1.5	2.1E2	5.3
nbz202a3	0.0317	0.357	0.646	2.04	2.61	2.2	5.0	11.4	14	46
nbz202a4	0.0379	0.394	0.646	2.04	2.61	2.2	7.0	16	10	3.2
nbz202a5	0.0561	0.425	0.646	2.04	2.61	2.2	9.0	18	13	12
nbz202a6	0.0855	0.464	0.646	2.04	2.61	2.2	10	18	18	36
nbz202a7	0.140	0.505	0.646	2.04	2.61	2.2	20	20.8	23	32
nbz202b2	0.00421	0.243	0.104	2.03	2.61	3.6	1.3	7.5	6.5	58
nbz202b3	0.00684	0.264	0.104	2.03	2.61	3.6	1.6	6	12	36
nbz202b4	0.00860	0.302	0.104	2.04	2.61	3.6	2.0	4.57	18	7.3
nbz202b5	0.0145	0.331	0.104	2.05	2.61	3.6	3.0	6.2	20	4.4
nbz203a2	0.00430	0.0580	0.252	2.00	11.4	0.67	0.80	0.77	2.1E2	9.0
nbz203a3	0.00823	0.0860	0.252	2.01	11.4	0.67	1.0	1.6	1.3E2	20
nbz203b2	0.00720	0.139	0.520	2.00	9.37	0.81	3.0	11.1	12	1.6E3
nbz203b3	0.0115	0.153	0.520	2.01	9.37	0.81	3.0	26	7.6	4.0
nbz203c2	0.0299	0.227	2.04	2.05	10.2	0.64	8.0	320	0.85	36
nbz203c3	0.0553	0.240	2.04	2.11	10.2	0.64	9.0	340	1.4	25
pna201a2	0.00667	0.264	1.52	2.07	2.44	0.95	2.0	0.5	36	16
pna201a3	0.00630	0.267	1.52	2.08	2.44	0.95	1.5	0.65	27	2.6
pna201a4	0.00896	0.270	1.52	2.10	2.44	0.95	1.5	0.57	42	2.3
pna201a5	0.0107	0.276	1.52	2.12	2.44	0.95	1.7	0.54	52	1.0
pna201a6	0.0118	0.282	1.52	2.12	2.44	0.95	2.0	0.51	59	4.0
pna201a7	0.0184	0.289	1.52	2.17	2.44	0.95	2.3	0.5	92	1.0
pna202a3	0.00291	0.206	0.303	2.04	3.62	0.81	0.90	1.08	8.3	1.0
pna202a4	0.00226	0.220	0.303	2.04	3.62	0.81	1.0	1.7	3.8	1.0
pna202a5	0.00236	0.229	0.303	2.04	3.62	0.81	1.2	2.61	2.5	1.0
pna202a6	0.00258	0.238	0.303	2.04	3.62	0.81	1.4	2.25	3.0	1.0
pna202a7	0.00327	0.246	0.303	2.04	3.62	0.81	1.6	5.9	1.4	2.3
pna202a8	0.00359	0.258	0.303	2.04	3.62	0.81	1.9	4.2	2.1	2.3
pna202a9	0.00389	0.268	0.303	2.04	3.62	0.81	--	3.14	2.9	1.0
pna202a10	0.00439	0.278	0.303	2.04	3.62	0.81	--	2.34	4.3	2.6
pna202b2	0.00654	0.259	0.398	2.00	3.62	0.91	1.7	3.48	5.2	2.3
pna202b3	0.00844	0.268	0.398	2.00	3.62	0.91	1.9	6.5	3.5	4.8

pna202b4	0.0102	0.279	0.398	2.00	3.62	0.91	2.4	3.9	6.7	4.8
pna202b5	0.0134	0.290	0.398	2.00	3.62	0.91	2.9	5.5	6.0	19
pna202b6	0.0175	0.303	0.398	2.00	3.62	0.91	3.8	2.84	14	9.6
pna202b7	0.0239	0.319	0.398	2.00	3.62	0.91	4.7	3.7	14	17
pna202b8	0.0338	0.335	0.398	2.00	3.62	0.91	6.4	2.63	27	1.0
pna502a4	0.00666	0.217	0.200	2.06	3.68	1.4	--	14	2.4	6.8
pna502a5	0.00822	0.242	0.200	2.08	3.68	1.4	--	38	0.99	1.4
pna502a6	0.0125	0.263	0.200	2.11	3.68	1.4	--	30	1.8	9.0
pna502a7	0.0189	0.294	0.200	2.16	3.68	1.4	--	15	4.7	3.2
pna502b2	0.0155	0.259	0.485	2.04	3.68	2.0	7.4	21.5	4.3	5.3
pna502b3	0.0203	0.259	0.485	2.09	3.68	2.0	--	34	3.6	14
pna502b4	0.0291	0.259	0.485	2.17	3.68	2.0	--	15	12	5.8
pna502b5	0.0382	0.259	0.485	2.28	3.68	2.0	--	24	9.5	0.81
pna502c2	0.0286	0.335	1.96	2.05	3.68	2.0	--	31	4.3	9.6
pna502c3	0.0585	0.342	1.96	2.30	3.68	2.0	--	28.5	9.5	5.8
pna502c4	0.0471	0.371	1.96	2.40	3.68	2.0	--	25	8.0	12
pna502c5	0.0842	0.381	1.96	2.79	3.68	2.0	--	26.2	13	6.8
pna502c6	0.188	0.411	1.96	2.84	3.68	2.0	41	21.9	32	11
pna502c7	0.211	0.470	1.96	2.92	3.68	2.0	--	17.9	40	14
qnx201a3	0.0687	0.242	1.45	2.07	2.66	0.80	14	4.9	33	9.0
qnx201a4	0.103	0.252	1.45	2.13	2.66	0.80	14	4.19	55	9.0
qnx201a5	0.179	0.264	1.45	2.27	2.66	0.80	30	4.5	82	6.3
qnx201a6	0.215	0.281	1.45	2.35	2.66	0.80	50	6.18	66	9.0
qnx201b2	0.00191	0.162	0.298	2.01	2.66	2.6	0.64	0.208	1E2	4.0
qnx201b3	0.00318	0.166	0.298	2.04	2.66	2.6	0.72	0.212	1.6E2	4.0
qnx201b4	0.00430	0.174	0.298	2.07	2.66	2.6	1.0	0.274	1.6E2	2.6
qnx201b5	0.00649	0.183	0.298	2.12	2.66	2.6	1.4	0.351	1.8E2	25
qnx201b6	0.0122	0.194	0.298	2.13	2.66	2.6	2.2	0.675	1.7E2	3.2
qnx201b7	0.0254	0.212	0.298	2.15	2.66	2.6	4.0	0.888	2.4E2	2.6
qnx501a2	9.31E-4	0.0982	1.04	2.01	2.64	2.0	1.2	2.36	6.2	12
qnx501a3	0.0114	0.0991	1.04	2.02	2.64	2.0	--	4.82	37	1.0
qnx501a4	0.00204	0.119	1.04	2.02	2.64	2.0	1.7	2.5	11	2.0
qnx501a5	0.0309	0.121	1.04	2.05	2.64	2.0	1.7	6.87	58	6.3
qnx202a2	0.00826	0.219	0.319	1.90	2.81	1.6	4.5	2.1	22	8.4
qnx202a3	0.00998	0.234	0.319	1.90	2.81	1.6	6.9	3.2	16	6.8
qnx202a4	0.0126	0.247	0.319	1.90	2.81	1.6	8.5	2.9	21	4.8
qnx202a5	0.0193	0.257	0.319	1.90	2.81	1.6	11	3	29	9.0
qnx202a6	0.0343	0.275	0.319	1.90	2.81	1.6	16	5.9	25	2.9
qnx202a7	0.0545	0.296	0.319	1.90	2.81	1.6	27	6.5	33	9.6
qnx202b2	0.0161	0.255	1.52	1.87	2.81	0.82	8.0	2.1	19	49
qnx202b3	0.0164	0.263	1.52	1.87	2.81	0.82	10	2.3	17	25
qnx202b4	0.0237	0.269	1.52	1.87	2.81	0.82	12	3	18	16
qnx202b5	0.0323	0.279	1.52	1.87	2.81	0.82	15	2.4	29	81
qnx202b6	0.0435	0.293	1.52	1.87	2.81	0.82	20	5	18	9.0
qnx202b7	0.0618	0.306	1.52	1.87	2.81	0.82	28	5.7	22	7.8
qnx202c2	0.00212	0.158	0.201	1.92	3.42	0.93	0.50	0.18	53	36
qnx202c3	0.00237	0.173	0.201	1.92	3.42	0.93	0.90	0.33	29	81
qnx202c5	0.00359	0.217	0.201	1.92	3.42	0.93	1.9	0.065	1.4E2	64
qnx502a3	0.00284	0.148	0.202	2.00	3.35	1.4	1.6	3.78	5.6	4.0
qnx502a4	0.00453	0.159	0.202	2.01	3.35	1.4	--	4.65	6.8	4.8
qnx502a5	0.00542	0.176	0.202	2.01	3.35	1.4	--	9.08	3.7	1.4
qnx502a6	0.00935	0.190	0.202	2.02	3.35	1.4	--	9.9	5.5	2.0
qnx502a7	0.0164	0.213	0.202	2.04	3.35	1.4	--	12	7.1	1.2
qnx502a8	0.0301	0.241	0.202	2.07	3.35	1.4	--	18.6	7.4	2.9
qnx502b2	0.0317	0.252	1.96	2.06	3.24	1.9	--	63.5	3.0	2.3
qnx502b3	0.0589	0.264	1.96	2.13	3.24	1.9	--	55.3	6.0	0.35
qnx502b4	0.0831	0.289	1.96	2.18	3.24	1.9	--	59.1	7.3	0.85
qnx502b5	0.277	0.314	1.96	2.44	3.24	1.9	--	59.1	22	6.8
qnx502c5	0.0518	0.203	0.982	2.08	3.24	1.7	6.3	62.8	5.4	4.0
qnx502c6	0.0463	0.262	0.982	2.10	3.24	1.7	--	45.6	5.2	2.9
qnx502c7	0.0590	0.279	0.982	2.12	3.24	1.7	--	45	6.3	2.9

## Dankwoord

Hier, aan het einde van mijn proefschrift wil ik graag de mensen bedanken die een bijdrage geleverd hebben aan de totstandkoming van dit boekje.

Allereerst ben ik natuurlijk dank verschuldigd aan Piet Kerkhof, die het vertrouwen in mij had om me dit onderzoek met een grote mate van vrijheid te laten doen. Verder wil ik Ton van der Zanden bedanken, mijn co-promotor, die me vier jaar lang intensief begeleid heeft. De groep van mijn tweede promotor, Klaas Kopinga, heeft me de mogelijkheid geboden om experimenten te doen met hun geweldige MRI apparatuur. Met name Leo Pel en Roland Valckenborg hebben hier veel van hun kostbare tijd in gestoken.

Marius Vorstman heeft me in het begin van mijn promotie een eind op weg geholpen en toonde altijd grote belangstelling voor mijn onderzoek. Stefan van der Sanden en Marcel Geboers, bedankt voor de discussies op wetenschappelijk en ander gebied. Anniek van Bemmelen stond altijd klaar om alle zaken in goede banen te leiden. De studenten H el ene Wuts, Marieke Verhoeven, Martijn Habets, Ruben de Wijs, Thijs Peters en Jeroen Knarren hebben veel en goed werk verricht in het kader van dit onderzoek. En natuurlijk ook dank aan de technici en alle anderen die bij hebben gedragen aan mijn proefschrift.

Speciale dank ben ik nog verschuldigd aan Gerben, Marijke, Marij, Wendy, Meike en Flora. De afleiding die jullie e-mailtjes gegeven hebben compenseerden ruimschoots de hoeveelheid tijd die ze gekost hebben. Dit geldt natuurlijk ook voor alle tijd, altijd nuttig besteed, met de rest van mijn familie en vrienden. Marco, jij krijgt nog even een aparte vermelding van mij.

En natuurlijk, papa, mama en de zusjes en broertjes, Hanneke, Ineke, Piet-Hein, Toine en Sjef, bedankt, omdat ik altijd op jullie kon en kan rekenen.

## **Curriculum Vitae**

Frans Aarden werd op 2 maart 1972 geboren te Standdaarbuiten. In 1990 behaalde hij zijn Atheneum-B diploma aan het Norbertuscollege te Roosendaal. Aansluitend studeerde hij Scheikundige Technologie aan de Technische Universiteit Eindhoven. Het afstudeerwerk werd verricht bij prof.dr.ir. P.J.A.M. Kerkhof in het Laboratorium voor Scheidingsprocessen en Transportverschijnselen. In augustus 1996 behaalde hij het ingenieursdiploma. Vervolgens werkte hij van oktober 1996 tot april 2001 in hetzelfde laboratorium aan het onderzoek dat wordt beschreven in dit proefschrift.